Optical control of single neutral atoms

Dissertation
zur Erlangung des Doktorgrades (Dr. rer. nat.)
der Mathematisch-Naturwissenschaftlichen Fakultät
der Rheinischen Friedrich-Wilhelms-Universität Bonn

vorgelegt von
Wolfgang Alt
aus
Mainz

Bonn 2004

Angefertigt mit Genehmigung
der Mathematisch-Naturwissenschaftlichen Fakultät
der Rheinischen Friedrich-Wilhelms-Universität Bonn

1. Gutachter: Prof. Dr. Dieter Meschede
2. Gutachter: Prof. Dr. Eberhard Klempt

Tag der Promotion: 30.09.2004

Abstract

This thesis presents experiments concerning the preparation and manipulation of single neutral atoms in optical traps. The experimental setup as well as the properties of the optical dipole trap are described. The long term goal of this experiment is to use trapped atoms as information carriers in quantum information processing. The examination and control of all trapping parameters and heating effects is a prerequisite for the realization of quantum gates.

A magneto-optical trap captures and cools down a few cesium atoms. By efficiently detecting their fluorescence, we are able to determine their exact number. They are then transferred without loss into a standing-wave optical dipole trap. I have measured the temperature of the atoms in this trap using two methods which are devised to work with small numbers of atoms: By adiabatically lowering the trap depth, an energy-selective loss of atoms is obtained, which yields the energy distribution of the atoms in the trap. To obtain accurate and reliable results with this method, I have modeled the measurement process with a three-dimensional numerical Monte-Carlo simulation. Alternatively, the trapped atoms are continuously illuminated by near-resonant light, and the fluorescing atomic cloud is observed with a specially designed high-resolution imaging system. The temperature is inferred from the size of the cloud and from the oscillation frequencies of the atoms in the dipole trap. The oscillation frequencies are determined in an independent measurement using resonant and parametric excitation.

I have experimentally and theoretically examined various intrinsic as well as technical heating mechanisms in the dipole trap. I find that the dominating sources of heating in the present setup are of technical origin, and I point out possible ways to reduce them.

Finally, the setup of a miniature ultra-high finesse optical resonator is presented, which will be used to couple two trapped atoms via the exchange of a photon. The optical resonance frequency of the resonator is successfully stabilized to the atomic transition by an electronic servo loop. In order not to disturb trapped atoms in the cavity mode, a weak, far-detuned stabilization laser is employed.

Zusammenfassung

Die vorliegende Arbeit berichtet über Experimente zur Präparierung und Manipulation einzelner neutraler Atome in optischen Fallen. Der experimentelle Aufbau wird vorgestellt, und die Eigenschaften der optischen Dipolfalle werden beschrieben. Das langfristige Ziel dieses Experimentes ist es, gespeicherte Atome als Informationsträger in der Quanteninformationsverarbeitung zu benutzen. Für die Realisierung von Quantengattern ist die

Untersuchung und Kontrolle aller Fallenparameter und Heizmechanismen entscheidende Voraussetzung.

Einzelne Cäsiumatome werden von einer magneto-optischen Falle eingefangen und gekühlt. Durch eine effiziente Detektion des Fluoreszenzlichtes können wir die genaue Zahl der gefangenen Atome bestimmen. Anschließend werden die Atome verlustfrei in eine optische Stehwellen-Dipolfalle umgeladen. Ihre Temperatur in dieser Falle habe ich mit zwei Meßverfahren bestimmt, die speziell dazu entworfen wurden, mit einer sehr geringen Anzahl von Atomen zu funktionieren: Zum einen wird ein energieabhängiger Verlust von Atomen durch ein adiabatisches Absenken der Fallentiefe erreicht und damit die Energieverteilung der Atome in der Falle bestimmt. Um dabei genaue und zuverlässige Resultate zu erhalten, habe ich den Meßprozeß mit einer dreidimensionalen numerischen Monte-Carlo-Simulation modelliert. Zum anderen werden die Atome mit nahresonantem Laserlicht beleuchtet und die fluoreszierende Atomwolke mit einem eigens entwickeltem hochauflösendem Abbildungssystem beobachtet. Die Temperatur wird dann aus der Größe der Atomwolke und den Oszillationsfrequenzen der Atome in der Dipolfalle abgeschätzt. Die Oszillationsfrequenzen werden in einer unabhängigen Messung mittels resonanter und parametrischer Anregung bestimmt.

Verschiedene fundamentale sowie technische Heizmechanismen in der Dipolfalle habe ich experimentell und theoretisch untersucht. Dabei habe ich herausgefunden, daß die dominierenden Heizeffekte technischen Ursprungs sind, und Maßnahmen zu deren Reduzierung vorgeschlagen.

Schließlich wird der Aufbau eines miniaturisierten optischen Resonators sehr hoher Finesse präsentiert, der später verwendet werden soll, um eine kontrollierte Wechselwirkung zwischen zwei gespeicherten Atomen durch den Austausch eines Photons zu erzeugen. Eine elektronische Regelschleife stabilisiert die optische Resonanzfrequenz des Resonators auf den atomaren Übergang. Um gespeicherte Atome, die sich in der Resonatormode befinden, nicht zu stören, verwenden wir zur Stabilisierung einen schwachen, in der Frequenz weit verstimmten Laserstrahl.

Publications

Parts of this thesis have been published in the following papers:

1. W. Alt, *An objective lens for efficient fluorescence detection of single atoms*, Optik **113**, 142 (2002)

2. W. Alt, D. Schrader, S. Kuhr, M. Müller, V. Gomer, and D. Meschede, *Single atoms in a standing-wave dipole trap*, Phys. Rev. A **67**, 033403 (2003)

Contents

Introduction

Experiments with individual quantum systems open the possibility to investigate quantum effects on a fundamental level. One topic which presently receives much attention is quantum information processing. Quantum bits or qubits are quantum-mechanical superposition states of the logical states "0" and "1" of the classical bit. By processing qubits with quantum gates, a quantum computer is fundamentally superior to classical computers in certain cases. For example, the computation time required for the factorization of a large integer by classical algorithms grows exponentially with the number of digits. A quantum algorithm, however, is in principal capable of performing the factorization in polynomial time [1].

The internal states of atoms are prominent candidates for the physical realization of qubits. Quantum gates, the fundamental building blocks of quantum algorithms, can be performed by switching on and off a well-controlled coherent interaction between two qubits. At the same time, the interaction with the environment must be minimized as it leads to decay ("decoherence") of the fragile quantum superposition states.

Quantum logic operations have been demonstrated experimentally with chains of ions in Paul traps [2, 3]. These gates use the coulomb interaction of the ions, which at the same time makes them very sensitive to external electric fields. Our goal is to construct a quantum register from neutral atoms, which are potentially more robust to external perturbations.

For this purpose, we cool, trap and observe single cesium atoms with a magneto-optical trap. A prior system [4] was completely rebuilt and improved in many ways, as described in chapter 1.1 and in the thesis of Stefan Kuhr [5]. It now provides better optical access, variable magnetic fields, a high-resolution optical fluorescence detection system of increased sensitivity and a computer control of all relevant parameters.

For the manipulation of internal atomic states, the atoms prepared in the magneto-optical trap are then transferred without loss into an optical dipole trap. Here, the atoms can be stored while their internal state is preserved. This property makes the dipole trap a promising container for qubits. For the dipole trap we use two counterpropagating focused laser beams, which create a standing wave interference pattern, as described in chapter 1.2. This one-dimensional optical lattice allows us to trap several atoms in individual potential wells with very good axial confinement. Additionally, we are able to transport atoms along the dipole trap axis by mutually detuning the two laser beams, realizing an "optical conveyor belt" [5, 6]. A coherent superposition of internal atomic states is conserved [7].

To obtain maximum control over the atoms in the dipole trap, I have determined the important trapping parameters such as temperature, oscillation frequencies and heating rates. The temperature is an important parameter because it leads to an inhomogeneous broadening of all atomic transitions due to the influence of the dipole trapping potential. This effect limits the coherence time available for quantum operations. Furthermore, the temperature determines the localization of the atoms, which is a crucial parameter for the coherent interaction required for two-qubit gates. Knowledge of the oscillation frequencies of the atoms confirms our theoretical description of the dipole trap and is required for cooling schemes such as Raman cooling.

Since our traps operate only with relatively small numbers of atoms, the standard methods for the measurement of the temperature of trapped atomic ensembles, such as time-of-flight, cannot be used. I have therefore developed suitable methods to measure the temperature of single trapped atoms, described in chapter 2. One method is based on an adiabatic lowering of the trap depth to obtain an energy-selective loss of atoms, which yields the energy distribution of the atoms in the trap. A short theoretical description of this process is given, but I had to resort to extensive numerical modelling to include the effects of various experimental imperfections in order to obtain a reliable and accurate result. The other method uses the size of the trapped atomic cloud and the measured oscillation frequencies to estimate the temperature of the atoms. For this purpose, the trapped atoms are illuminated with near-resonant light and are observed with an intensified CCD camera through our optical imaging system.

I further present a thorough analysis of heating effects in the dipole trap in section 2.4, in which I identify the dominant heating mechanisms. These results may enable us to improve the properties of our dipole trap by eliminating technical sources of heating, and to evaluate possible schemes to cool the atoms to significantly lower temperatures. Some cooling schemes are mentioned in the outlook.

For the implementation of quantum gates we want to use the atom-atom interaction mediated by an optical resonator. Two atoms placed into the mode of a high quality resonator can exchange photons and in this way become entangled [8], or exhibit dynamics corresponding to basic gates [9]. A quantum phase gate has been experimentally demonstrated in microwave cavities [10]. Present experiments send beams of atoms flying through a microwave cavity [11], or throw clouds of atoms through an optical resonator [12, 13]. In these cases, the average number of atoms inside the cavity mode must be small to avoid three-atom events. Therefore, the simultaneous presence of two atoms in the cavity occurs with low probability. Our standing wave dipole trap, however, can transport a predetermined number of atoms over macroscopic distances. We plan to use this optical conveyor belt to deterministically place exactly two atoms into the interaction region.

Quantum operations by photon exchange require strong coupling between atoms and cavity field in conjunction with a weak coupling to the environment. Strong coupling is obtained by confining the light to a small volume with a resonator, while the coupling to the environment is given by the loss rate of photons from the cavity. It turns out that very high demands are placed on the mirrors and their stability, especially in the optical region, where the lowest technically feasible absorption and transmission losses are required. We constructed such a high finesse optical resonator and mounted it in such a way that it can be integrated into our existing single atom apparatus. We have characterized the resonator [14], and we are able to stabilize the resonance frequency of the resonator with an electronic servo loop close to the required precision. Moreover, we achieve a continuous stabilization without disturbing the atoms within the resonator by using a far-detuned stabilization laser, as described in chapter 3.

Our endeavors to prepare and detect the quantum state of an atom in the dipole trap and to transport the atom without changing its state have recently been successful [7]. This level of control opens the route to the construction of a quantum shift register with neutral atoms. Together with the optical resonator, elementary quantum gates with neutral atoms might be possible.

Chapter 1

Trapping of single atoms

Electromagnetic cooling and trapping of neutral atoms is essential for experiments where isolated atoms are to be studied for a long time compared to the transit time of a thermal atom through an experimental region. Our experiments on the optical control of single neutral atoms use two different traps: a magneto-optical trap and an optical dipole trap. In the past years these traps have been refined and optimized to enable us to prepare, manipulate and observe single cesium atoms in various ways. Operations such as preparing and detecting the hyperfine state of a single atom or transporting an atom over macroscopic distances have become standard experimental techniques in our lab.

1.1 A magneto-optical trap for single atoms

Cooling of atoms by near-resonant laser radiation (Doppler cooling) has been proposed 1975 by T. Hänsch and A. Shawlow [15]. Three-dimensional laser cooling has been first demonstrated in 1985 by S. Chu [16]. This configuration evolved into a magneto-optical trap [17] by adding an inhomogeneous magnetic field after a suggestion of J. Dalibard in 1987. The magneto-optical trap (MOT) has become a widely used tool for atom trapping, since it captures atoms from a dilute gas at room temperature, cools them down to sub-millikelvin temperatures and keeps them confined for long times. Additionally, the MOT continuously excites the atoms, which in turn radiate fluorescence photons. In our case, the fluorescence allows us to infer the number of atoms in the MOT.

1.1.1 Operating principle

The MOT cools and confines atoms at the same time by exerting light forces on the atoms. Since the atom acquires the momenta of the photons it absorbs, these forces can be thought of as “light pressure” acting on the

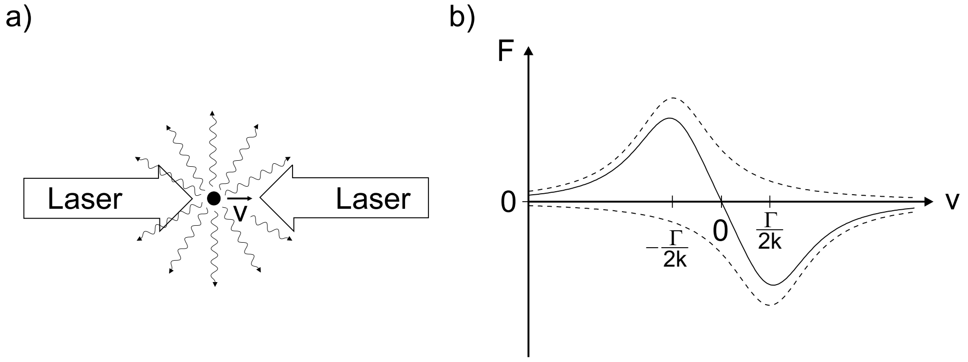

Figure 1.1: Doppler cooling. (a) The moving atom preferentially absorbs photons in the opposite direction of motion, whereas the spontaneous emission is random. (b) Light force versus velocity for a detuning of $-\Gamma/2$. Each laser beam gives rise to a Lorentzian force dependency (dashed curves) with maxima at $v = \pm\Gamma/(2k)$. The cooling force is the sum of both forces (solid line).

atom. Cooling is achieved through a velocity-dependent light force, which results in a friction-like slow down. The confinement is due to a position dependent light force which pushes the atom towards the trap center.

Doppler cooling

To explain the doppler cooling mechanism, we use a two-level atom with only two energy eigenstates, a stable ground state $|\, g\,\rangle$ and an excited state $|\, e\,\rangle$ of energy $\hbar\omega_0$ and lifetime $\tau = 1/\Gamma$, coupled by a radiative transition. This atom is illuminated by a monochromatic laser beam of frequency ω and intensity I.

The atom absorbs photons from the beam and spontaneously re-emits them randomly. The scattering rate R_s is given by

$$R_\mathrm{s}(I,\Delta) = \frac{\Gamma}{2}\frac{I}{I_0}\left[1 + \frac{I}{I_0} + \left(\frac{2\Delta}{\Gamma}\right)^2\right]^{-1}, \tag{1.1}$$

where $\Delta = \omega - \omega_0$ is the detuning of the laser from the atomic transition, and I_0 is the saturation intensity of the transition. In the limit of low intensity eq. (1.1) is a Lorentzian line shape centered at ω_0 with a full width at half maximum of Γ.

Two counterpropagating laser beams, which are slightly red detuned with respect to the atomic resonance ($\Delta < 0$), can be used to slow down the atom in one dimension (see fig. 1.1(a)): When the atom moves to the right, the laser beam from the right is blue shifted into resonance by the Doppler effect, and thus its scattering rate increases. In the same way, the laser from the left is shifted out of resonance and its scattering rate decreases. As a consequence, the atom receives more momentum kicks from the right than from the left and is therefore slowed down. The recoil momenta from the spontaneous emission events average out to zero. The average force on the atom then becomes

$$F(v) = \hbar k \left[R_{\mathrm{s}}(I, \Delta - kv) - R_{\mathrm{s}}(I, \Delta + kv) \right] \tag{1.2}$$

and is shown in fig. 1.1(b) for $\Delta = -\Gamma/2$. For small velocities this function can be approximated by a linear dependence $F \sim v$, which resembles a viscous drag.

Optical molasses

The Doppler cooling scheme can be extended to three dimensions by using three mutually orthogonal sets of counterpropagating laser beams. This configuration is called optical molasses, since it provides a viscous friction force for atoms moving in arbitrary directions.

Doppler cooling does not permit cooling to zero temperature ($v = 0$), since the stochastic nature of the momentum kicks due to absorption and spontaneous emission leads to a fluctuation of the atomic momentum around its steady state value $\langle \mathbf{p} \rangle = 0$. This "random walk" or diffusion process in momentum space heats up the atom and leads to a non-zero equilibrium temperature called "Doppler limit" or "Doppler temperature" of about $k_{\mathrm{B}} T_{\mathrm{D}} = \hbar\Gamma/2$ [18, 19].

The simple two-level atom model of Doppler cooling presented here neglects the multilevel structure of real atoms, the polarizations of the light fields, and the dipole force (see section 1.2). A more complete theory which includes these phenomena shows several "sub-Doppler" cooling mechanisms [20], which can lead to temperatures two orders of magnitude below the standard Doppler limit. For the laser beam parameters in our MOT, however, sub-Doppler cooling plays no important role and is not discussed here.

In our experiment we use the D2-transition of cesium atoms at $\lambda = 852$ nm for cooling (see appendix A). The natural linewidth of $\Gamma = 2\pi \times 5.2$ MHz leads to a Doppler temperature of $T_{\mathrm{D}} = 125$ µK. The one-dimensional atomic rms velocity at the Doppler temperature is $v_{\mathrm{D}} = \sqrt{k_{\mathrm{B}} T_{\mathrm{D}}/m} = 0.09$ m/s. According to fig. 1.1(b), the cooling force extends only up to velocities which produce Doppler shifts in the order of Γ, resulting in a capture velocity of a few m/s. Thus, from thermal cesium atoms ($v_{\mathrm{rms}} = 240$ m/s) only the very low velocity tail of the Boltzmann distribution can be captured. The maximum acceleration due to resonant light pressure is produced by the maximum possible scattering rate of $\Gamma/2$ and equals $a_{\mathrm{res}} = \Gamma\hbar k/(2m) = 5.8 \times 10^4$ m/s^2. This large value permits a rapid

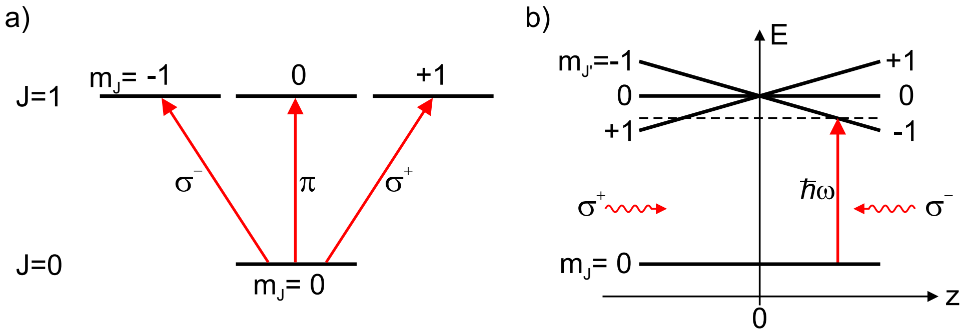

Figure 1.2: One-dimensional picture of the MOT. (a) When exciting an atom from $J = 0$ to $J = 1$, transitions with $\Delta m_J = -1, 0, +1$ can only be excited by σ^--, π- and σ^+-polarized radiation, respectively. (b) A magnetic quadrupole field shifts the Zeeman sublevels such that the laser beam, which pushes the atom back to $z = 0$, is absorbed preferentially.

cooling process, such that the Doppler limit is reached within less than a millisecond.

Position dependent force

A position dependent restoring force, which always points towards the trap center, turns an optical molasses into a trap. Without this force, an atom usually leaves the molasses region in less than a second due to its diffusive motion. In a MOT, the restoring force is produced by the same laser beams which constitute the optical molasses. The atomic absorption is spatially modulated by a magnetic quadrupole field in conjunction with polarizations of the laser beams.

The working principle can be understood in a simplified one-dimensional model where the atomic states are characterized by the angular momentum quantum numbers J and m_J. A single $J = 0$ ground state is coupled to a degenerate $J = 1$ -manifold, see fig. 1.2(a). A magnetic field B splits the excited state according to the linear Zeeman effect, where the level $|\, J, m_J\,\rangle$ is shifted by the energy

$$\Delta E = m_J g_J \mu_{\mathrm{B}} B, \tag{1.3}$$

where g_J is the Landé g-factor and μ_{B} is Bohr's magneton.

In one dimension, the magnetic field has the form

$$B(z) = \frac{\mathrm{d}B}{\mathrm{d}z}\, z, \tag{1.4}$$

where $\mathrm{d}B/\mathrm{d}z$ is the field gradient in z-direction. We assume $\mathrm{d}B/\mathrm{d}z > 0$ and $g_J > 0$. Then, as shown in fig. 1.2(b), to the right of the zero point of the magnetic field, the $|\, J = 1, m_J = -1\,\rangle$ level is shifted downwards, into resonance with the red detuned cooling laser. If the laser beam, which

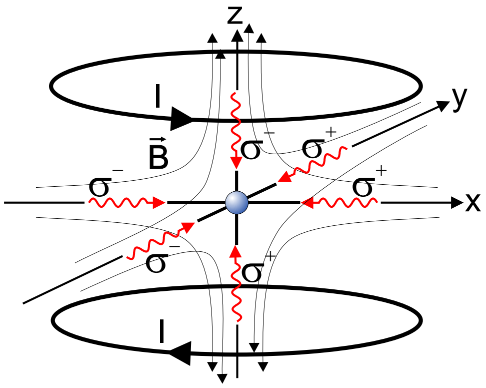

Figure 1.3: Three-dimensional schematic of the MOT. Two magnetic coils in anti-Helmholtz configuration produce the quadrupole field, and 6 circularly polarized laser beams exert cooling and trapping forces.

comes from the right, is σ^--polarized, it will strongly excite the red-shifted $|\,J=1, m_J=-1\,\rangle$ level, pushing the atom to the left. Conversely, the σ^+-polarized beam from the left will only weakly excite the blue-shifted $|\,J=1, m_J=+1\,\rangle$ level. Altogether, an atom located to the right of the magnetic zero point experiences a force to the left, i. e. towards the trap center. In a similar fashion, an atom left of the trap center is pushed to the right.

This scheme can be extended to three dimensions, by using two magnetic coils in anti-Helmholtz configuration to produce a quadrupole field of the form

$$\mathbf{B}(\mathbf{x}) = \frac{\mathrm{d}B}{\mathrm{d}z}\left(-\frac{x}{2}, -\frac{y}{2}, z\right), \tag{1.5}$$

and shining in two circularly polarized beams of right-handed helicity (z) plus four circularly polarized beams of left-handed helicity (x, y), see fig. 1.3.

Although the MOT forces do not form a conservative potential, a "trap depth" can be defined via the minimum velocity an atom needs to escape from the trap. An estimation of the potential barrier is the resonant scattering force times the radial distance over which it extends. The restoring force ceases to work at a radius where the Zeeman detuning of the relevant atomic transition exceeds the detuning of the MOT lasers. A high magnetic field gradient $\mathrm{d}B/\mathrm{d}z$ yields a small radius and therefore a shallow trap [21, 22].

The rate R_c at which the MOT captures atoms from a thermal background gas also depends strongly on the field gradient. A simplified classical model [23] yields

$$R_\mathrm{c} \sim \left(\frac{\mathrm{d}B}{\mathrm{d}z}\right)^{-14/3}. \tag{1.6}$$

This dependence is used to control the loading rate of the MOT, see sec. 1.3.1.

Typical magnetic field gradients are $10-300$ G/cm ($0.1-3$ T/m), which result in trap depths on the order of $0.1 - 1$ K. The temperature of the trapped atoms is at least three orders of magnitude lower such that thermal “evaporation” of atoms can be neglected. In the case of a single trapped atom, atom loss occurs by collisions with thermal background gas atoms. At higher atom numbers, trapped atoms collide inelastically with one another. In these so called “cold collisions”, internal energy is converted into kinetic energy by various mechanisms [22, 24, 25], which usually expels both involved atoms from the trap.

Parameters for trapping single atoms

The magneto-optical trap works remarkably well in collecting and trapping atoms, standard MOTs usually trap $10^3 - 10^{11}$ atoms. In order to reduce this number down to a single trapped atom, we have to drastically lower the loading rate. For this purpose, we first use a very low cesium partial pressure in the background gas of about 10^{-14} mbar [4] instead of the common 10^{-9} mbar used in large MOTs. Second, we operate the MOT at a high magnetic field gradient of about 300 G/cm (3 T/m), which decreases the loading rate, according to eq. (1.6), by four to five orders of magnitude compared to common gradients of < 30 G/cm. Our high field gradient also decreases the diameter of the trapping volume to about 30 µm. This improvement of the localization facilitates the observation of single atoms and their transfer into the dipole trap.

1.1.2 Vacuum system

All our experiments on cold trapped atoms have to be performed in an ultra-high vacuum (UHV) environment, since a collision with a thermal background gas atom or molecule can easily remove a cold atom from our comparatively shallow traps. The residual gas pressure thus ultimately limits the lifetime of the atoms in our trap. A pressure of about 10^{-10} mbar (10^{-8} Pa) corresponds to a lifetime of tens of seconds [4].

The previous experiments in our group [26] used a stainless steel chamber with many windows for optical access. The present experiments require several more laser beams from different directions. Since adding more windows would have made the apparatus large and complex, we use a glass cell, which itself is attached to a conventional stainless steel vacuum apparatus. The glass cell offers maximum optical access in combination with a compact setup. This in turn allows us to place all imaging optics and magnetic coils outside the vacuum, yet close to the trapped atoms. The center of the glass cell is located 5 cm above the optical table, while the vacuum pumps extend

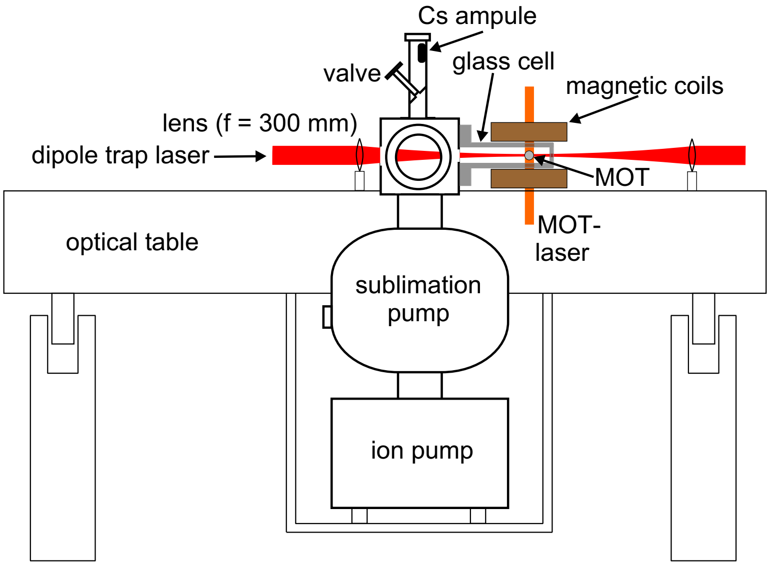

Figure 1.4: The vacuum apparatus is located in a cut-out of the optical table.

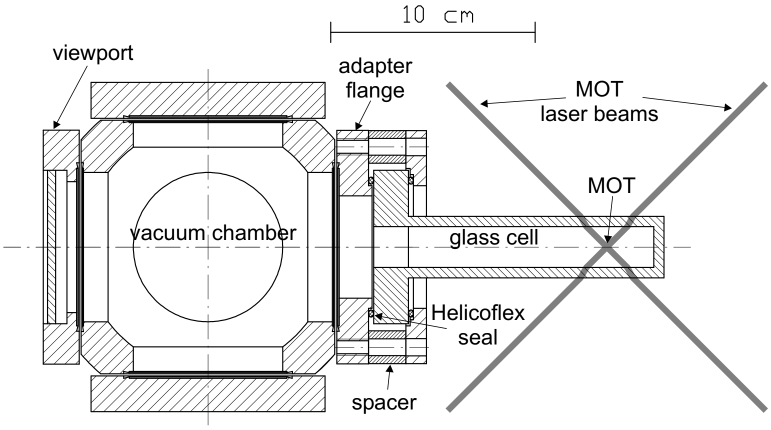

Figure 1.5: Cross section through the glass cell and flange components as viewed from above.

through a cut-out below the optical table, see fig. 1.4.

Glass cell

The glass cell (Hellma, 111.093-VY) consists of a cuboid part of outer dimensions 30 × 30 × 125 mm^3, which is attached to a thick glass disc, see fig. 1.5. It is made of Vycor glass (Corning, VYCOR 7913), which consists of 96% silica. The 5 mm thick windows are optically polished, and anti-reflection coated at the outside (780-850 nm, 0°). The different parts are diffusion-bonded to create air-tight seals without melting the glass which would distort the surface.

The glass disc of the cell is sealed to a modified Conflat flange using a Helicoflex seal (Garlock, HNV-200), which is a bakeable metallic equivalent to an O-ring. An outer jacket made of a soft metal (aluminum) is compressed into the mating surfaces. In our case, a tight seal was achieved only after re-grinding the sealing surface of the glass disc with fine sand paper.

The glass cell is attached to a central stainless steel cube (Kimball Physics, MCF450-SC60008-A) offering six Conflat CF63 flanges. The flange opposite to the glass cell holds a window, the bottom flange connects to the vacuum pumps, and the top flange connects to the cesium reservoir and the pressure gauge.

Vacuum pumps

The central cube is connected to a titanium sublimation pump, which consists of a vacuum chamber with cold shield and baffles (Varian) and a Titanium cartridge (Varian, model 916-0017). An ion getter pump (Varian, VacIon Plus 300 StarCell) connects to the sublimation pump. The apparatus was evacuated initially with a turbo-molecular pump through an auxiliary valve and baked for one week. Due to the delicate Helicoflex seal we limited the bake-out temperature to 90℃ at the cube and about 200℃ at the ion pump. The ion pump operates continuously to maintain the UHV, while the sublimation pump was used only a few times to reduce excessively high cesium gas levels.

Cesium reservoir

The cesium reservoir consists of a T-junction (CF35), a linear motion feed-through and a valve. A sealed glass ampule containing 99% pure cesium metal was fixed inside before bake-out and was broken after bake-out by actuating the mechanical feed-through. The valve isolates the room-temperature cesium vapor pressure of 10^{-6} mbar [27] from the much lower pressures in the main part of the apparatus. The valve is opened for a few minutes only when we want to increase the MOT loading rate.

A UHV pressure gauge (Varian,UHV–24), which is also connected to the top of the central cube, was damaged probably by an over-exposure to cesium vapor.

1.1.3 Magnetic coils

In order to obtain a small number of well-localized atoms in our MOT, we use a magnetic field gradient of $\mathrm{d}B/\mathrm{d}z = 340$ G/cm (3.4 T/m). In previous experiments these fields were produced by permanent magnets [4]. However, present experiments such as Raman cooling and quantum state preparation

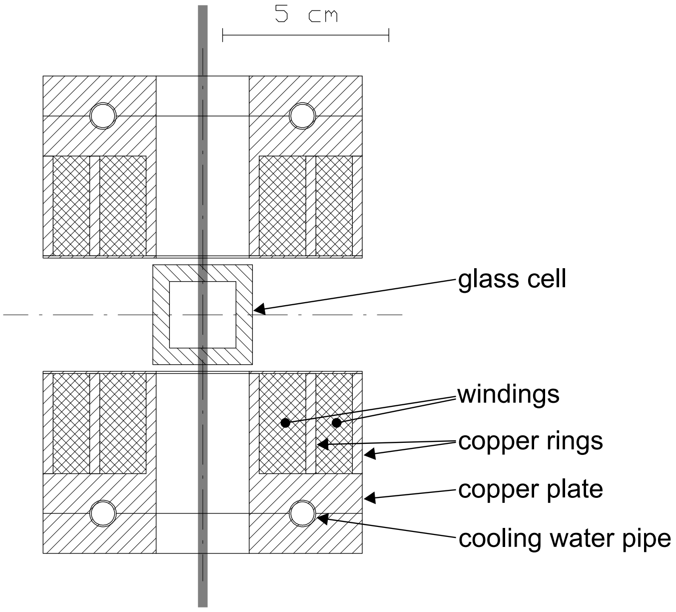

Figure 1.6: Water-cooled magnetic coils supply the quadrupole field for the MOT.

require zero or small homogeneous fields. Therefore, the MOT quadrupole field has to be produced by coils, without the use of ferromagnetic materials.

At the necessary current densities of about 10 A/mm^2, heat dissipation is a major problem. Therefore, the coils are wound on a copper mandril against a water-cooled copper plate. Each coil has about 340 turns of high-temperature enamelled copper wire of 1.4 mm diameter. During the winding process, high quality heat conducting paste (Electrolube HTCP) was spread onto each layer. Additional copper rings enhance heat conduction, see fig. 1.6. The cooling plate and the copper rings are slit to interrupt eddy currents.

From the winding geometry, the magnetic field gradient in z-direction was calculated to be 21.7 G/(cm×A). A later experiment, which measured the magnetic shift of a microwave transition of transported atoms, gave 21.9 G/(cm×A). The coils sustain continuous currents up to 20 A ($\mathrm{d}B/\mathrm{d}z =$ 440 G/cm) and even higher currents for short times.

The power supply (F. u. G. GmbH, NTN 2800–65) and the coils are connected via an electronic control circuit, which switches between “high current” (15.4 A), “low current” (1.5 A) or “off”. It is controlled by a computer via TTL inputs, see appendix C.1 and section 1.3.1. The switching time of the magnetic field is limited by eddy currents within the copper cooling plate, which take about 50 ms to decay.

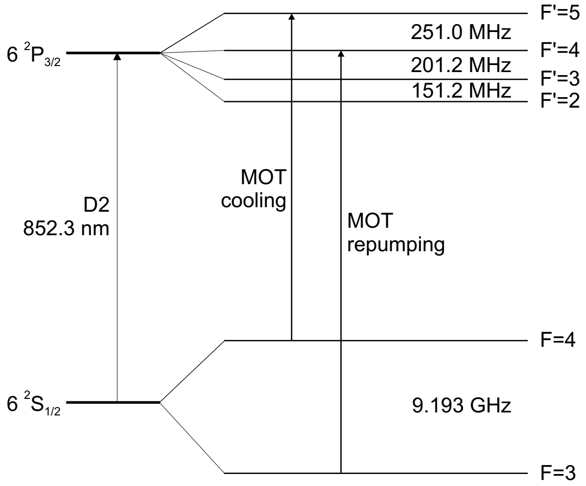

Figure 1.7: Simplified level scheme of the cesium atom. Shown are the transitions used for cooling and repumping in the MOT. Level separations are not drawn to scale.

1.1.4 Laser system

We need several laser sources at the cesium D2 transition (852 nm) for our experiments. The cooling laser operates on the $F = 4 \rightarrow F' = 5$ -transition of the D2 line, see fig. 1.7. There is a small probability of off-resonantly exciting an atom to the $F' = 4$ -level, from where it can decay to the $F = 3$ ground state. Due to the large hyperfine splitting of 9.2 GHz the cooling laser does not excite this level. To return these atoms into the cooling cycle, a repumping laser excites the $F = 3 \rightarrow F' = 4$ -transition, which quickly puts the atoms back to the $F = 4$ ground state.

For state-selective detection of atoms we employ a push-out laser, which operates on the $F = 4 \rightarrow F' = 5$ -transition. For optical pumping to a specific m_F-state we use a laser beam on the $F = 4 \rightarrow F' = 4$ -transition. All lasers are electronically frequency stabilized onto an atomic transition using polarization spectroscopy of cesium vapor cells.

Diode lasers

Because they are comparatively cheap and versatile solid state laser sources, our experiment uses diode lasers except for the dipole trap. Near 852 nm, low and medium power laser diodes (10–150 mW) are readily available, which is also one reason why our experiment uses cesium atoms. The frequency stability and tunability of the bare laser diode are much improved by frequency-selective optical feedback [28]. We use diode lasers with an external cavity in Littrow configuration, where a grating feeds its first order diffracted beam back into the laser diode, whereas the direct (zeroth order)

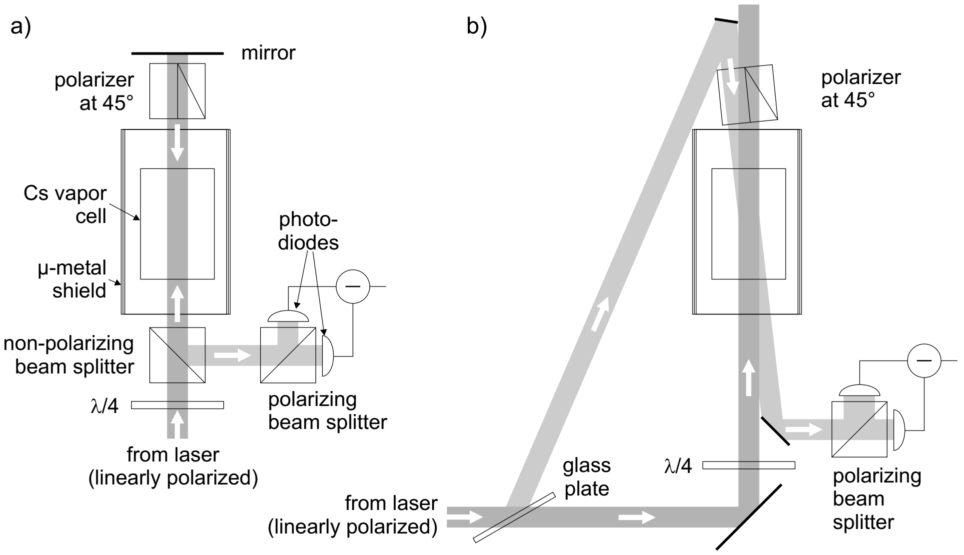

Figure 1.8: Polarization spectroscopy setup. (a) Compact, retro-reflecting version. (b) Setup with an independent probe beam.

reflection constitutes the output beam. The mechanical design originates from the group of T. Hänsch in Garching [29]. The temperature and current controllers were built by our electronic workshop from schematics which also originate from the Hänsch group. Each laser is protected from optical feedback by a 60 dB optical isolator (Gsänger, model FR850TS1).

Polarization spectroscopy

The lasers used to excite specific atomic transitions should have a frequency stability better than the natural linewidths of the transitions, which is 5.2 MHz in our case. Since the frequency of our free-running diode lasers fluctuates over a few MHz within seconds and drifts over hundreds of MHz within hours, an active frequency stabilization onto a stable reference is required. For this purpose, we perform doppler-free polarization spectroscopy [30, 31] in a cesium vapor cell to obtain a dispersive signal on each atomic transition. The polarization spectroscopy itself is a modification of the saturation spectroscopy [32]. It provides a resolution in the order of the natural linewidth, despite a thermal Doppler broadening which is two orders of magnitude larger.

For the stabilization of the repumping laser and the push-out laser we use the compact setup of fig. 1.8 (a). The circularly polarized pump beam is passed through the cesium cell, re-polarized linearly at 45° with respect to the optical table, retro-reflected, and reused as a probe beam. After passing through the cell again, it is coupled out by a 50% non-polarizing beam splitter cube and is directed onto a polarizing beam splitter cube. Its two outputs are monitored by photodiodes, whose signals are substracted to yield the dispersive signal.

This simple setup has two disadvantages. Because the beam passes the cesium cell twice, the laser power on the photodiodes is reduced in the center of the absorption profile, which decreases the signal height. Additionally, due to reflections off the many surfaces in the beam path, the photodiode signal always shows optical interferences. They convert vibrations and drifts of the optical elements (in the µm range) into sinusoidal fluctuations of the signal offset. Although all optical elements, except the cesium cell, are anti-reflection coated, and we slightly tilt all surfaces with respect to the laser beam axis (to avoid direct back-reflections), the interferences are still visible above the noise floor of the signal.

We found that the more traditional setup of fig. 1.8 (b) with independent probe beam avoids these difficulties and gives a cleaner signal. The small angle between pump and probe beam axis of about 2° only causes a small residual doppler broadening. This is, however, in the same order of magnitude as the power broadening, which we accept in exchange for a larger signal amplitude.

Magnetic shielding of the cesium cell is important, since the polarization spectroscopy relies on optically pumping the atoms. We use several layers of µ-metal sheet wrapped around the cell. The magnetic shield is then carefully demagnetized. This treatment increases the signal amplitude and decreases the apparent width of the lines.

When the diode laser is locked to an atomic transition, the dispersive spectroscopic signal serves as error-signal. It is fed into a servo amplifier, which is a proportional-integral amplifier with adjustable gain and input offset. The output of the servo amplifier is connected to the piezoelectric actuator which moves the grating of the diode laser, and thus controls the laser frequency.

The mechanical action of the piezoelectric actuator limits the servo bandwidth to a few hundred Hertz. A more stable lock is achieved by additionally feeding the error signal through a fast integrator onto the current of the laser diode. The current acts as a fast control of the laser frequency and allows servo bandwidths on the order of 1 MHz. This system is used for the cooling laser, and an emission linewidth of the locked laser of 100 kHz was measured in a beat signal with a very stable Hollberg laser [33].

Laser setup

The four diode lasers are located on a separate optical table to save space on the main table. Electronically controlled mechanical shutters (Vincent Associates, Uniblitz LS2 T2) are used to switch on and off each laser beam with a switching time of < 100 µs. The light is then transferred by single mode, polarization maintaining optical fibers (3M, FS PM 4621) to the experiment. Most lasers fulfill several tasks in the experiment:

Cooling laser: The cooling laser is locked to the crossover signal of the $F = 4 \rightarrow F' = 3$ and the $F = 4 \rightarrow F' = 5$ transitions, such that it emits about 225 MHz below the cooling transition ($F = 4 \rightarrow F' = 5$). We use an acousto-optical modulator (AOM) in double pass configuration to shift the frequency of the laser light upwards by almost that amount. The use of an AOM allows us to control the detuning and the intensity of the cooling laser beams electronically. On the main experiment table, the laser beam exiting the fiber output coupler is split up, circularly polarized and shined in along three orthogonal directions for the MOT. Behind the vacuum cell, the polarization of each beam is changed by passing twice through a $\lambda/4$-plate as it is retro-reflected and used as counter-propagating beam.

For optical pumping on the $F = 4 \rightarrow F' = 4$ transition, a part of the unshifted cooling laser radiation is used, since the $F' = 3 - F' = 5$ crossover is located only 25 MHz to the blue of that transition. The small residual detuning is approximately compensated by the light shift of the atomic transitions in the dipole trap, see sec. 1.2.2.

The cooling laser is also used as a frequency reference in the high finesse cavity setup, see section 3.

Repumping laser: The repumping laser is locked to the $F = 3 \rightarrow F' = 4$ transition. It is either overlapped onto the vertical MOT cooling beam, or it is shined in along another axis onto the MOT. Due to the low scattering rate of the repumping laser in the MOT, compared to the cooling laser, its polarization is irrelevant for the MOT operation, and can be chosen to aid specific optical pumping tasks.

Push-out laser This laser is locked to the $F = 4 \rightarrow F' = 5$ transition, and is used for state-selective detection. It is sent to the experiment either through its own optical fiber, or through the fiber used for the optical pumping beam.

1.1.5 Fluorescence imaging and detection

The presence of a single atom in a MOT can be detected by its fluorescence light, as was experimentally demonstrated by several groups [34, 35, 4] in the mid-90's. The keys to success are efficient collection of fluorescence, suppression of stray light and sensitive detectors.

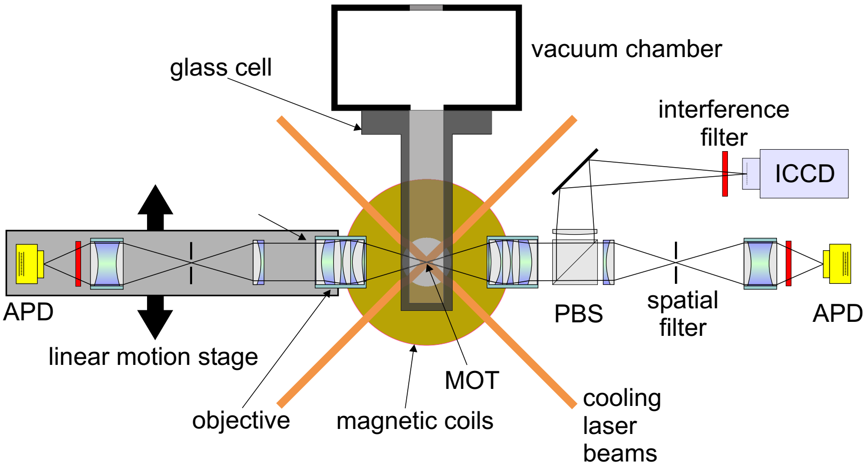

Figure 1.9: Detection setup for the MOT fluorescence, as viewed from above. ICCD: intensified CCD-camera, APD: avalanche photodiode, PBS: polarizing beam splitter.

Imaging optics

Since the atomic fluorescence is emitted isotropically, it is advantageous to collect the fluorescence light from a solid angle as large as possible. For this purpose we use an objective lens outside the vacuum, placed close to the glass cell, see fig. 1.9. The design, test and implementation of the objective lens system is described in detail in appendix B, and is published in [36]. In order to maximize the solid angle covered, the numerical aperture of the objective is chosen as high as possible, given the tight spatial constraints imposed by the MOT laser beams, the magnetic coils and the glass cell. Although placing a lens inside the vacuum close to the MOT could in principle cover a larger solid angle, mounting a lens within the small glass cell is at least cumbersome, and it would not admit the movable detection axis described below.

The working distance of the objective was designed such that the reflections of the four MOT laser beams, which intersect the glass cell at a 45° angle, off the inner cell surface just misses the entrance aperture. The reflection off the outer surface is blocked by tubes which enclose the MOT beams.

In order to guide the collected fluorescence light to the detector while keeping stray light away, the fluorescence light is spatially filtered. The MOT is imaged onto a small aperture of 150 µm diameter, which essentially blocks rays not originating from a region of 67 µm diameter around the MOT, about twice the visible MOT size. Effective filtering of stray light is of utmost importance, since a single atom, illuminated by six laser beams with a total power of ~ 1 mW, scatters only 3 pW, of which typically 60 fW reach the detector. A good spatial separation of stray light requires high quality optical imaging. Therefore, the whole imaging system is optimized for diffraction limited resolution.

The actual detection of the fluorescence photons takes place in two avalanche photodiodes (APD) and an intensified CCD camera. Interference filters (Dr. Hugo Anders) in front of the detectors transmit 80% at 852 nm, but attenuates ambient laboratory light and straylight of the dipole trap laser (1064 nm) by 10^{-4}. One of the APD detection assemblies can be moved by a linear translation stage together with the imaging optics. This feature is used to demonstrate the operation of the optical conveyor belt (section 1.3.3).

Detection with avalanche photodiodes

For high-speed single photon detection we use integrated single photon counting modules (EG&G Canada, SPCM200 CD2027). They contain a temperature stabilized silicon APD in a passively quenched circuit together with a high voltage module. A photon of $\lambda = 852$ nm, which hits the sensitive area of 150 µm diameter, produces an output pulse with a probability (= quantum efficiency) of about 50%. The low dark count rate of only 30 counts/s allows sensitive measurements, and via the sub-nanosecond time resolution even fast atomic dynamics can be decoded from the fluorescence radiation [37].

The signal from the APD is processed by a multi-channel scaler (EG&G Ortec, Turbo-MCS 914), which is used to count the number of pulses within 100 ms time intervals. This information is recorded and continuously displayed by a computer for visual inspection of the MOT operation. Additionally, the arrival time of each single photon pulse is recorded with 50 ns resolution by a custom-built timer card (Silicon Solutions, TimerCard 3.0). Controlled by a TTL gate input, this data is directly written into a file on another computer. After the experiment, these files are then processed by a software which is able to bin the counts into arbitrary time intervals and to automatically extract essential information such as atom numbers or fluorescence rates [5].

We primarily use the fluorescence to determine the exact number of atoms in the MOT. Fig. 1.10 shows a typical record of the APD count rate versus time, integrated over intervals of 100 ms. After switching on the trap at $t = 0$, only stray light of the MOT lasers ($2 \cdot 10^4$ counts/s) is visible. At $t = 2$ s one cesium atom is captured from the background gas, and its fluorescence increases the count rate by $6 \cdot 10^4$ counts/s. Since each atom contributes the same amount of fluorescence, the number of atoms in the trap can be inferred directly from the discrete levels of the count rate. A simultaneous loss of two atoms indicates inelastic cold collisions [25, 22].

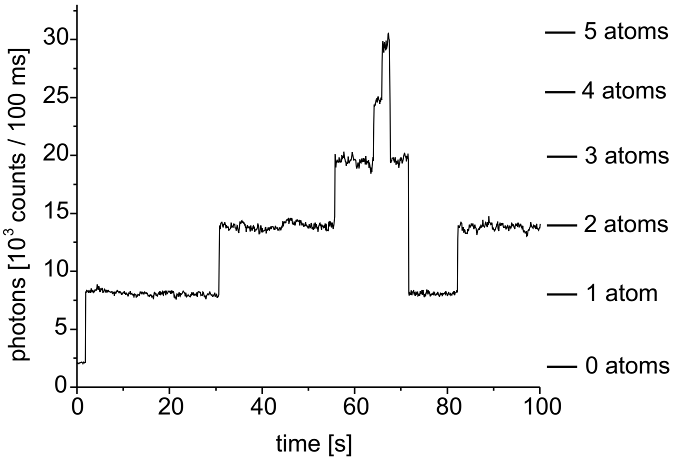

Figure 1.10: Count rate of the APD detecting the fluorescence the MOT. Each trapped atom contributes the same amount of fluorescence to the signal. When an atom enters or leaves the trap, the count rate suddenly increases or decrease accordingly. The number of trapped atoms can thus be determined from the fluorescence count rate.

Efficiency of fluorescence collection

The upper limit of the fluorescence count rate of a single atom can be estimated from equation (1.1) in the limit of strong saturation. In this limit, the atom scatters $\Gamma/2 = 1.6 \cdot 10^7$ photons/s into 4π solid angle, of which the objective lens covers $\eta_{\rm obj} = 2.1\%$. Together with the quantum efficiency $\eta_{\rm APD} = 50\%$ of the APD we find a maximum count rate of

$$R = \eta_{\rm obj}\eta_{\rm APD}\frac{\Gamma}{2} = 1.7 \cdot 10^5. \tag{1.7}$$

Experimentally, a maximum rate per atom of about $8 \cdot 10^4$ counts/s was observed with high cooling laser intensity ($I/I_0 \approx 80$) and small detuning ($\Delta \approx \Gamma$). The missing factor of two is probably due to several reasons. In the optical path there are a total of 16 optical surfaces, 15 of which are anti-reflection coated. Assuming losses of 0.5% and 4% for coated and uncoated surfaces, respectively, the total transmission is 89% (the interference filters were not installed at that time). In a MOT, the 6 circularly polarized laser beams create complex interference patterns with various local polarizations and possibly dark spots [38]. This can reduce the fluorescence rate from equation (1.1) by a factor of 0.7 [39].

Atom counting

The exact number of atoms can only be determined from the fluorescence within a given time interval Δt: One additional atom has to increase the number of fluorescence counts by more than the statistical fluctuations. This limit can be estimated under the assumption that the fluctuations of the number of counts are only due to the statistical nature of the photon scattering process, and not due to variations of external parameters such as laser intensities or detunings. In this case the actual number of counts N in the interval Δt is distributed around the mean value $\overline{N}$ according to Poissonian statistics. For $\overline{N} \gg 1$ this can be approximated by a Gaussian distribution of standard deviation $\Delta N = \sqrt{\overline{N}}$.

The average number of counts $\overline{N}(n)$ for n atoms in the MOT in the time interval Δt is given by

$$\overline{N}(n) = (R_\mathrm{s} + nR_\mathrm{a})\Delta t, \tag{1.8}$$

where R_s and R_a are the count rates produced by stray light and one atom, respectively. To decide whether a measured N corresponds to n or to $n+1$ atoms, we place the cut halfway between $\overline{N}(n)$ and $\overline{N}(n+1)$. The decision is correct with 95% probability (confidence), if the cut is $2\Delta N$ (two standard deviations) away, i. e. if $\overline{N}(n+1) - \overline{N}(n) = 4\Delta N$, which yields

$$n = \frac{R_\mathrm{a}^2 \Delta t - 16 R_\mathrm{s}}{16 R_\mathrm{a}}. \tag{1.9}$$

Using the values given above for R_s and R_a, we find that the atoms can be counted up to $n = 3$ within $\Delta t = 1$ ms and theoretically to $n > 300$ within $\Delta t = 100$ ms. The maximum count rate of the APD of 10^6 counts/s, however, limits the maximum observable number of atoms to about 15 in our case.

We initially observed slow fluctuations of the single atom fluorescence rate of ±10% over a few seconds, which impaired our atom counting abilities and disturbed the dipole trap alignment procedure (sec. 1.2.3). These fluctuations were caused by changes of the optical path length of the three axes of the MOT cooling laser in the order of the optical wavelength. Their influence on the atoms can be explained by two mechanisms. First, the three MOT laser beam paths act as (very low finesse) Fabry-Perot resonators, because the light is retroreflected at the far end of each axis, and a small amount ($\sim 4\%$) is reflected again at the output end face of the optical fiber which delivers the laser beam to the experiment. Indeed, we found that a photodiode signal monitoring the cooling laser power at the fiber output showed fluctuations correlated with the fluorescence count rate. A second mechanism is the change in the complex interference pattern due to fluctuations of the relative phase of the beams, which could also influence the fluorescence rate [38].

A simple solution to this problem is to continuously modulate all optical path lengths, such that an average over all different interference phases is obtained within the integration time of typically 100 ms. Initially this was achieved by exciting an eigenresonance of the optical table by a mechanical shaker. Now, the three retroreflecting mirrors of the MOT are mounted on piezoelectric actuators and are dithered with a few hundred Hertz. The remaining count rate fluctuations are purely Poissonian [5].

Detection with ICCD camera

For imaging single atoms in the MOT as well as in the dipole trap we use an intensified CCD (ICCD) camera. Half of the fluorescence light collected by the fixed objective lens is split off by a polarizing beam splitting cube and focused onto the image intensifier, see fig. 1.9.

Although a single atom in a MOT emits enough fluorescence to be observed directly by a low noise CCD chip [4], an exposure time of several seconds is required. The fluorescence rate is even lower inside the dipole trap. For this reason we use an image intensifier (Roper Scientific, GEN III HQ). This intensifier incorporates a special GaAs photocathode, which is specified to have a quantum efficiency of about 30% at 852 nm. At full amplification, each photoelectron is amplified by the multi-channel electron multiplier to a bunch of $\sim 10^6$ electrons. The light they produce on the phosphorous screen is guided by a bundle of optical fibers to the CCD chip. In this way, a single incoming photon can be detected far above the noise floor of our low noise, high resolution CCD camera (Roper Scientific, PI-MAX:1K, 1024 × 1024 pixel).

The magnification of our imaging optics of about 14 was chosen to have 1 µm at the MOT correspond roughly to one pixel (13 µm squared) of the camera. The diffraction-limited spot size of 1.8 µm (airy disk radius at the object plane) is thus distributed over several pixels. This should allow us to determine the position of a point source with sub diffraction-limited precision by fitting the intensity distribution of its image.

The exact value of the total magnification, including the image intensifier, was determined experimentally by observing an atom in the dipole trap (see sec. 2.5.2) while transporting it over a precisely known distance of 60 µm (see sec. 1.3.3). The experimental value of the magnification is 14.0 ± 0.1, or 0.929 ± 0.007 µm per pixel [40].

An image of two atoms in the MOT as well as in the dipole trap is shown in chapter 2 in fig. 2.17.

1.2 Dipole trap

The optical dipole trap constitutes a versatile tool for the manipulation of cold neutral atoms. It is based on the attraction of the induced electric dipole moment of a polarizable particle into regions of high electric field strength. It was thus proposed by Letokhov in 1968 [41], that the electric field of a laser beam can attract atoms into regions of high intensity. A similar trap for small dielectric particles using laser beams was proposed by Ashkin [42]. This method is used in e. g. biological experiments as "optical tweezers" [43]. After the first demonstration of trapped sodium atoms in 1986 [44], dipole traps became a valuable, widely used tool for the manipulation of neutral atoms [45]. Their laser frequency can be detuned very far from all atomic resonances, so that it is possible to store atoms without continuous excitation, in contrast to radiation pressure traps such as the MOT. Long-lived internal states can thus be preserved and used for spectroscopic experiments or as quantum memories.

A great variety of trap shapes can be produced, according to the many possible light configurations which can be attained with laser beams and interference patterns. We use a standing wave dipole trap to perform controlled transportation of our atoms. The dipole trap furthermore allows us to prepare, manipulate and read out the internal states of the atoms, and to directly observe individual atoms spatially resolved.

1.2.1 Classical model of the dipole force

The classical model provides a basic, intuitive description of the origin of the dipole force [45]. Nevertheless, its predictions are good approximations to the quantum-mechanical treatment.

Lorentz model

The electric component of a monochromatic light field $\mathbf{E}(t) = \mathbf{E}_0 \exp(i\omega t) + c.c.$ induces an electric dipole moment $\mathbf{d} = \alpha\mathbf{E}$ in the atom, where α is the (complex) atomic polarizability. The atom is considered here as an electron (mass m_e, electric charge $-e$), elastically bound to the core (mass $M \gg m_e$, charge $+e$) by an harmonic potential, and damped with an energy decay rate Γ due to dipole radiation (Lorentz's model).

The electric component of the light field drives the electron according to the equation of motion

$$\ddot{\mathbf{x}} + \Gamma_\omega \dot{\mathbf{x}} + \omega_0^2 \mathbf{x} = -e\mathbf{E}(t). \tag{1.10}$$

Here,

$$\Gamma_\omega = \frac{e^2\omega^2}{6\pi\epsilon_0 m_e c^3} \tag{1.11}$$

is the energy damping rate due to classical dipole radiation of the oscillating electron [46]. The stationary solution of (1.10) yields the polarizability via $\mathbf{d}(t) = -e\mathbf{x}(t) = \alpha\mathbf{E}(t)$ as

$$\alpha = \frac{e^2}{m_e} \frac{1}{\omega_0^2 - \omega^2 + i\Gamma_\omega\omega}. \tag{1.12}$$

By substituting $e^2/m_e = 6\pi\epsilon_0 c^3 \Gamma_\omega/\omega^2$ and introducing the on-resonance damping rate $\Gamma \equiv \Gamma_{\omega_0} = (\omega_0/\omega)^2\Gamma_\omega$ we obtain

$$\alpha = 6\pi\epsilon_0 c^3 \frac{\Gamma/\omega_0^2}{\omega_0^2 - \omega^2 + i\frac{\omega^3}{\omega_0^2}\Gamma}. \tag{1.13}$$

Potential depth

The dipole potential U is the interaction potential of the induced dipole moment $\mathbf{d}$ in the electric field $\mathbf{E}$

$$U = -\frac{1}{2}\mathbf{d}\cdot\mathbf{E}. \tag{1.14}$$

The factor 1/2 reflects the fact that $\mathbf{d}$ is an induced dipole moment which builds up as the atom moves into regions of higher field strength.

Since the electric field is time dependent, the effective potential depth is the time average over one oscillation period (denoted by $\langle\cdots\rangle$)

$$U = -\frac{1}{2}\langle\mathbf{d}\cdot\mathbf{E}\rangle = -|\mathbf{E}_0|^2\mathrm{Re}(\alpha). \tag{1.15}$$

With the intensity $I = 2\epsilon_0 c|\mathbf{E}_0|^2$ the potential depth can be expressed as

$$U(\mathbf{x}) = -\frac{I(\mathbf{x})}{2\epsilon_0 c}\mathrm{Re}(\alpha). \tag{1.16}$$

The dipole trap depth is thus proportional to the intensity I and to the real part of the polarizability α, which describes the in-phase component of the atomic dipole moment. The gradient of the potential yields the dipole force $\mathbf{F}(\mathbf{x}) = -\nabla U(\mathbf{x})$.

Scattering rate

Due to the damping rate Γ, the atom absorbs energy from the dipole trap laser. The average absorbed power is

$$P = \langle\dot{\mathbf{d}}\cdot\mathbf{E}\rangle = -\frac{I(\mathbf{x})\omega}{\epsilon_0 c}\mathrm{Im}(\alpha). \tag{1.17}$$

It is proportional to the intensity I and to the imaginary part of the polarizability α, which describes the out-of-phase component of the atomic dipole moment. Whereas classically the power is reradiated continuously, in the corresponding quantum mechanical process, photons are emitted at the rate

$$R_\mathrm{s} = \frac{P}{\hbar\omega} = -\frac{I}{\hbar\epsilon_0 c}\mathrm{Im}(\alpha). \tag{1.18}$$

Photon scattering heats up the atoms (sec. 2.4) and limits the lifetime of internal states [26].

For the practical case of a detuning much larger than the natural linewidth ($|\omega_0 - \omega| \gg \Gamma$) we can derive expressions for the trap depth and the scattering rate:

$$U = \frac{-3\pi c^2}{2} \frac{I\Gamma}{\omega_0^3} \left(\frac{1}{\omega_0 - \omega} + \frac{1}{\omega_0 + \omega} \right) \tag{1.19a}$$

$$R_\mathrm{s} = \frac{3\pi c^2 I \Gamma^2}{2\hbar\omega_0^3} \frac{\omega^3}{\omega_0^3} \left(\frac{1}{\omega_0 - \omega} + \frac{1}{\omega_0 + \omega} \right)^2 . \tag{1.19b}$$

If the detuning $\Delta \equiv \omega - \omega_0$ is still small compared to the optical frequency ω_0 these expressions are further simplified by the so called rotating wave approximation to

$$U = \frac{3\pi c^2}{2} \frac{I}{\omega_0^3} \frac{\Gamma}{\Delta} \tag{1.20a}$$

$$R_\mathrm{s} = \frac{3\pi c^2 I}{2\hbar\omega_0^3} \frac{\Gamma^2}{\Delta^2} \tag{1.20b}$$

$$= \frac{\Gamma}{\hbar\Delta} U. \tag{1.20c}$$

We see from eq. (1.20a) that the sign of the dipole potential depends on the sign of the detuning Δ. For a laser tuned below the resonance frequency ($\Delta < 0$, red detuning) the dipole potential is negative, and the atom is attracted into the high intensity regions. This is analogous to the static case, where polarizable dielectric particles are always pulled into the regions of high electric fields. In contrast, a blue detuned laser beam ($\Delta > 0$) pushes the atom away from regions of high intensity, because above resonance, the atomic dipole oscillates nearly 180° out of phase. The expression (1.20c) for R_s shows that, for a given potential depth, a low scattering rate can be obtained by using a large detuning. Of course, the intensity has to be increased proportionally to maintain the trap depth.

Multi-level atoms

For cesium atoms, the multitude of resonance transitions to different excited states poses a problem to the direct application of the classical model (see fig. 1.12). However, they can be approximately taken into account by applying equations (1.19) to each transition separately and adding up the results weighted with each transition's oscillator strength f_osc. The oscillator strength of a transition is a measure for the fraction of "classical" harmonically bound electrons needed to explain the transition rate and absorption cross-section. Theoretical oscillator strengths can be obtained from approximated electron wavefunctions [47]. For the cesium D-lines, however, they can be calculated more precisely from the experimentally known linewidths, because in these cases the excited 6P states decay only to a single level, the

$6S_{1/2}$ ground state. In this case, the relation which connects decay rates to oscillator strengths reads [47]

$$\Gamma = \frac{e^2\omega^2}{2\pi\epsilon_0 m_e c^3}\frac{g_\mathrm{g}}{g_\mathrm{e}} f_\mathrm{osc}, \tag{1.21}$$

where g_e and g_g are the degeneracies of the excited and ground state, respectively. With Γ_D1 and Γ_D2 from appendix A we obtain $f_\mathrm{osc,D1} = 0.344$ and $f_\mathrm{osc,D2} = 0.714$.

In a Nd:YAG laser trap ($\lambda = 1064$ nm), only the D1- and the D2-transition contribute significantly to the dipole force; the relative contribution of the next strongest transition (to the $7P_{3/2}$ level) is only $3 \cdot 10^{-5}$. We thus have

$$\begin{aligned}
U &= \frac{-3\pi c^2 I}{2}\Big[f_\mathrm{osc,D1}\frac{\Gamma_\mathrm{D1}}{\omega_\mathrm{D1}^3}\left(\frac{1}{\omega_\mathrm{D1}-\omega}+\frac{1}{\omega_\mathrm{D1}+\omega}\right) + && \text{(1.22a)}\\
&\quad + f_\mathrm{osc,D2}\frac{\Gamma_\mathrm{D2}}{\omega_\mathrm{D2}^3}\left(\frac{1}{\omega_\mathrm{D2}-\omega}+\frac{1}{\omega_\mathrm{D2}+\omega}\right)\Big] && \text{(1.22b)}\\
R_\mathrm{s} &= \frac{3\pi c^2 I}{2\hbar}\Big[f_\mathrm{osc,D1}\frac{\Gamma_\mathrm{D1}^2\omega^3}{\omega_\mathrm{D1}^6}\left(\frac{1}{\omega_\mathrm{D1}-\omega}+\frac{1}{\omega_\mathrm{D1}+\omega}\right)^2 + && \text{(1.22c)}\\
&\quad + f_\mathrm{osc,D2}\frac{\Gamma_\mathrm{D2}^2\omega^3}{\omega_\mathrm{D2}^6}\left(\frac{1}{\omega_\mathrm{D2}-\omega}+\frac{1}{\omega_\mathrm{D2}+\omega}\right)^2\Big]. && \text{(1.22d)}
\end{aligned}$$

The above equations are often approximated in various ways, e. g. by applying the rotating-wave approximation and by combining the D1- and the D2-transition into a single transition with an “effective detuning”. This approach yields simpler formulas in the form of (1.20) as used in [48], which, however, underestimate the trap depth by 14% and, at the same time, overestimate the scattering rate by 60%.

1.2.2 Quantum-mechanical description

A useful quantum-mechanical description of the dipole force originates from the “dressed-state” picture of the atom-light interaction [49]. In this approach, the energy eigenstates of the atom are replaced by combined states of the atom and the quantized dipole trap laser field. The combined states are then coupled, and the resulting new energy eigenstates (dressed states) are shifted in energy by the interaction. The dipole trapping potential results from this light shift (AC Stark shift). Finally, the dressed states are coupled to the empty modes of the electromagnetic field so that they can be assigned individual transition rates, lifetimes etc., as in the case of ordinary atomic levels.

Hamilton operator

As a simple case we consider a two-level atom at rest, interacting with the dipole trap laser beam. The Hamilton operator of the combined system consists of three parts:

$$\hat{H} = \hat{H}_{\mathrm{A}} + \hat{H}_{\mathrm{L}} + \hat{V}. \tag{1.23}$$

The atomic Hamiltonian $\hat{H}_{\mathrm{A}}$ describes a two-level system with ground and excited states, $|\,g\,\rangle$ and $|\,e\,\rangle$, with energy spacing $\hbar\omega_0$,

$$\hat{H}_{\mathrm{A}} = \hbar\omega_0 |\,e\,\rangle\langle\,e\,|. \tag{1.24}$$

The dipole trap laser is modeled as a single mode of the electromagnetic field containing n photons of energy $\hbar\omega$. Following the book of C. Cohen-Tannoudji [50], one can imagine this as a beam circulating around between ideal mirrors in a closed loop. For the atom, this situation is equivalent to the continuous stream of new photons from an actual laser, as long as n is reasonably constant. The Hamiltonian of the light field $\hat{H}_{\mathrm{L}}$ thus reads

$$\hat{H}_{\mathrm{L}} = \hbar\omega\hat{a}^{+}\hat{a}, \tag{1.25}$$

where $\hat{a}^{+}$ and $\hat{a}$ are creation and annihilation operators of a photon in the mode.

The energy eigenstates of $\hat{H}_{\mathrm{A}} + \hat{H}_{\mathrm{L}}$ are denoted by $|\,g,n\,\rangle$ and $|\,e,n\,\rangle$. They form a ladder of level pairs separated by $\hbar\omega$, where the states within a pair are separated by the detuning $\hbar\Delta = \hbar(\omega - \omega_0)$, see fig. 1.11.

Let $\boldsymbol{\mathcal{E}}(\mathbf{x})$ be the mode distribution of the recirculating laser beam, such that the electric field operator $\hat{\mathbf{E}}(\mathbf{x})$ of the laser mode reads

$$\hat{\mathbf{E}}(\mathbf{x}) = \boldsymbol{\mathcal{E}}(\mathbf{x})\hat{a} + \boldsymbol{\mathcal{E}}^{*}(\mathbf{x})\hat{a}^{+}, \tag{1.26}$$

which implies the normalization

$$\epsilon_0 \iiint_V \left(\boldsymbol{\mathcal{E}}(\mathbf{x})^2 + \boldsymbol{\mathcal{E}}^{*}(\mathbf{x})^2\right) \mathrm{d}^3\mathbf{x} = \hbar\omega_0. \tag{1.27}$$

The atomic dipole moment is

$$\begin{aligned} \mathbf{d} &= \langle\,e\,|\,\hat{\mathbf{d}}\,|\,g\,\rangle \\ \mathbf{d}^{*} &= \langle\,g\,|\,\hat{\mathbf{d}}\,|\,e\,\rangle. \end{aligned} \tag{1.28}$$

Here, $\hat{\mathbf{d}}$ is the dipole moment operator, which can be written as

$$\hat{\mathbf{d}} = \mathbf{d}|\,e\,\rangle\langle\,g\,| + \mathbf{d}^{*}|\,g\,\rangle\langle\,e\,|. \tag{1.29}$$

The coupling Hamiltonian $\hat{V} = -\hat{\mathbf{d}} \cdot \hat{\mathbf{E}}$ then reads

$$\begin{aligned} \hat{V} = {} & -(\mathbf{d} \cdot \boldsymbol{\mathcal{E}}\,\hat{a}|\,e\,\rangle\langle\,g\,| + \mathbf{d} \cdot \boldsymbol{\mathcal{E}}^{*}\,\hat{a}^{+}|\,e\,\rangle\langle\,g\,| + \\ & +\mathbf{d}^{*} \cdot \boldsymbol{\mathcal{E}}\,\hat{a}|\,g\,\rangle\langle\,e\,| + \mathbf{d}^{*} \cdot \boldsymbol{\mathcal{E}}^{*}\,\hat{a}^{+}|\,g\,\rangle\langle\,e\,|). \end{aligned} \tag{1.30}$$

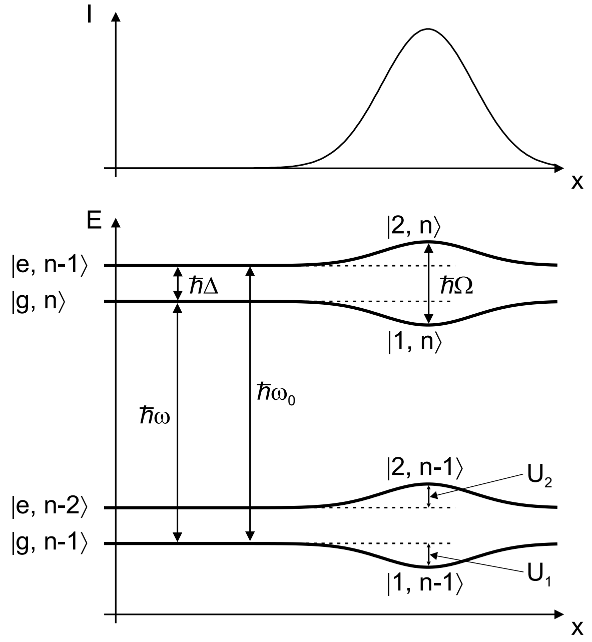

Figure 1.11: Dressed states of a two-level atom in a strong red-detuned laser field. When the atom enters the laser beam of Gaussian intensity profile (top curve), the interaction mixes and shifts the levels, which results in a position dependent dipole potential.

The first and last term of operator (1.30) couple the states $|\,g,n\,\rangle$ and $|\,e,n-1\,\rangle$ which are separated by Δ, whereas the other two terms couple the states $|\,g,n\rangle$ and $|\,e,n+1\rangle$, which are separated by $\omega_0+\omega \gg \Delta$, i. e. much further (see fig. 1.11). Since this large separation reduces the effect of the coupling, the corresponding terms are neglected. This so called rotating wave approximation greatly simplifies the following calculation.

The interaction now couples only the states within each pair by

$$\langle\, e,n-1\,|\,\hat{V}\,|\,g,n\,\rangle = -\mathbf{d}\cdot\boldsymbol{\mathcal{E}}\sqrt{n}\,. \tag{1.31}$$

Although the coupling strength actually depends on the number of photons n, we assume here that the light field is in a coherent state $|\,\alpha e^{i\omega t}\,\rangle$ which contains $\langle n\rangle = |\alpha|^2$ photons, and that $\langle n\rangle \gg \Delta n \gg 1$ can be regarded as constant, despite the poissonian uncertainty $\Delta n = \sqrt{\langle n\rangle}$ and the absorption of photons by the atom. The expectation value of the electric field operator,

$$\begin{aligned}\mathbf{E} &= \langle\,\alpha e^{i\omega t}\,|\,\hat{\mathbf{E}}\,|\,\alpha e^{i\omega t}\,\rangle \\ &= \left(\boldsymbol{\mathcal{E}}e^{i\omega t}+\boldsymbol{\mathcal{E}}^{*}e^{-i\omega t}\right)\sqrt{n},\end{aligned} \tag{1.32}$$

acts like a classical field on the atomic dipole moment $\mathbf{d}$, which is why we introduce the Rabi frequency Ω_{R} in analogy to the Bloch vector model as

$$\hbar\Omega_{\mathrm{R}} = (\mathbf{d}\cdot\boldsymbol{\mathcal{E}}+\mathbf{d}^{*}\cdot\boldsymbol{\mathcal{E}}^{*})\sqrt{n}. \tag{1.33}$$

For the case of linear polarization of the laser light, we can choose $\mathbf{d}$ and $\boldsymbol{\mathcal{E}}$ to be real, and thus

$$\hbar\Omega_{\mathrm{R}} = 2\mathbf{d}\cdot\boldsymbol{\mathcal{E}}\sqrt{n}. \tag{1.34}$$

The new eigenstates

To find the new eigenstates, we diagonalize the total Hamiltonian $\hat{H}$ on the subspace spanned by the states $\{|\,g,n\,\rangle,\ |\,e,n-1\,\rangle\}$ which are coupled by the atom-field-interaction. In this basis

$$\hat{H} = \hbar\begin{pmatrix} n\omega & \frac{1}{2}\Omega_{\mathrm{R}} \\ \frac{1}{2}\Omega_{\mathrm{R}} & n\omega-\Delta \end{pmatrix}. \tag{1.35}$$

The eigenvalues of $\hat{H}$ are

$$\begin{aligned} \frac{E_1}{\hbar} &= n\omega - \frac{\Delta}{2} - \frac{1}{2}\sqrt{\Omega_{\mathrm{R}}^2+\Delta^2} && (1.36\mathrm{a}) \\ \frac{E_2}{\hbar} &= n\omega - \frac{\Delta}{2} + \frac{1}{2}\sqrt{\Omega_{\mathrm{R}}^2+\Delta^2}, && (1.36\mathrm{b}) \end{aligned}$$

i. e. the states are repelled by the interaction. In the case of negative detuning $\Delta < 0$, the lower state, which connects to the atomic ground state, is shifted downwards by $U_1 = -(\Delta + \sqrt{\Omega_{\mathrm{R}}^2+\Delta^2})/2$ when the atom in moved into the laser beam, whereas the excited (upper) state is shifted upwards by the same amount, see fig. 1.11. The dipole trap potential for an atomic level is thus its light shift (AC Stark shift). In the limit of far detuning $|\Delta| \gg \Omega_{\mathrm{R}}$, an approximation to first order of $\Omega_{\mathrm{R}}/\Delta$ yields simple formulas for the energy shifts

$$\begin{aligned} U_1 &= -\frac{\Omega_{\mathrm{R}}^2}{4\Delta} && (1.37\mathrm{a}) \\ U_2 &= \frac{\Omega_{\mathrm{R}}^2}{4\Delta} && (1.37\mathrm{b}) \end{aligned}$$

and the for new eigenstates

$$\begin{aligned} |\,1,n\,\rangle &= \left(1-\frac{\Omega_{\mathrm{R}}^2}{8\Delta^2}\right)|\,g,n\,\rangle + \frac{\Omega_{\mathrm{R}}}{2\Delta}|\,e,n-1\,\rangle && (1.38\mathrm{a}) \\ |\,2,n\,\rangle &= -\frac{\Omega_{\mathrm{R}}}{2\Delta}|\,g,n\,\rangle + \left(1-\frac{\Omega_{\mathrm{R}}^2}{8\Delta^2}\right)|\,e,n-1\,\rangle. && (1.38\mathrm{b}) \end{aligned}$$

Scattering rates

Since only the excited state of the atom can decay by spontaneous emission, the photon scattering rate is determined by the decay of the excited state component of the dressed state. An atom in the state $|\,1, n\,\rangle$ can thus decay either to $|\,1, n-1\,\rangle$ or to $|\,2, n-1\,\rangle$, and the same holds for an atom in $|\,2, n\,\rangle$. The decay rates can be calculated from the transition dipole moments, because the decay rate is proportional to the square of the dipole moment, and the full atomic dipole moment $\mathbf{d} = \langle\, e\,|\,\hat{\mathbf{d}}\,|\,g\,\rangle$ just corresponds to the decay rate Γ of the free atom. In the limit of far detuning $|\Delta| \gg \Omega_\mathrm{R}$, we keep only the lowest orders of Ω_R/Δ in the calculation of the dipole moments

$$\begin{aligned}
\mathbf{d}_{11} &= \langle\,1, n\,|\,\hat{\mathbf{d}}\,|\,1, n-1\,\rangle = \tfrac{\Omega_\mathrm{R}}{2\Delta}\mathbf{d} \\
\mathbf{d}_{12} &= \langle\,1, n\,|\,\hat{\mathbf{d}}\,|\,2, n-1\,\rangle = -\tfrac{\Omega_\mathrm{R}^2}{4\Delta^2}\mathbf{d} \\
\mathbf{d}_{21} &= \langle\,2, n\,|\,\hat{\mathbf{d}}\,|\,1, n-1\,\rangle = \left(1 - \tfrac{\Omega_\mathrm{R}^2}{4\Delta^2}\right)\mathbf{d} \\
\mathbf{d}_{22} &= \langle\,2, n\,|\,\hat{\mathbf{d}}\,|\,2, n-1\,\rangle = -\tfrac{\Omega_\mathrm{R}}{2\Delta}\mathbf{d}
\end{aligned} \tag{1.39}$$

and the decay rates

$$\Gamma_{11} = \Gamma_{22} = \frac{\Omega_\mathrm{R}^2}{4\Delta^2}\Gamma \tag{1.40a}$$

$$\Gamma_{12} = \frac{\Omega_\mathrm{R}^4}{16\Delta^4}\Gamma \tag{1.40b}$$

$$\Gamma_{21} = \Gamma. \tag{1.40c}$$

Due to the large Γ_{21} the atom will almost always stay in state $|\,1, n\,\rangle$, and the scattering rate R_s is dominated by Γ_{11}. Identifying

$$\Omega_\mathrm{R}^2 = \frac{6\pi c^2\Gamma}{\hbar\omega_0^3} I \tag{1.41}$$

we reproduce the potential depth and scattering rate (1.20) of the classical model.

Multi-level atoms

When the atom possesses more than two levels, one could proceed as above, i. e. construct the total Hamiltonian including all possible interactions and diagonalize it. In our case the energy shifts U are very small compared to the detunings Δ. Therefore it is a very good approximation to take the energy shift due to each allowed transition into account separately, because one transition shifts the levels so little that they can be regarded as unshifted for calculating the influence of the next transition. The total shift of a level is then obtained as the sum of the shifts due to all transitions connecting to that level, weighted by the transitions' oscillator strengths. The individual

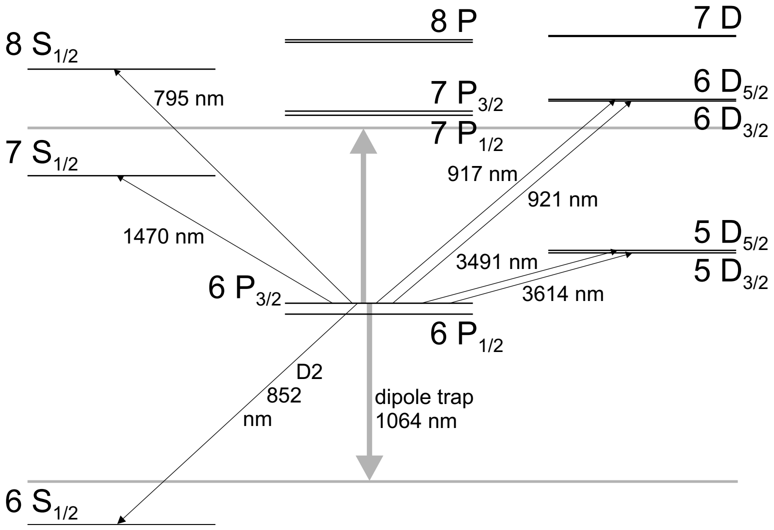

Figure 1.12: Some of the transitions used in calculating the shift of the $6P_{3/2}$ state. With respect to some of the transitions, the dipole trap laser is red detuned, for some others, it is blue detuned.

shifts can be calculated using either the dressed state equations (1.37) or the classical equations (1.19). The main result of the dressed state model is that the excited state is shifted by the same amount as the ground state, but in the opposite direction. This enables us to obtain the shifts of excited states, which cannot be obtained from the classical model.

The shift of the $6P_{3/2}$ state of cesium in a linearly polarized Nd:YAG laser dipole trap ($\lambda = 1064$ nm) has been computed by D. Schrader [51], taking into account transitions to several higher lying states, see fig. 1.12. It turns out that, for the excited state, the light shift strongly depends on the F and m_F quantum numbers; it even changes sign. In contrast, the shift of the $6S_{1/2}$ ground state does not depend on m_F and the dependence on F is only 10^{-4} of the absolute shift.

1.2.3 Experimental Setup

Trap parameters

Our dipole trap consists of two counterpropagating Gaussian laser beams with wavelength λ, waist radius w_0, and the same waist position, power, and polarization. They are overlapped to create a standing wave interference pattern. Neglecting the Guoy phase of the Gaussian beams as well as the curvature of the wavefronts, the intensity distribution can be written as

$$I(z,\rho) = I_{\mathrm{P}} \frac{w_0^2}{w^2(z)} e^{-\frac{2\rho^2}{w^2(z)}} \cos^2(kz) \tag{1.42a}$$

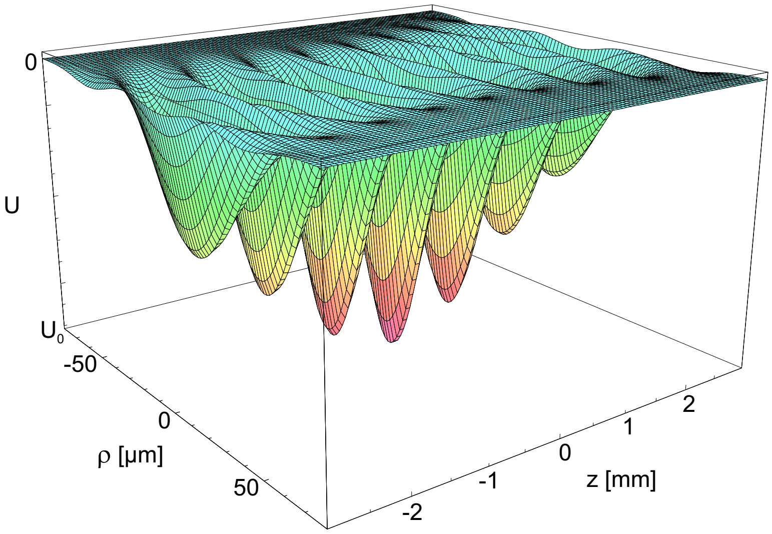

Figure 1.13: Three-dimensional view of the standing wave dipole potential in the (ρ,z)-plane. In z-direction, the wavelength has been stretched by a factor 1500 to show the individual potential wells.

$$w^2(z) = w_0^2\left(1+z^2/z_0^2\right) \tag{1.42b}$$

$$z_0 = \pi w_0^2/\lambda \tag{1.42c}$$

$$I_\mathrm{P} = \frac{4P}{\pi w_0^2}. \tag{1.42d}$$

Here, $w(z)$ is the beam radius with waist w_0 and Rayleigh length z_0. The peak intensity I_P for a total power P is twice that of a single beam of power P due to the constructive interference. In the experiments we use the values

$$\lambda = 1064 \text{ nm} \tag{1.43a}$$

$$w_0 = 30 \text{ μm} \tag{1.43b}$$

$$z_0 = 2.7 \text{ mm} \tag{1.43c}$$

$$P = 4 \text{ W} \tag{1.43d}$$

$$I_\mathrm{P} = 5.6\cdot 10^9 \text{ W/m}^2. \tag{1.43e}$$

unless otherwise noted. Using equations (1.22) we obtain a trap depth U_0 and scattering rate R_s of

$$\begin{aligned} U_0 &= -1.5 \text{ mK}\cdot k_B \\ R_\mathrm{s} &= 9.6 \text{ s}^{-1}. \end{aligned} \tag{1.44}$$

Fig. 1.13 gives an impression of the dipole potential.

The oscillation frequencies of an atom in the center of the trap are given, in harmonic approximation, by

$$\Omega_{\mathrm{z}} = 2\pi\sqrt{\frac{2U_0}{m\lambda^2}} \tag{1.45}$$

$$\Omega_{\mathrm{rad}} = \sqrt{\frac{4U_0}{mw_0^2}} \tag{1.46}$$

in axial and radial directions, respectively. In our case of cesium atoms, $\Omega_{\mathrm{z}}/2\pi = 410$ kHz and $\Omega_{\mathrm{rad}}/2\pi = 3.3$ kHz.

Laser

Our dipole trap laser is a Nd:YAG laser (Quantronix, model 116EF–OCW–10), which is an arc-lamp pumped, high power cw industrial laser. Its resonator contains two mode-filtering apertures and two brewster windows to force operation in the fundamental Gaussian (TEM_{00}) transverse mode with linear polarization. Additionally, an uncoated plane-parallel glass plate serves as an etalon to reduce the number of simultaneously lasing longitudinal modes from > 30 to about 4. This increases the coherence length to > 10 cm and therefore ensures a good interference contrast of the two beams which form the standing wave. In this configuration the maximum output power is 10 watts.

A schematic overview of the dipole trap setup is presented in fig. 1.14. The output beam first passes a thin film polarizer (not shown) to increase the purity of the polarization to $> 10^4 : 1$. A mechanical shutter switches on and off the dipole trap within 10 ms, and a variable attenuator, consisting of a $\lambda/2$ waveplate and a polarizing beam splitter cube (PBS), is used to manually set the power level. An optical isolator (Gsänger Optoelektronik, model FR 800/1200–8, 30 dB) protects the laser from optical feedback.

Acousto-optical modulators

Next, the laser beam is divided by a polarizing beam splitter into two separate beams which will create the standing wave. Each beam passes through an acousto-optical modulator (AOM) of high efficiency (Crystal Technology, model 3110-125). The AOMs are used for fast control of the laser power and for detuning the laser frequency (see section 1.3.3). To maintain a stable beam direction while scanning the frequency, the AOMs are set up in double pass configuration [52] (not shown in fig. 1.14) by retro-reflecting the first order diffracted beam back into the AOM. This setup also allows us to operate the dipole trap with the AOMs switched off simply by retro-reflecting the zeroth diffraction order. An aberration-compensated telescope enlarges the beam diameter, such that it can be focused down to a waist radius of 30 µm by a $f = 300$ mm lens.

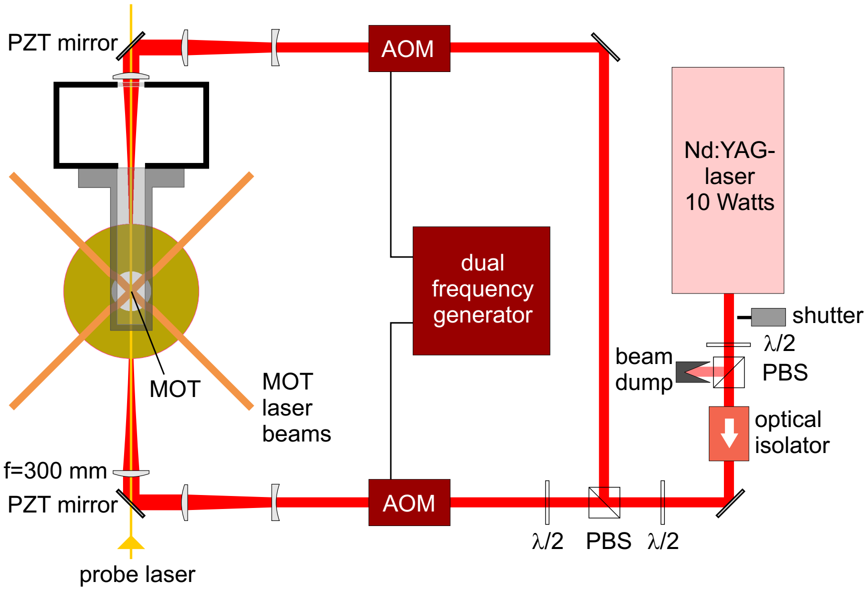

Figure 1.14: Schematic overview of the dipole trap laser setup. PBS: polarizing beam splitter, AOM: acousto-optical modulator, $\lambda/2$: half waveplate for polarization rotation.

Alignment

Each beam of the dipole trap is carefully aligned onto the MOT position. For this purpose we shine the dipole trap laser beam on the MOT and observe the fluorescence of the atoms. When the beam hits the atoms, it induces a light shift of the atomic levels (see sec. 1.2.2) such that the cooling transition is effectively blue detuned, further away from the MOT cooling laser. The fluorescence rate per atom thus decreases typically by more than a factor of 3, which we therefore use as a sensitive alignment criterion. To aid in the alignment, the last two mirrors, which steer the two dipole trap beams into the vacuum chamber, are equipped with piezoelectric actuators (Thorlabs, model KC1-PZ/M).

1.3 Experimental methods

The experiments described later in this thesis rely on the basic experimental techniques of loading and counting atoms in MOT and dipole trap, and transportation of atoms.

1.3.1 Forced loading of atoms

In the beginning of each experimental sequence, atoms are loaded into the MOT from the cesium background vapor. Once the number of atoms is

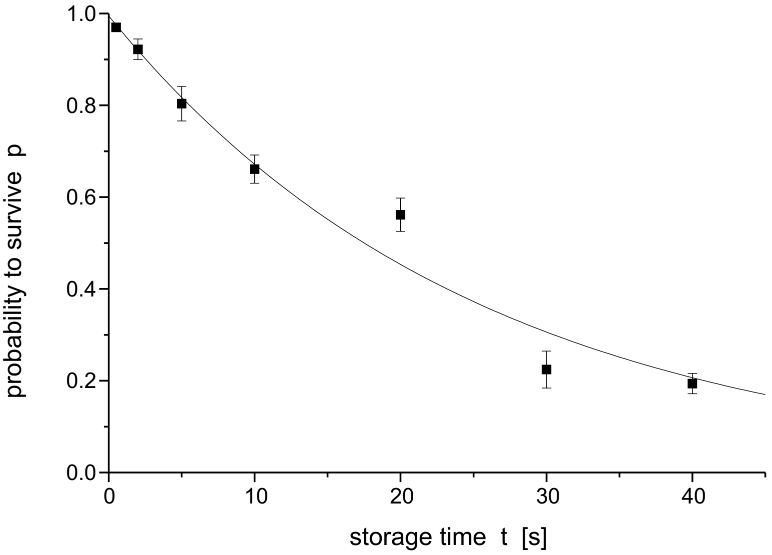

Figure 1.15: Lifetime of atoms in the dipole trap. The fit function is $p(t) = p_0 \exp(-t/\tau)$ with $p_0 = 0.99 \pm 0.04$ and $\tau = 25 \pm 3$ s.

determined from the fluorescence, it should not change due to spontaneous loading events during the rest of the sequence, which requires a rather low cesium vapor pressure. In order to still load a required average number of atoms within a short time, we lower the magnetic field gradient of the MOT from 300 G/cm to about 30 G/cm during the loading time. According to equation (1.6), the low gradient enhances the loading rate by up to four orders of magnitude. This "magnetic umbrella" [5] allows us to load a mean number of 1–50 atoms within 5–500 ms, while the probability to spontaneously load an additional atom during the rest of the experimental sequence is typically 1%.

1.3.2 Transfer efficiency and lifetime

Almost all our experiments rely on counting the number of atoms in the MOT before and after their manipulation in the dipole trap. Thus, a crucial step is the highly efficient transfer of the atoms between the two traps. The most simple experiment is the measurement of the lifetime of the atoms in the dipole trap. After loading a few atoms into the MOT and counting them by means of their fluorescence rate, we switch on the dipole trap and operate MOT and dipole trap simultaneously for about 50 ms. Then we switch off the MOT lasers and leave the atoms in the dipole trap. After a waiting time the remaining atoms are transferred back into the MOT, using again a temporal overlap of the two traps. The MOT, finally, allows us to count the number of atoms that survived. This sequence was repeated 100 times with about two atoms (in average) per repetition to obtain the probability for an atom to survive. Since each atom initially counted in the MOT can either survive or get lost, the experiment is of the Bernoulli type and the statistical error of the probability estimate is calculated accordingly, see sec. 2.2.2.

In fig. 1.15 the probability p to survive a storage time t within the dipole trap is shown together with an exponential fit, $p(t) = p_0 \exp(-t/\tau)$. The time constant τ is the lifetime of the atoms in the dipole trap, while the survival probability p_0 yields the transfer efficiency from the MOT into the dipole trap and back. For $t = 500$ ms we measured a transfer efficiency of $97 \pm 1\%$, and the fit yields $p_0 = 99 \pm 4\%$. In a preceding experiment a similar result was obtained with a running wave dipole trap [26]. This high transfer efficiency means that we can place a known number of atoms into the dipole trap after preparing and counting them in the MOT. Similarly we count the atoms in the dipole trap by loading them back into the MOT.

We attribute the lifetime of 25 s in the dipole trap to collisions with thermal background gas atoms, which can easily remove cold atoms from the dipole trap. Other possible loss mechanisms are heating effects and cold collisions between trapped atoms. Heating mechanisms are described in detail in section 2.4, but they turn out not to limit the lifetime in this case, where the AOMs were turned off. Collisions between trapped atoms are very improbable, because the atoms are distributed over about 50 individual potential wells of the dipole trap. Additionally, the preceding experiment [26] showed equal lifetimes in the dipole trap and in a magnetic quadrupole trap, which points to a universal loss mechanism such as background gas collisions.

1.3.3 Optical conveyor belt

The standing wave geometry was chosen for our dipole trap because it enables us to move trapped atoms along the dipole trap axis in a precise, electronically controlled way. The standing wave interference pattern can be set into motion by slightly mutually detuning the frequencies of the two counterpropagating laser beams. This effect can easily be understood in a moving frame of reference, see fig. 1.16. Because the velocity is proportional to the frequency difference between the two beams, the interference pattern can be uniformly accelerated and decelerated by the application of linear frequency ramps to one of the dipole trap beams. As long as the acceleration is not too high, atoms trapped in individual potential minima (anti-nodes) of the standing wave are carried along in this optical conveyor belt [6, 53].

In the experiment, the AOMs are used to shift the optical frequencies of the two dipole trap beams (fig. 1.14). A custom-built dual digital frequency synthesizer (APE Berlin, model DFD 100) supplies both AOMs with the same frequency (i. e. constant phase difference) as long as the conveyor belt is at rest. For the transport of an atom, one frequency is ramped up and down in a phase-continuous way to accelerate and decelerate the conveyor

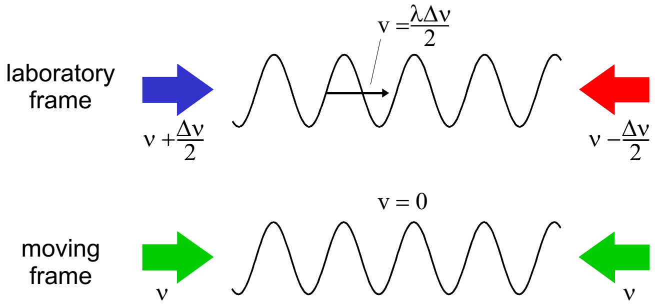

Figure 1.16: Two counterpropagating waves with a small frequency difference $\Delta\nu$ produce a standing wave pattern moving at a velocity $v = \Delta\nu\lambda/2$. This fact can be understood in the co-moving frame of reference, in which the two laser beams are doppler shifted such that their frequencies coincide and the interference pattern is at rest.

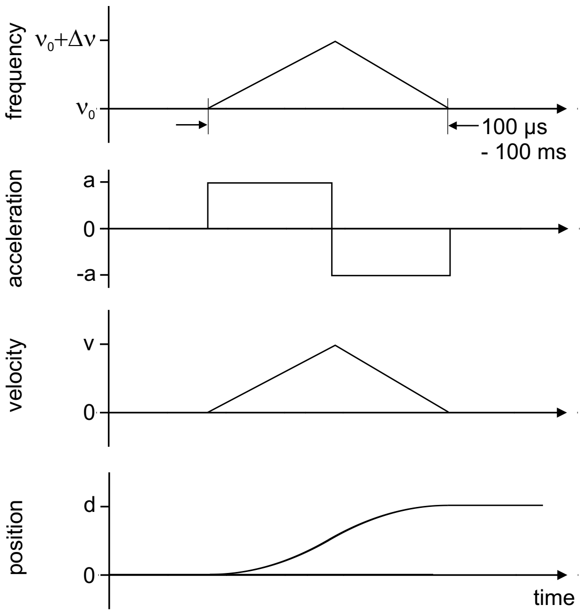

Figure 1.17: The conveyor belt is operated by applying a triangular frequency ramp to one of the dipole trap beams. The atom is accelerated and decelerated uniformly, velocity and position as function of time are shown below.

belt, see fig. 1.17. The full digital control of the frequency ramps allows us to set the total phase difference $\Delta\phi_{\mathrm{opt}}$ between the two counterpropagating laser beams, accumulated during the frequency sweep, with an accuracy of a fraction of 2π. The transportation distance is thus determined with sub-micrometer precision to $d = \Delta\phi_{\mathrm{opt}}\lambda/(4\pi)$.

When the atom has stopped at its new position it can be resonantly illuminated inside the dipole trap with a probe laser and observed by the movable detection assembly of fig. 1.9. This detector previously was translated by the transportation distance along the dipole trap axis. In this way we found that the optical conveyor belt transports single atoms over a macroscopic distance of 1 mm with an efficiency of 92%. With another detection method, transportation efficiencies of 80% over 10 mm were obtained [6].

Typical accelerations of $a = 10^4$ m/s^2 bring the atoms to velocities of 5.5 m/s (optical detunings of 10 MHz) within 0.6 ms. These values are for a transportation distance of 3 mm. A detailed description of the optical conveyor belt and its properties can be found in the thesis of Stefan Kuhr [5] and in [6, 53, 5].

Chapter 2

Temperature measurements in the dipole trap

For the application of neutral atoms in quantum information processing, control over all degrees of freedom is required. This is obvious for the internal state, in which the quantum information is encoded. But also the external degrees, such as position, velocity and temperature, play an important role. A high temperature of the atoms in the dipole trap, for example, leads to an inhomogeneous broadening of their transition frequencies due the light shift. This effect has been shown to limit the coherence time in our experiment [7]. As another example, the temperature-dependent localization of an atom determines its coupling to the mode of an optical resonator. A prerequisite for the control of the temperature is its measurement. For this purpose, methods compatible with the small number of atoms in our trap have to be used.

The temperature is determined by cooling and heating mechanisms. Therefore, the implementation and evaluation of cooling methods is an important goal of our experiment in the near future. Uncontrolled heating can prevent successful cooling and even limit the lifetime of atoms in the trap. Hence, the classification of heating effects of fundamental and technical origin is of prime interest.

2.1 Methods

Since the temperature of a sample of trapped atoms cannot be measured by directly contacting it, one usually measures the position, velocity or energy distribution of the cold trapped atoms, from which their temperature is then deduced.

2.1.1 Velocity distribution (Time-of-flight)

The time-of-flight method measures the velocity distribution to determine the temperature of trapped atoms. For this purpose the trapping potential is switched off quickly, such that each atom continues to travel freely with its instantaneous velocity. After an expansion time, the atomic cloud is imaged onto a CCD camera by illuminating it for a short duration. If the atoms do not interact during the expansion, and the size of the cloud after the expansion is large compared to its initial size in the trap, the spatial distribution of the expanded cloud directly maps out the initial velocity distribution within the trap.

In an harmonic trapping potential, the virial theorem states that the average potential energy is equal to the average kinetic energy. In this way, the mean total energy $\langle E \rangle$ can be calculated from the distribution of the kinetic energy which in turn follows from the measured velocity distribution. In the case of thermal equilibrium, the temperature T follows from

$$\langle E \rangle = 3k_{\mathrm{B}}T. \tag{2.1}$$

An advantage of the time-of-flight method is that it yields the complete energy distribution in a single shot. Additionally, the size of the expanded cloud is easily adapted to the density or resolution requirements of the imaging system by varying the expansion time. A disadvantage is that it requires a large number of atoms to work properly, since a single atom within a large detection area together with a short exposure time yields a small amount of fluorescence only. While adding up a large number of images would help in principle, background noise adds up as well, which further increases the required number of images.

2.1.2 Spatial imaging

Direct imaging of the trap yields the spatial distribution of the atoms in the trapping potential. If the potential is known, the distribution of energies in the sample can be obtained. This method is applied to our dipole trap in section 2.5.

A prerequisite for spatial imaging is that the atoms can be illuminated in the trap without changing the temperature. This is certainly the case in a MOT, where equilibrium temperatures have been measured this way [54, 55]. In our dipole trap, we have to illuminate the atoms with near-resonant light for observation. Heating due to photon scattering must be counteracted by laser cooling (sec. 2.5.2).

Temperature measurement by spatial imaging is ideally suited for small numbers of atoms, since high atomic densities could lead to heating by light-induced inelastic collisions or to optically thick samples. Additionally, even for a single atom in the trap, its equilibrium temperature can be obtained from a single image by integrating the fluorescence long enough to average over many heating and cooling cycles. A disadvantage is that for small, steep traps or low temperatures, this method requires higher resolution imaging as compared to the time-of-flight method.

2.1.3 Release-recapture

In the release-recapture method [16, 56], the trapping potential is switched off non-adiabatically to release the atoms into free expansion. After a short waiting time the potential is switched back on, and those atoms which still roam the trap volume are recaptured. During the expansion, hot atoms will on average leave the trapping region with a higher velocity than cold atoms. The time it takes for a substantial fraction of the atoms to leave the trap volume can therefore be used to estimate their temperature in the trap.

A more precise determination of the temperature requires good knowledge of the capture volume of the trap and numeric modelling of the expansion process using an estimated energy distribution. An advantage of the release-recapture method is that it does not require any imaging of atomic clouds. It can therefore be used on very small atomic ensembles, which can be detected only either inside the trapping potential or by transferring the atoms into a different type of trap, e. g. a MOT. In this way the temperature of single atoms in a dipole trap has been measured in P. Grangier's group [57].

2.1.4 Adiabatic lowering

I have devised a technique to obtain the complete energy distribution of an atomic ensemble while using only a single atom at a time. The basic idea is to slowly reduce the depth of the trapping potential from U_0 to a nonzero value U_{low} such that a fraction of the atoms escapes. The surviving fraction is then detected.

When the potential is changed adiabatically, exactly those atoms survive which initially had a thermal energy E_0 less than a certain threshold energy E. Furthermore, this threshold depends only on the depth U_{low} to which the potential was reduced. Thus, by properly choosing U_{low}, we vary the energy threshold E and record the fraction of atoms below that energy. This measurement yields the cumulative energy distribution of the atoms, from which the temperature can be extracted.

Since this method relies on merely detecting a loss of atoms, it is rather simple to implement in our experiment. Another advantage is that we do not have to assume an energy distribution in order to extract the temperature, but we get the entire distribution from the measurement. For these reasons, this method was chosen to measure the temperature of the atoms in our dipole trap.

2.2 Theory and simulations of adiabatic processes

To understand why and how the method of adiabatic lowering works it is illustrated with a one-dimensional model. Here, the quantities of interest can be calculated easily, and an approximate but clear description of the experiment is obtained. A more realistic model of our experiment using the three-dimensional dipole potential and including deviations from strict adiabaticity is analyzed by numeric simulation of atomic trajectories in the trap. In both models, the motion in our trap is treated classically, since the mean oscillatory quantum numbers of our atoms are $n \approx 5$ axially and $n \approx 600$ radially at a temperature of 7% of the trap depth (see sec. 2.3.2).

2.2.1 Adiabatic manipulation of a one-dimensional potential

Action integral

Consider a classical particle oscillating in a conservative one-dimensional potential $V(x)$. When the potential is changed while the particle is moving, the energy of the particle is not conserved any more. There is, however, a result of classical mechanics stating that in the limit of infinitesimally slow (adiabatic) changes, the action integral over one oscillation period,

$$S = \oint p \, dx, \tag{2.2}$$

is conserved [58].

As an illustration, a particle oscillating in an harmonic potential with frequency ν and energy E has an action of $S = E/\nu$. When the spring constant and thus ν is changed adiabatically, E/ν remains constant. This result is familiar from quantum mechanics, where $E/\nu = nh$ and the quantum number n does not change when the wavefunction can follow the change of the potential adiabatically.

Our method of temperature measurement is modeled as an atom oscillating with energy E_0 in the (anharmonic) dipole potential of finite depth U_0,

$$V(x, U_0) = U_0 \tilde{V}(x), \tag{2.3}$$

where $\tilde{V}(x)$ is a normalized shape function ranging from 0 to 1. If the potential is symmetric, $V(x, U) = V(-x, U)$, the action can be written as

$$S(E, U) = 4 \int_0^{x_{\max}} \sqrt{2m[E - V(x, U)]} \, dx, \tag{2.4}$$

where $x_{\max}$ is the turning point of the oscillatory motion given by $V(x_{\max}, U) = E$. When the potential depth U is adiabatically reduced, the energy E of the atom decreases due to “adiabatic cooling”, but less than proportionally to U, see fig. 2.1. Thus, at some depth U_{esc}, its energy E equals U_{esc} and the atom escapes.

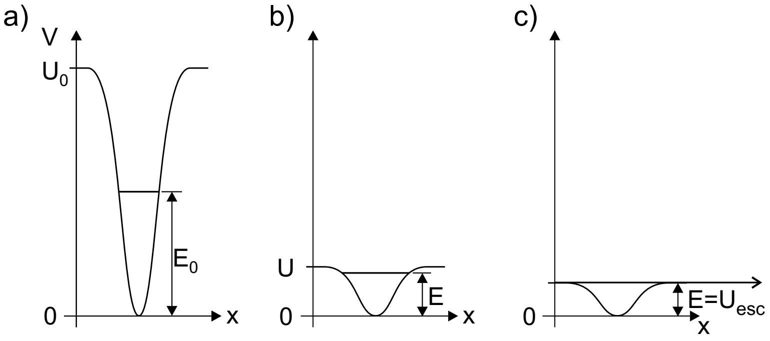

Figure 2.1: An atom with initial energy E_0 in a potential of depth U_0 (a) is cooled adiabatically to energy E when the potential depth is reduced to U (b). Since E decreases more slowly than U, the atom escapes at some point (c), at which the energy of the atom E_{esc} equals the potential depth U_{esc}.

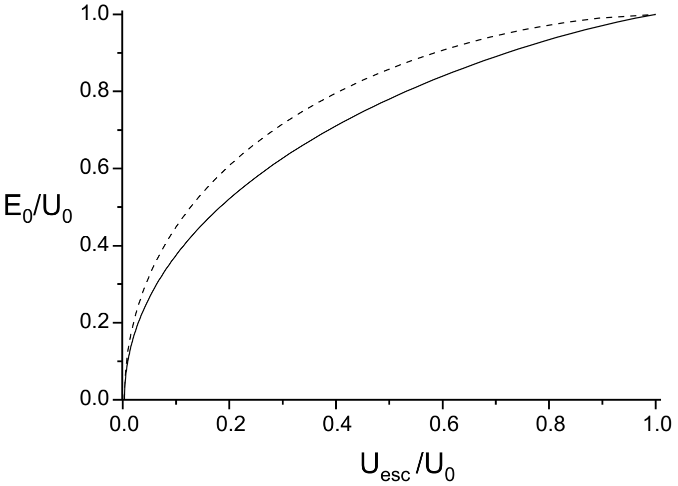

Figure 2.2: Relation between the escape depth U_{esc} and the initial energy E_0 of an atom in a one-dimensional potential. Solid line: $V(x,U) = U\big(1-\cos^2(kx)\big)$ (axial potential of our dipole trap); dashed line: $V(x,U) = U\big(1-\exp(-2x^2/w_0^2)\big)$ (radial potential of the dipole trap).

Since the action S is conserved, we numerically solve

$$S(E_0, U_0) = S(U_{\mathrm{esc}}, U_{\mathrm{esc}}) \tag{2.5}$$

to obtain the relation between the initial energy E_0 and the escape depth U_{esc} shown in fig. 2.2. As an example, a typical atom with $E_0 = 0.1\,U_0$ escapes (axially) when the trap depth is lowered to 0.9%.

Adiabaticity criteria

In reality the changes of the potential are never infinitesimally slow. A practicable criterion for adiabaticity is that the potential should not change significantly during one oscillation period [58]. Since in our case changing the potential depth means changing the oscillation frequency ν, the relative change $\Delta\nu/\nu = (\dot{\nu}T)/\nu$ within one oscillation period $T = 1/\nu$ should be small, i. e.

$$\left|\frac{\dot{\nu}}{\nu^2}\right| \ll 1. \tag{2.6}$$

An optimal way to to lower the potential depth U within a given time should avoid large values of $|\dot{\nu}/\nu^2|$ and therefore keep $\dot{\nu}/\nu^2 = const.$. Solving this differential equation for $\nu(t)$ together with the harmonic approximation $\nu \sim \sqrt{U}$ yields the result $U(t) \sim 1/t^2$.

The energy of an atom after a *non-adiabatic* reduction of the potential depth depends on its phase of oscillation, and *not* only on its initial energy E_0. This becomes obvious for an instantaneous change of the depth, where the potential energy of an atom changes proportionally to the trap depth, whereas its kinetic energy remains unchanged.

Because the anharmonicity of our potential makes the oscillation frequency ν approach zero as E approaches U, the adiabaticity condition is always violated right before the atom leaves the trap. This energy region, however, can be made small by decreasing the potential depth more slowly than what would be required for an harmonic potential.

For a quantitative analysis, trajectories of atoms in a one-dimensional Gaussian potential were simulated by numerically integrating the classical equations of motion. As an example, the potential depth is ramped down from U_0 to $U_{\mathrm{low}} = 0.01\,U_0$. According to the relation of fig. 2.2, all atoms with an initial energy E_0 of less than $0.155\,U_0$ should remain trapped, whereas all more energetic atoms should be lost. In the simulation, there is a span ΔE_0 of energies E_0 over which the loss rate rises from 10% to 90%. This span determines the energy selectivity and increases with decreasing ramping duration, indicating a loss of adiabaticity.

The simulation revealed that a smooth transition from the constant $U(t) = U_0$ to the decreasing part $U(t) \sim 1/t^2$ considerably improves the

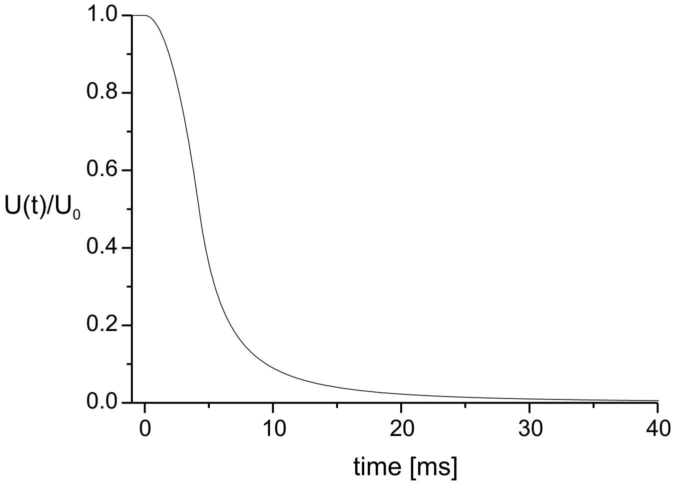

Figure 2.3: Optimized function $U(t)$ of eq. (2.7) used to adiabatically ramp down the potential depth.

adiabaticity, which is also expected theoretically [58]. Therefore, the potential depth is ramped down according to

$$U(t) = \begin{cases} U_0 & \text{for} \quad t \le 0 \\ U_0\left(1 - \dfrac{t^2}{4T_\mathrm{c}^2}\right) & \text{for} \quad 0 < t \le T_\mathrm{c}\sqrt{2} \\ U_0\dfrac{T_\mathrm{c}^2}{t^2} & \text{for} \quad t > T_\mathrm{c}\sqrt{2} \end{cases}, \tag{2.7}$$

see fig. 2.3. The characteristic time scale T_c determines the ramp duration and the adiabaticity. A value of $T_\mathrm{c} = 9.3/\nu$ keeps $|\dot{\nu}/\nu^2| < 0.11$ and results in an energy selectivity ΔE_0 of about 2–5% of U_0. With the radial oscillation frequency $\nu_\mathrm{rad} = 3.1$ kHz, T_c becomes 3 ms, and lowering the trap depth to 1% takes 30 ms.

2.2.2 Simulation of trajectories in a realistic 3-D potential

Motivation

The one-dimensional analysis of the adiabatic lowering has several shortcomings. In our three-dimensional dipole potential, the axial motion of an atom does not exchange energy with the radial motion, because their oscillation frequencies differ by two orders of magnitude. The two radial degrees of freedom, however, are mutually coupled by the anharmonicity of the radial potential combined with an inevitable slight ellipticity of the dipole trap. Additionally, the effect of gravity offsets the zero point of the potential and thus breaks the remaining symmetries. Numerical simulations of the motion in the radial plane indicate that the radial oscillatory motion can therefore completely change its orientation and ellipticity over several oscillation periods on a rosetta-like trajectory. Since this precession period strongly depends on the oscillation amplitude of the atom and the depth and the ellipticity of the trap, it remains unknown in praxis. Therefore, the reduction of the trap depth can well be adiabatic with respect to all oscillation frequencies, but still be non-adiabatic with respect to the precession period of the oscillation.

At trap depths below a few percent, an atom escapes the potential most easily along the axis of gravity. The escape depth therefore depends on whether the atom oscillates horizontally or vertically in the radial plane. Together with the non-adiabaticity with respect to the precession period, a reduction of the energy selectivity can therefore not be excluded.

As a second point, the escape depths of fig. 2.2 indicate that the atoms leave the trap in axial rather than in radial direction. An atom which oscillates in axial direction with near maximum amplitude spends most of its time near the node of the standing wave, due to the anharmonicity of the potential. There, however, the radial force is very weak since the three-dimensional potential is a *product* of a Gaussian and a $\cos^2$ function. Therefore, the radial potential depth averaged over the fast axial motion goes to zero as the atom tries to escape axially. Similarly, a large radial excursion weakens the axial confinement. Is is therefore not evident whether the three-dimensional escape depths would follow the axial or the radial curve of fig. 2.2, or a different relationship.

I did a full simulation of the atomic trajectories in our three-dimensional dipole potential to answer these questions and to be able to quantitatively analyze our experimental results. The simulation includes the effect of gravity, the finite duration of the ramp and the waiting time used in the experiment (sec. 2.3).

Overview

The simulation places an atom with a certain initial energy E_0, but otherwise randomly distributed initial position and velocity, into the dipole trap potential

$$V(x, y, z, t) = U(t) \cos^2(kz)\, e^{-2(x^2+y^2)/w_0^2} + mgy. \tag{2.8}$$

The potential depth $U(t)$ is then ramped down according to eq. (2.7) to a value U_{low}, while the motion of the atom in the potential is calculated. The potential depth is held at U_{low} for 15 ms to make sure that escaping atoms leave the trap region. The atom is counted as lost if it has departed more than 100 µm from the origin, which approximates the capture radius of our MOT.

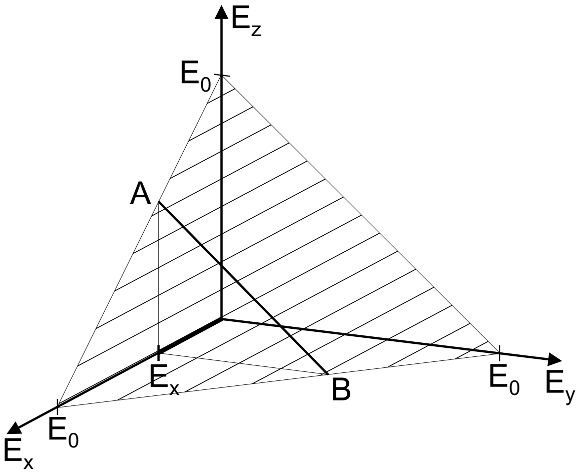

Figure 2.4: The system homogeneously populates the hatched triangular surface $E_x + E_y + E_z = E_0$. Its projection onto the E_x-axis yields the probability distribution of E_x. After fixing E_x, the system homogeneously populates the line $\overline{AB}$.

This calculation is repeated many times to obtain the probability $p(E_0, U_{\text{low}})$ of an atom remaining trapped for a specific E_0 and U_{low}. When U_{low} is decreased, the survival probability p changes from unity to zero. The escape depth is defined by $p(E_0, U_{\text{esc}}) = 0.5$, and the span ΔU_{esc} it takes p to decrease from near unity to near zero indicates the energy resolution.

Choosing the starting coordinates

The starting position and velocity of the atom should be randomly distributed over the phase space of the system, however with a fixed total energy E_0. For this purpose, the energy E_0 is divided onto the three degrees of freedom $\{x, y, z\}$ with

$$\begin{aligned} E_x + E_y + E_z &= E_0 \\ 0 \leq E_i &\leq E_0 \\ i &= x, y, z \quad . \end{aligned} \tag{2.9}$$

We assume that initially the atoms are thermally distributed with a temperature T. Then the probability of a certain energy configuration only depends on the total energy E_0, and not on the individual energies E_i. The triangular surface in the space $\{E_x, E_y, E_z\}$ defined by eq. (2.9) is thus assumed to be homogeneously populated, see fig. 2.4. My algorithm therefore first chooses a random E_x with a probability distribution which decreases linearly from $E_x = 0$ to $E_x = E_0$,

$$p(E_x) = \frac{2}{E_0^2}(E_0 - E_x). \tag{2.10}$$

Once E_x is fixed, the remaining energies $\{E_y, E_z\}$ are homogeneously distributed on the line $E_y + E_z = E_0 - E_x$. Thus E_y is chosen randomly from the interval $[0, E_0 - E_x]$, and $E_z = E_0 - E_x - E_y$.

The position and velocity are chosen such that the energy in each degree of freedom i is E_i, but the phase of oscillation is homogeneously distributed in the interval $[0, 2\pi]$. For this purpose, the algorithm starts with an atom at the bottom of the one-dimensional potential $V(x_i)$ with a velocity corresponding to a kinetic energy of E_i. Then the oscillation period in this anharmonic potential is determined for the energy E_i. The one-dimensional equations of motion are then solved numerically for a random fraction of this oscillation period to obtain the position and velocity at a random phase of the oscillation.

The three independently determined positions $\{x, y, z\}$, however, cannot directly be combined to a starting coordinate for the three-dimensional simulation, because of the anharmonicity of the potential, $V(x, 0, 0) + V(0, y, 0) + V(0, 0, z) \neq V(x, y, z)$. The distance of the atom from the origin is therefore slightly adjusted until the total energy equals E_0.

Calculation of the trajectories

The three-dimensional equations of motion in the time-varying potential (2.8) are solved numerically by a fourth-order Runge-Kutta algorithm. After careful evaluation of the numerical accuracy a fixed step time of 3 ns was used. For speed reasons I used an optimized version of the C-implementation from Numerical Recipes [59]. The C-program is interfaced to a Mathematica program which chooses the starting coordinates and does the statistical bookkeeping.

Statistical evaluation

For each set of parameters E_0 and U_{low}, the probability for an atom to survive, $p(E_0, U_{\text{low}})$, has to be determined with some reasonably small statistical error using the least possible number N of trajectories. When k atoms out of N survive, the estimate for the true survival probability p is k/N according to Bernoulli statistics.

The 1σ confidence interval $[p_-, p_+]$ around p denotes the range within which k/N falls with 68% probability. This range is a measure for the expected discrepancy between the probability p and its estimate k/N due to the limited size of the sample N. The confidence interval can be calculated from [60]

$$\sum_{l=0}^{k} P(p_+, N, l) = (1 - 0.68)/2 \qquad (2.11a)$$

$$\sum_{l=k}^{N} P(p_-, N, l) \quad = \quad (1 - 0.68)/2, \tag{2.11b}$$

with the binomial probability

$$P(p, N, k) = \binom{N}{k} p^k \, (1 - p)^{N-k}. \tag{2.12}$$

After each trajectory simulation, equation (2.11) is evaluated and another trajectory is simulated until the width of the confidence interval $p_+ - p_-$ is less than 0.1. While about $N = 120$ trajectories are needed for $p \approx 0.5$, a much lower number of simulations (down to $N = 18$) is required for the same statistical accuracy when p is near unity or near zero.

For each E_0 the corresponding U_{esc} is found by looking at the survival probability $p(E_0, U_{\mathrm{low}})$ for different values of U_{low}. The U_{low} are chosen by a recursive interval halving algorithm such that neighboring values of the survival probability p differ by less than 0.2. This ensures that the critical transition from $p(E_0, U_{\mathrm{low}}) \approx 1$ to $p(E_0, U_{\mathrm{low}}) \approx 0$ is found quickly and is sampled just sufficiently dense.

I finally fit an error-function $\mathrm{erf}((U_{\mathrm{low}} - U_{\mathrm{esc}})/\Delta U_{\mathrm{esc}})$ to the survival probability. From this fit the escape depth U_{esc} as well as the escape range ΔU_{esc} are obtained.

Results

For different values of the initial atomic energy E_0 the escape depth U_{esc} is shown in fig. 2.5. The three-dimensional trajectory simulation mostly follows the one-dimensional predictions of sec. 2.2.1. The deviation at low energies is probably due to the influence of gravity. In order to evaluate the experimental results in sec. 2.3.2, an analytic function was fitted to the data points. The squareroot-like functional form is suggested by the one-dimensional model.

2.3 Experiment

2.3.1 Measurement procedure

In the beginning of the experimental sequence, about five atoms are loaded into the MOT by means of the forced loading technique (sec. 1.3.1). This number still ensures that the probability of collisions remains very small, because these atoms are distributed over about 50 separate potential wells of the dipole trap. On the other hand, the measurement time is reduced by a factor of five compared to the use of a single atom at a time.

The atoms are then transferred into the dipole trap and the quadrupole magnetic field is switched off to prevent magnetic trapping. The dipole trap

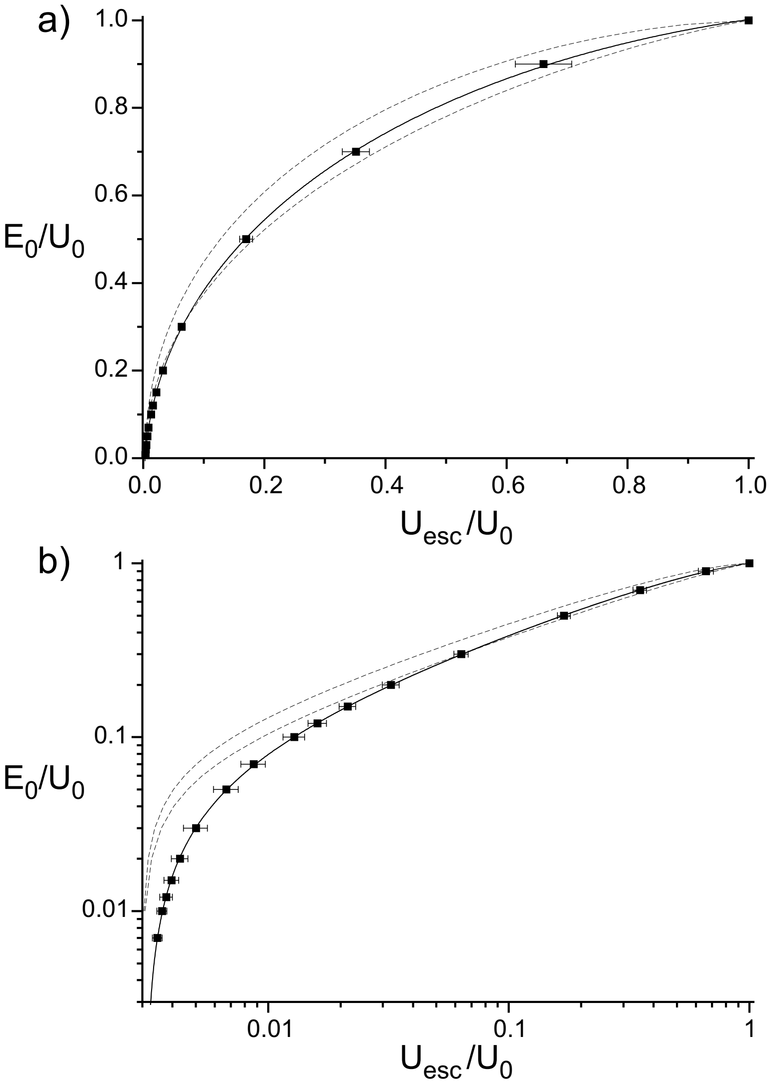

Figure 2.5: Initial atomic energy versus escape depth for the adiabatic lowering in (a) linear scale, (b) logarithmic scale. The data points are the results of the three-dimensional trajectory simulation, the bars indicate the escape range. The solid curve is a fit to the data points with the function $y = b \cdot (\sqrt{x - x_c} - a_0 - a_1 x - a_2 x^2 - a_3 x^3)$. The dotted lines are the one-dimensional predictions of fig. 2.2.

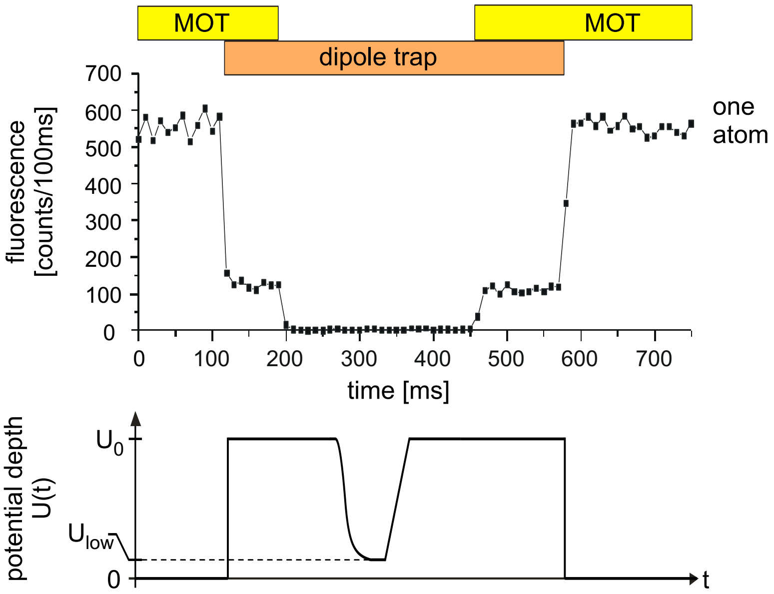

Figure 2.6: Experimental sequence used for the temperature measurement. An atom is transferred from the MOT into the dipole trap, which is then adiabatically lowered. After the dipole trap is ramped up, any atom that remained trapped is transferred back to the MOT. Initial and final number of atoms are extracted from their fluorescence rate.

depth is adiabatically lowered down to U_{low} according to eq. (2.7). The lowering takes between 10 ms and 51 ms for values of U_{low} between $0.082\,U_0$ and $0.0036\,U_0$, respectively. The trap depth is kept low for 15 ms to allow escaping atoms to leave the capture region of the MOT, before the dipole trap is ramped up again and remaining atoms are transferred back to the MOT, see fig. 2.6. The upward ramp does not have to follow the adiabatic form of eq. (2.7), since no atoms are lost on *increasing* the trap depth. For each value of U_{low} the experimental sequence was repeated 100 times to keep the statistical error below 3%.

The change of the dipole trap depth was realized by variation of the RF power of the AOM drivers via an analog control voltage. Due to the PIN-diode RF attenuator inside the AOM driver in combination with the double-pass setup, the relation between the power of the dipole trap laser and the control voltage is highly nonlinear. We measured this transfer function by linearly sweeping the control voltage and monitoring the laser powers by calibrated photodiodes. After digitization with a storage oscilloscope, the data was fitted with a suitable function, the inverse of which was applied to $U(t)$ to precompensate the nonlinearity.

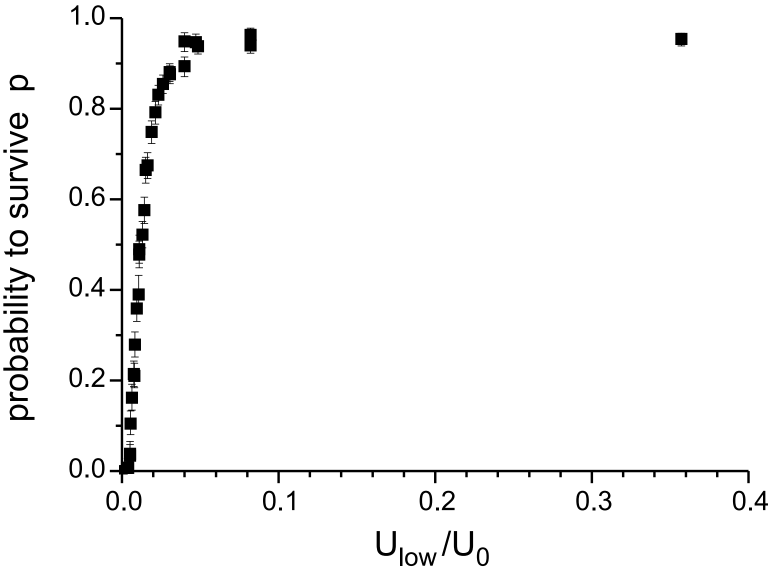

Figure 2.7: Measured survival probability p versus reduced trap depth U_{low}.

2.3.2 Results

The measured survival probability versus U_{low} is shown in fig. 2.7. Due to the adiabatic cooling, the trap depth can be reduced down to a few percent before a significant number of atoms is lost.

The experimental trap depths U_{low} are then converted into initial atomic energies E_0 using the fit function from fig. 2.5. The result, shown in fig. 2.8, is the cumulative energy distribution, i. e. the fraction of atoms with an energy below E_0. In order to extract a temperature we assume a Boltzmann-distribution of the atomic energy

$$p(E) \sim g(E) e^{-\frac{E}{k_{\mathrm{B}}T}}. \tag{2.13}$$

In a three-dimensional harmonic trap, the density of states $g(E)$ is proportional to E^2 [61] and thus

$$p(E) = \frac{1}{2(k_{\mathrm{B}}T)^3} E^2 e^{-\frac{E}{k_{\mathrm{B}}T}}. \tag{2.14}$$

By integration we obtain the cumulative energy distribution

$$P(E) = 1 - \left(1 + \frac{E}{k_{\mathrm{B}}T} + \frac{E^2}{2(k_{\mathrm{B}}T)^2}\right) e^{-\frac{E}{k_{\mathrm{B}}T}}. \tag{2.15}$$

A fit to the measured data with the temperature and the maximum survival probability P_{tot} as free parameters yields $k_{\mathrm{B}}T = (0.034 \pm 0.001)\, U_0$

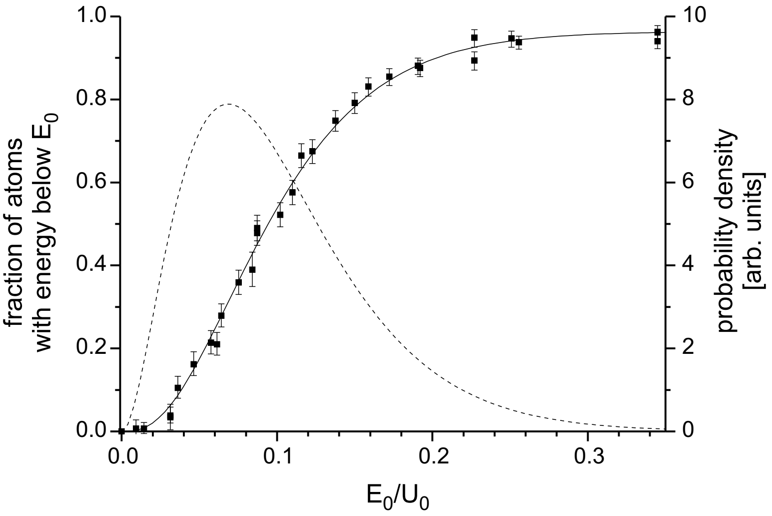

Figure 2.8: Cumulative energy distribution of the atoms in the dipole trap. Solid line: fit of a cumulative three-dimensional Boltzmann distribution (eq. (2.15)) with $k_\mathrm{B}T = 0.034\,U_0$. Dashed line: corresponding (non-cumulative) energy distribution.

and $P_\mathrm{tot} = 96 \pm 1\%$, see fig. 2.8. Using the theoretical $U_0 = 1.5$ mK, the temperature of the atoms is $T = 51$ µK, less than the Doppler temperature of 125 µK. When the trap depth of $U_0 \approx 1.0$ mK determined from the measured axial oscillation frequency (section 2.4.5) is used, a correspondingly lower temperature of $T = 34$ µK is obtained.

These temperatures of the atoms in the dipole trap are similar to the temperatures in our high gradient MOT. Values down to 80 µK have been obtained in [55], in a somewhat lower gradient of 90 G/cm. The high magnetic field gradient and the high cooling laser intensity of $I/I_0 \approx 40$ seem to impede most of the sub-doppler cooling in the MOT. However, we can conclude from the measured temperatures that the cooling action of the MOT continues even with the dipole trap laser superimposed.

2.4 Heating mechanisms in the dipole trap

In the absence of background gas collisions, the lifetime of atoms in the dipole trap is ultimately limited by heating. Besides fundamental heating mechanisms, which turn out to play no role in our experiment, we observe several technical sources of heating. The characterization of the most important heating mechanisms will prove very useful to evaluate techniques for further cooling of the atoms in the dipole trap.

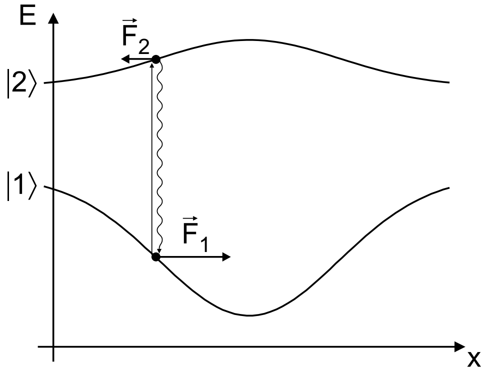

Figure 2.9: Model of the heating by dipole force fluctuations. When the atom is excited from state $|\,1\,\rangle$ to $|\,2\,\rangle$, the dipole force changes from F_1 to F_2.

2.4.1 Recoil heating

A fundamental source of heating in dipole traps is spontaneous scattering of dipole trap laser photons. Each photon imparts on average the recoil energy

$$E_\mathrm{r} = \frac{(\hbar k)^2}{2m} \tag{2.16}$$

to the atom on absorption and on spontaneous emission (here, k denotes the wavenumber of the dipole trap laser). A spontaneous scattering rate R_s therefore increases the average energy of an atom in the dipole trap by [45]

$$\langle \dot{E} \rangle = 2 R_\mathrm{s} E_\mathrm{r}. \tag{2.17}$$

This result remains valid whether the oscillatory motion of the atom is treated classically or quantum-mechanically, and whether the spacing of the motional quantum states is small or large compared to the recoil energy [18].

With our scattering rate of 10 s^{-1} (1.44), the heating rate is only about 0.6 µK/s, which is negligible in our experiment.

2.4.2 Dipole force fluctuations

The dipole potential for a two-level atom has opposite sign for the two dressed states, see sec. 1.2.2. When the atom is excited, it experiences a repellant instead of an attractive potential during the lifetime of the excited state. Averaged over many excitations the stochastically fluctuating dipole force leads to a heating of the atomic motion.

Model

While the heating rate can be calculated via momentum diffusion coefficients [49], we will estimate the effect based on a simple physical model [62].

When an atom in dressed state $|\,1\,\rangle$ of fig. 2.9 is excited to state $|\,2\,\rangle$, the dipole force changes by an amount $\Delta F = F_2(x) - F_1(x)$ for the lifetime $\tau = 1/\Gamma$ of the excited state $|\,2\,\rangle$. This force can be interpreted as a momentary momentum transfer $\Delta p = \Delta F \tau$ as long as the atom does not move significantly during the time τ, i. e. τ is small compared to the oscillation period T_{osc} of the atom in the potential. In our case, this approximation is clearly fulfilled with $\tau = 30$ ns and $T_{\text{osc}} > 2$ µs.

These momentum kicks drive a random walk in momentum space, in analogy to recoil heating. Hence the energies

$$E_{\text{kick}} = \frac{(\Delta p)^2}{2m} \tag{2.18}$$

on average add up, and the heating rate becomes

$$\langle \dot{E} \rangle = R_{\text{exc}} E_{\text{kick}}. \tag{2.19}$$

Intrinsic excitation rate

The excitation rate R_{exc} is not equal to the scattering rate R_{s} of the dipole trap laser, because the latter is dominated by the decay Γ_{11} from the state $|\,1,n\,\rangle$ to $|\,1,n-1\,\rangle$, which does not change the dipole potential (fig. 1.11). Only the rate Γ_{12} describes "excitations" which change the dipole potential and thus contribute to R_{exc}. From equations (1.40) and (1.41) we have

$$\begin{aligned} R_{\text{exc}} &= \Gamma_{12} && \text{(2.20a)} \\ &= \frac{\Omega_{\text{R}}^4}{16\Delta^4}\Gamma && \text{(2.20b)} \\ &= \frac{9\pi^2 c^4 \Gamma^3 I^2}{4\hbar^2 \omega_0^6 \Delta^4} && \text{(2.20c)} \\ &= \frac{R_{\text{s}}^2}{\Gamma} && \text{(2.20d)} \\ &\approx 5 \cdot 10^{-6}\ \text{s}^{-1}, && \text{(2.20e)} \end{aligned}$$

which is completely negligible, since the corresponding heating rate is less than 10^{-8} mK/s.

External excitation

Heating by dipole force fluctuations can be severe when the atom is excited by near-resonant light, for example during optical pumping, (sub-)Doppler cooling or fluorescence detection in the dipole trap. In these cases, the excitation leads from dressed state $|\,1,n-1\,\rangle$ to $|\,2,n\,\rangle$ and thus the relevant state-changing excitation rate R_{exc} is equal to the scattering rate of the near-resonant radiation.

For a quantitative estimation of the heating rate averaged over an oscillation period of the atom, let us assume that the atom with an energy $E = U_0/2$ oscillates in the trap. The turning points $\pm x_{\mathrm{max}}$ then coincide with the steepest slope of the dipole potential, exactly for a $\cos^2$ and approximately for a Gaussian potential shape. Additionally, the part of the potential over which the oscillation extends can be well approximated as harmonic. The amplitude of the dipole force fluctuations ΔF then linearly depends on x as

$$\Delta F(x) = \frac{x}{x_{\mathrm{max}}} \Delta F_{\mathrm{max}}. \tag{2.21}$$

Since the energy E_{kick} depends quadratically on the force ΔF, we calculate the mean square force, averaged over one cycle of oscillation

$$\langle (\Delta F)^2 \rangle = \frac{(\Delta F_{\mathrm{max}})^2}{2}. \tag{2.22}$$

The time t the atom spends in the excited state also enters quadratically in E_{kick}. Therefore, the average squared time $\langle t^2 \rangle$ is calculated from the exponential distribution of the times t, $P(t) = \exp(-t/\tau)/\tau$

$$\begin{aligned} \langle t^2 \rangle &= \int_0^\infty t^2 P(t)\,\mathrm{d}t && \text{(2.23a)} \\ &= 2\tau^2. && \text{(2.23b)} \end{aligned}$$

The average energy then becomes

$$\langle E_{\mathrm{kick}} \rangle = \frac{(\Delta F_{\mathrm{max}})^2 \tau^2}{2m}. \tag{2.24}$$

When the typical energy E of the atom is much less than half the trap depth, the maximum dipole force which the atom experiences at its turning points reduces to $\Delta F_{\mathrm{max}} \sqrt{2E/U_0}$. The heating rate thus finally becomes

$$\langle \dot{E} \rangle = R_{\mathrm{exc}} \frac{E\,(\Delta F_{\mathrm{max}})^2 \tau^2}{m U_0}. \tag{2.25}$$

To further interpret eq. (2.25), we compare it to the unavoidable recoil heating (2.17),

$$\frac{\langle \dot{E} \rangle_{\mathrm{fluctuation}}}{\langle \dot{E} \rangle_{\mathrm{recoil}}} = \frac{E}{U} \left(\frac{\Delta F_{\mathrm{max}}}{F_{\mathrm{res}}} \right)^2, \tag{2.26}$$

where

$$F_{\mathrm{res}} = \frac{\hbar k}{2\tau} \tag{2.27}$$

is the maximum resonant light pressure force that a strongly saturating resonant laser beam can exert on the atom. Heating by dipole force fluctuations can thus only contribute significantly if the maximum dipole force exceeds the maximum resonant light force.

In our trap we have

$$\begin{aligned}
\text{axial: } \Delta F_{\max} &= kU_0 && (2.28a)\\
&= 9F_{\text{res}}, \\
\text{radial: } \Delta F_{\max} &= \frac{U_0}{w_0}\sqrt{\frac{2}{e}} && (2.28b)\\
&= 0.05F_{\text{res}}. \\
& && (2.28c)
\end{aligned}$$

For atoms under near-resonant illumination with $E = 0.5\,U_0$, eq. 2.26 yields a heating rate due to dipole force fluctuations which in axial direction is 40-times as strong as recoil heating, but is negligible in radial direction. Thus the axial temperatures could be larger than radial temperatures during continuous illumination (sec. 2.5.2) and during the transfer from the MOT into the dipole trap. Since the magnitude of this heating effect depends on the temperature of the atoms and the equilibration rate of axial and radial temperature is unknown, a simulation of the relevant heating and (sub-)Doppler cooling mechanisms could provide additional insight into the cooling dynamics in our trap.

2.4.3 Trap depth and position fluctuations

Technical noise on the intensity and the position of the dipole trap laser beam causes the trap depth and the trap position to fluctuate in time. While individual fluctuations can increase or decrease the oscillatory energy of a trapped atom, in the long run stochastic fluctuations always lead to heating. It turns out that neither intensity noise nor pointing instability cause noticeable heating in our experiment. However, the lifetime of atoms in our dipole trap is severely limited by electronic phase noise transferred by the AOMs onto the trapping laser beams.

Laser intensity noise

The heating effect depends on the amplitude and on the spectral distribution of the intensity fluctuations $\Delta I = I(t) - \langle I \rangle$ around the average intensity $\langle I \rangle$. The fluctuations are characterized by the spectral density of the relative intensity noise $S(\nu)$, which is defined such that the normalized variance of the intensity due to fluctuations in a spectral band $\mathrm{d}\nu$ around the frequency ν is

$$\frac{\langle (\Delta I)^2 \rangle_{\mathrm{d}\nu}}{\langle I \rangle^2} = S_I(\nu)\mathrm{d}\nu, \tag{2.29}$$

and thus

$$\frac{\langle (\Delta I)^2 \rangle}{\langle I \rangle^2} = \int_0^\infty S_I(\nu)\,\mathrm{d}\nu. \tag{2.30}$$

Since the trap depth U is directly proportional to the trapping laser intensity I, the relative intensity fluctuations equal the relative fluctuations of the spring constant of the trap.

When their magnitude is small, $\Delta I \ll \langle I \rangle$, the oscillation amplitude changes only slightly within one period of oscillation. Under this assumption and in harmonic approximation, the average heating rate can be calculated either classically [63], or quantum-mechanically using time-dependent perturbation theory [64]. The energy of an atom with an oscillation frequency ν_0 grows exponentially as

$$\langle \dot{E} \rangle = \pi^2 \nu_0^2 S_I(2\nu_0) \langle E \rangle. \tag{2.31}$$

Only fluctuations at twice the oscillation frequency contribute to the heating as it is expected for parametric excitation (see sec. 2.4.4). Due to the factor ν_0^2, high oscillation frequencies are more critical than low frequencies.

The relative intensity noise of our Nd:YAG laser beam was measured with an amplified photodiode. Within its bandwidth of DC to 3 MHz, the spectral voltage noise density was determined with a spectrum analyzer (Hewlett Packard, model 3589A). By dividing by the DC voltage we obtain the relative intensity noise shown in fig. 2.10(a). At low frequencies, $1/f$-noise and the power line frequency and its harmonics dominate. Peaks at intermediate frequencies are probably due to the switch mode power supply of the Nd:YAG laser, or due to relaxation oscillations. At high frequencies the noise becomes flat and reaches the theoretical shot noise of the photocurrent determined from the DC output voltage. This does not mean that the laser operates shot noise limited at these frequencies, because only a tiny fraction (about 15 µW) of the total beam power was used for this measurement. Since the *relative* shot noise scales with the measured power P as $1/\sqrt{P}$, the sensitivity could be improved by using photodiodes which respond linearly up to higher powers P.

From the exponential energy growth of equation (2.31) the energy e-folding time τ can be obtained as a characteristic heating time constant, see fig. 2.10(b). If an oscillation frequency of the atom in the dipole trap would coincide with one of the large peaks of the noise spectrum, a worst case heating time constant of about 10 s would result. The corresponding maximum ($E = U_0/2$) heating rate is $\langle \dot{E} \rangle = 150$ µK/s.

Pointing stability

A shift of the center of a harmonic trap is equivalent to a constant force acting on the atom in the unshifted potential. Fluctuations of the position of the trap therefore effectively exert a stochastic force which can heat a trapped atom by inducing a random walk in phase space. Position fluctuations of the dipole trap can be caused by acoustical vibrations of the optical elements or by pointing instabilities of the laser source.

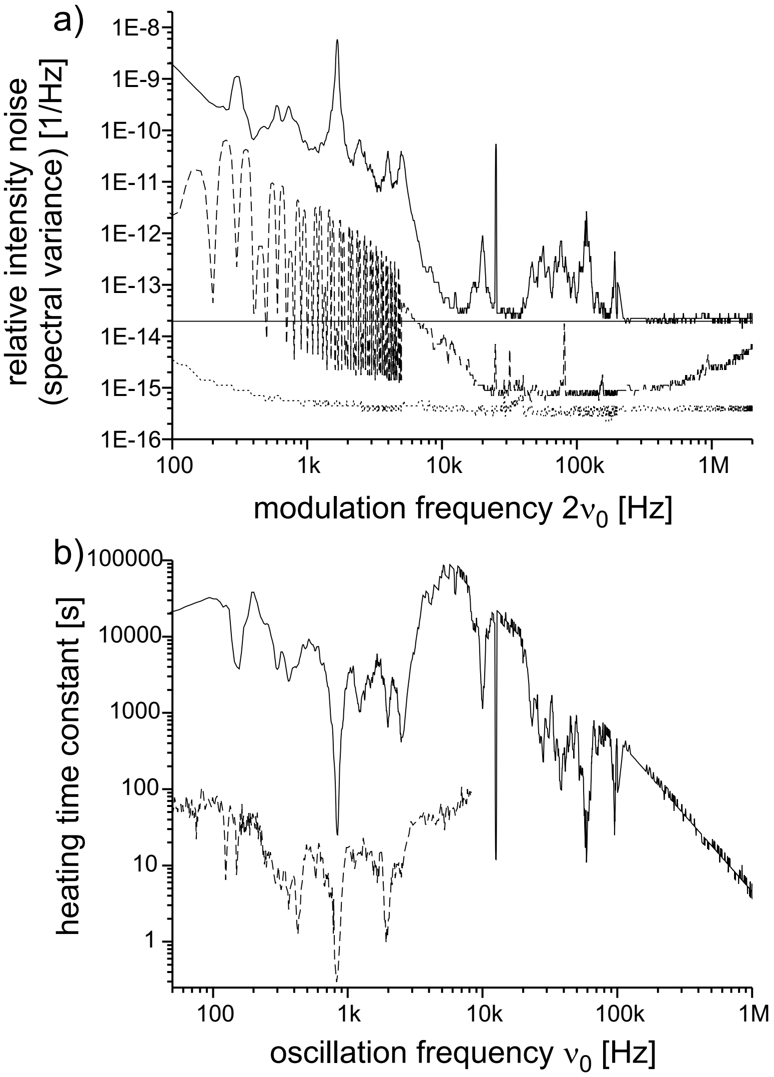

Figure 2.10: (a) Spectral density of the relative intensity noise of our dipole trap laser, S_I (continuous line). The dashed line is the noise of the photodiode amplifier (laser beam blocked), and the dotted line shows the input and ambient noise of the spectrum analyzer alone (amplifier switched off). The straight horizontal line indicates the theoretical shot noise level. (b) Continuous line: Corresponding e-folding time of the energy of a trapped atom versus its oscillation frequency, calculated after eq. (2.31). For $\nu_0 > 100$ kHz, detection shot noise masks the true intensity fluctuations (see text). The corresponding e-folding times are therefore merely lower bounds. Dashed line: Heating times according to intensity fluctuations deduced from beat signal measurement described on the following pages.

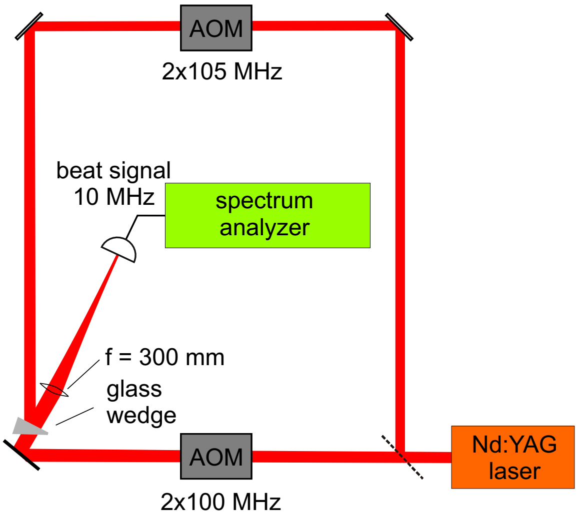

Figure 2.11: For the measurement of the beam pointing stability, the two laser beams of the dipole trap are mutually detuned with the AOMs and are overlapped on a photodiode. The amplitude of the resulting beat signal is recorded by a spectrum analyzer.

The fluctuations of the trap position $\Delta x(t)$ are characterized by the spectral density of their variance $S_{\Delta x}(\nu)$ in analogy to eq. (2.29), such that

$$\langle(\Delta x)^2\rangle = \int_0^\infty S_{\Delta x}(\nu)\,\mathrm{d}\nu. \tag{2.32}$$

For fluctuation amplitudes which are small compared to the oscillation amplitude of the atom, the average heating rate can be derived using the same methods as for the intensity fluctuations [63, 64]

$$\langle\dot{E}\rangle = \pi^3 m \nu_0^4 S_{\Delta x}(\nu_0). \tag{2.33}$$

Only fluctuations at the oscillation frequency ν_0 contribute to the heating as it is expected for resonant excitation (see sec. 2.4.4).

The spatial stability of the standing wave dipole trap inside the vacuum cell is not known. The relative position fluctuations between the two counter-propagating laser beams, however, have been measured by interfering them on a photodiode [5, 7]. Under the assumption of uncorrelated fluctuation of the two beams, the position fluctuation of the trap center can be deduced. As shown in fig. 2.11, the frequencies of the beams were mutually detuned by 10 MHz using the AOMs. The beams were then overlapped and focused down to the same waist which is used in the dipole trap (w_0 = 30 µm). The fast photodiode was connected to a spectrum analyzer (Hewlett Packard, model 3589A), which was used in "zero span" mode such that the amplitude A of the resulting 10 MHz beat signal was obtained as a time series with a bandwidth equal to the maximum filter (resolution) bandwidth of 10 kHz. From a fourier transform of this time series a frequency spectrum of the relative variance $\langle(\Delta A)^2\rangle/\langle A\rangle^2$ is obtained.

The amplitude of the 10 MHz beat signal is directly proportional to the spatial overlap of the two Gaussian beams and to the total beam power. To distinguish between these two parameters, the measurement was performed first with well overlapped beams, where the influence of position fluctuations is suppressed, since they produce only a second order effect on the beat amplitude. A second measurement was performed with only partially overlapped beams to obtain a strong, first order response. As shown in fig. 2.12(a), the two corresponding spectra differ significantly only for frequencies below 30 Hz. This would lead to the conclusion that the fluctuations of the beat signal were dominated by pointing instabilities below that frequency, and by intensity noise above. The directly measured intensity fluctuations of fig. 2.10 are, however, two orders of magnitude smaller. A possible reason for the larger amplitude of the beat signal is that in this case the beams were brought to interference after passing the complete optical setup consisting of the AOMs, telescopes and many mirrors. The optical elements could, in principle, also convert fluctuations of the beam position into intensity fluctuations, for example via interference effects or due to dirt causing position-dependent transmission. In contrast, the intensity fluctuations of fig. 2.10 were recorded in a much simpler measurement by coupling out a part of the beam close to the laser output.

To calculate the fluctuation of the relative position Δx of the two laser beams from the beat signal amplitude A, we write A as interference term or "overlap integral" of two Gaussian electric field distributions

$$\begin{aligned} A(\Delta x) &= E_0^2 \iint e^{-\frac{x^2+y^2}{w_0^2}} e^{-\frac{(x-\Delta x)^2+y^2}{w_0^2}} \,\mathrm{d}x\,\mathrm{d}y && (2.34a) \\ &= E_0^2 \frac{\pi w_0^2}{2} e^{-\frac{(\Delta x)^2}{2w_0^2}} . && (2.34b) \end{aligned}$$

For the partial overlap, one beam was displaced by Δx_0 such that the amplitude A dropped in half, which corresponds to

$$\Delta x_0 = w_0\sqrt{2\ln 2}. \tag{2.35}$$

By linearization of $A(\Delta x)$ around Δx_0 and normalization to $A(\Delta x_0)$ we obtain the position fluctuations $\delta\Delta x$ from the relative amplitude fluctuations as

$$\delta\Delta x = \frac{w_0}{\sqrt{2\ln 2}} \frac{\delta A}{A(\Delta x_0)}. \tag{2.36}$$

By measuring relative fluctuations, we are, for example, insensitive to an intensity mismatch of the two interfering beams.

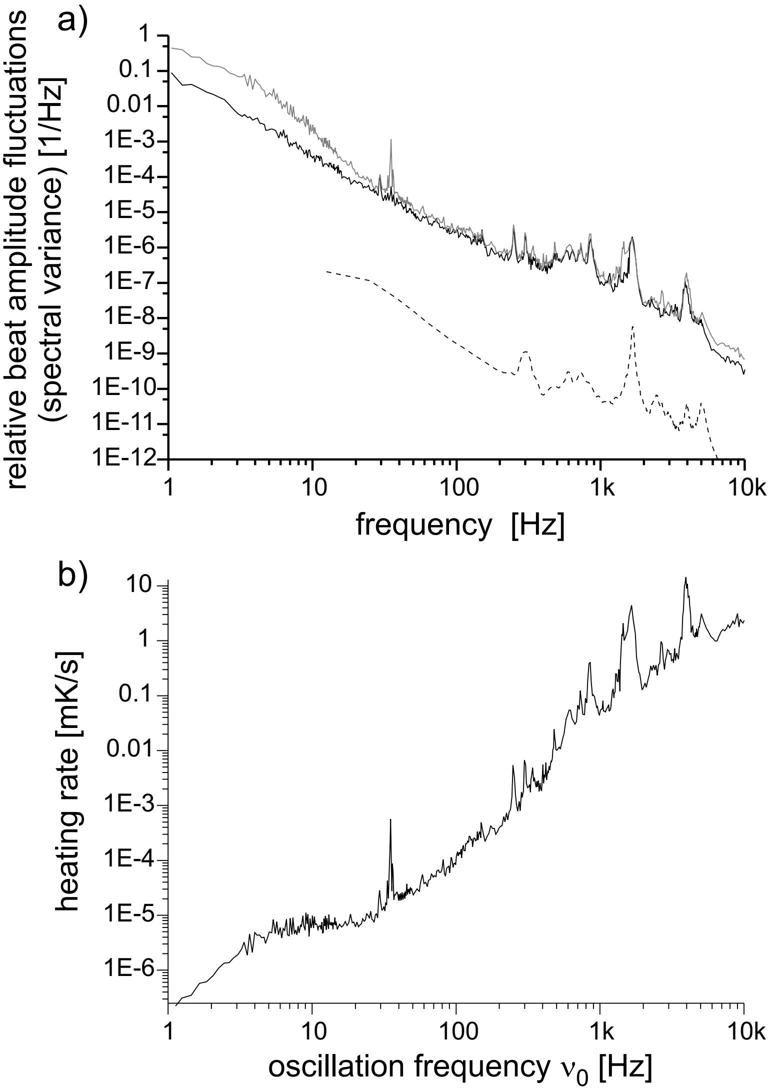

Figure 2.12: (a) Spectral variance of the relative beat signal amplitude for well overlapped (black curve) and partially overlapped (gray curve) dipole laser beams. For comparison, the influence of the intensity noise of fig. 2.10 is shown as dashed curve. (b) Heating rate of trapped atoms versus oscillation frequency due to the position fluctuations estimated from (a).

When we assume that the measured fluctuations of the relative beam positions are caused by uncorrelated position fluctuations $\{\delta\Delta x_1, \delta\Delta x_2\}$ of the individual beams of equal magnitude, we can estimate these as

$$\delta\Delta x_{1,2} = \delta\Delta x/\sqrt{2}. \tag{2.37}$$

The position fluctuations of the trap center the follow as

$$\delta\Delta x_{\mathrm{c}} = (\delta\Delta x_1 + \delta\Delta x_2)/2 = \delta\Delta x/2. \tag{2.38}$$

When all fluctuations of the beat signal amplitude are interpreted as position fluctuations, eq. (2.33) can be used to calculate the corresponding heating rates shown in fig. 2.12(b). For typical radial oscillation frequencies of $\nu_0 = 1 - 3$ kHz, heating rates of 0.2–5 mK/s are predicted. These values are probably too high, since the storage time of $\tau = 25$ s (sec. 1.3.2) indicates an upper limit of the heating rate on the order of $U_0/\tau \approx 0.05$ mK/s. However, the anharmonicity of the radial potential causes a decrease of the oscillation frequency and the heating rate with increasing energy of the atom. Therefore it cannot be excluded that the heating rate in the harmonic part of the potential exceeds the value of U_0/τ.

For a more systematic investigation of the pointing stability, one could obtain an independent measurement of the pointing stability by focusing one laser beam down to the same waist used in the dipole trap and blocking half of the beam by a knife edge. The transmitted power is then sensitive to position fluctuations, and its spectrum could be directly compared to the pure intensity noise spectrum measured without the knife edge.

The laser itself is probably not the dominating source of the relative beam pointing instabilities. By analyzing the optical setup, we found that a tilt of the beam at the output of the laser shifts both interfering dipole trapping beams into the *same* direction, producing no *relative* shift. A possible cause for the fluctuations are wavefront distortions due to convection and turbulent mixing of air currents of different temperatures. Such wavefront aberrations are easily observed in our lab when an expanded, collimated laser beam is analyzed with a shear plate interferometer (app. B.2) while turbulence is created by blowing air into the beam.

The fluctuations of the amplitude of the measured beat signal of fig. 2.12 (a) for the case of well-overlapped beams can be interpreted as intensity fluctuations of the trapping beams. The corresponding fluctuations of the trap depth would then cause parametric heating. This interpretation yields the energy e-folding times shown in fig. 2.10 (b) as dashed curve. These rather short heating times are still compatible with the lifetime of $\tau = 25$ s as long as the radial oscillation frequency does not coincide with a strong noise peak of the laser, and the anharmonicity is taken into account.

Optical phase noise

For the operation of the optical conveyor belt, the two counter-propagating laser beams of our dipole trap are mutually shifted in frequency using AOMs to move the standing wave pattern (sec. 1.3.3). Any fluctuation of the relative phase $\Delta\phi$ of the two driving frequencies therefore directly translates into a fluctuation of the axial position Δz of the potential wells, possibly heating up the atoms.

We measured the differential phase noise of our dual frequency synthesizer that we use to drive the AOMs by heterodyning its suitably attenuated outputs on a phase detector (Mini-Circuits RPD1). The output voltage of a phase detector depends on the phase difference between its inputs as

$$U_{\mathrm{out}}(\Delta\phi) = U_{\mathrm{peak}} \cos(\Delta\phi). \tag{2.39}$$

By setting the synthesizers to slightly different frequencies, U_{peak} is measured and the waveform is checked to be sinusoidal. When the synthesizers run at the same frequency and with a phase difference of 90° such that $U_{\mathrm{out}} \approx 0$, the rms phase noise is

$$\Delta\phi_{\mathrm{rms}} = \frac{U_{\mathrm{out,rms}}}{U_{\mathrm{peak}}}. \tag{2.40}$$

Due to the double-pass setup of the AOMs, the optical phase noise is twice the electronic phase noise, and the position shift of the trap is

$$\Delta z_{\mathrm{rms}} = \frac{\Delta\phi_{\mathrm{rms}}}{k}. \tag{2.41}$$

We measured a phase noise of $\Delta\phi_{\mathrm{rms}} \approx 10^{-3}$ rad with an essentially flat spectrum from 100 kHz to 1MHz. For an axial oscillation frequency of $\nu_0 = 380$ kHz equation (2.33) predicts a heating rate of $\langle \dot{E} \rangle \approx 4$ mK/s.

A heating rate of this magnitude is indeed indicated by a comparison of the lifetime of trapped atoms measured with and without using the AOMs at otherwise similar trap parameters, see fig. 2.13. When the phase noise is present, the lifetime drops to a few seconds and the decay becomes non-exponential. The low initial loss rate is probably due to the low initial energy of the atoms, which have to be heated up by nearly the full trap depth U_0 before they begin to escape [64]. The lifetime is still longer than $U_0/\langle \dot{E} \rangle \approx 0.4$ s by an order of magnitude. This can be explained by the fact that once the atom is heated to near U_0, its oscillation frequency ν_0 drops to zero due to the anharmonicity of the trapping potential. Since the heating rate is proportional to ν_0^4, already a moderate reduction of the oscillation frequency can slow down the heating process by an order of magnitude.

A more quantitative estimate of the heating time is obtained from a numerical trajectory simulation of the heating process [52]. The equations

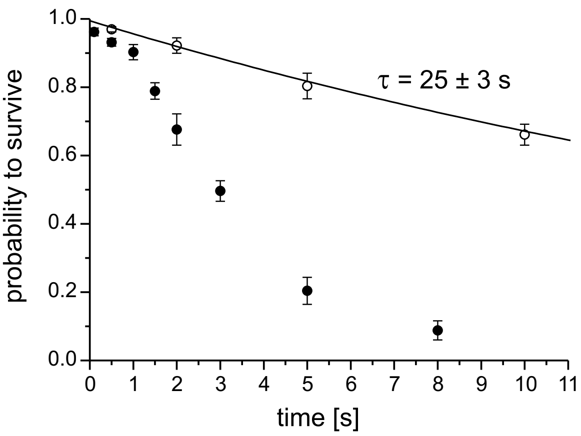

Figure 2.13: Lifetime measurement with (filled circles) and without (hollow circles) phase noise at otherwise identical conditions. The full lifetime data without phase noise is shown in fig. 1.15.

of motion of an atom in the one-dimensional potential

$$U(z,t) = U_0 \cos^2(k(z - \Delta z(t))) \tag{2.42}$$

are solved numerically with the Runge-Kutta method. The position fluctuations of the trap $\Delta z(t)$ are modeled as white noise with a bandwidth of 0–1 MHz. This noise is generated by choosing random numbers which are Gaussian distributed with an rms amplitude corresponding to the measured rms phase noise. To fill the required bandwidth, two million random numbers are drawn for one second of simulated time, and interpolated with a spline function. According to the sampling theorem, the spectrum then extends to 1 MHz. The average time it takes the atom to leave its potential well is proportional to $1/\Delta z_{\mathrm{rms}}^2$ and reaches about one second for the experimental fluctuation amplitude, in reasonable agreement with the lifetime.

2.4.4 Heating during transportation

Another technical source of heating is observed when atoms are transported at certain speeds using the optical conveyor belt [53]. It turns out that the potential slightly “wobbles” and resonantly or parametrically excites the atoms.

One of the dipole trap beams leaves the vacuum chamber through the front face of the glass cell. As this facet is not anti-reflection coated, about 4% of the power per surface is reflected back into the trapping region, see fig. 2.14. After divergent expansion, this third beam interferes with the two main laser beams and slightly changes the amplitude and phase of their interference pattern. When atoms are transported by mutually detuning

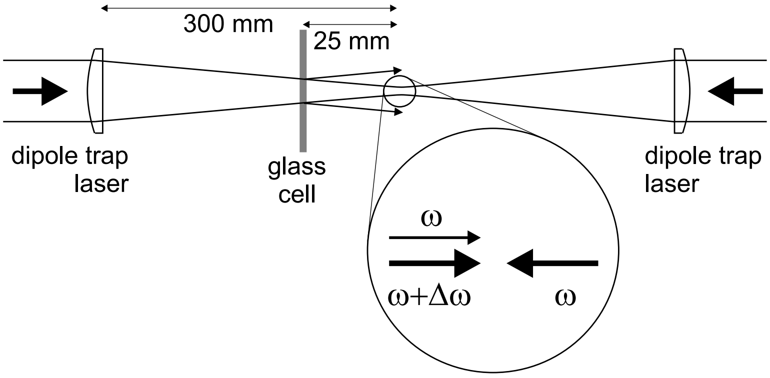

Figure 2.14: A partial reflection of the trapping beam at one of the vacuum cell windows interferes with the dipole trap. The frequencies are shown in the laboratory frame of reference.

the trapping beams by $\Delta\omega$, both phase and amplitude are modulated at that frequency. The other vacuum window is much further away from the trapping region and is anti-reflection coated, therefore the second reflection is neglected.

In the atomic frame of reference moving with a velocity $v = \Delta\omega/(2k)$, the total electric field is the sum of the main standing wave and the weak third beam,

$$E(z,t) \sim 2\cos(\omega t)\cos(kz) + \beta\cos[(\omega - \Delta\omega)t - k'z], \tag{2.43}$$

where $\beta \ll 1$ denotes the amplitude of the reflected beam in units of the incident beam amplitude. The trapping potential is obtained as the average of $E(z,t)^2$ over one optical cycle. With $k' \approx k$ and to first order in β we have

$$U(z,t) = -U_0\left(\cos^2(kz)[1+\beta\cos(\Delta\omega t)] - \beta\cos(kz)\sin(kz)\sin(\Delta\omega t)\right). \tag{2.44}$$

Setting

$$\Omega_z^2 = \frac{2U_0k^2}{m} \tag{2.45}$$

the equation of motion becomes

$$\ddot{z} + \Omega_z^2[1+\beta\cos(\Delta\omega t)]z = -\beta\frac{\Omega_z^2}{2k}\sin(\Delta\omega t). \tag{2.46}$$

It shows resonant excitation for $\Delta\omega = \Omega_z$ due to the driving force on the right hand side, as well as parametric excitation for $\Delta\omega = 2\Omega_z$ due to the modulation of the spring constant on the left hand side.

Resonant heating rate

For $\Delta\omega = \Omega_z$, the modulation of the spring constant has no significant effect for $\beta \ll 1$ and is therefore neglected. A solution of the resonant equation of motion

$$\ddot{z} + \Omega_z^2 z = \frac{\beta\Omega_z^2}{2k}\sin(\Omega_z t) \tag{2.47}$$

with $z(0) = 0$ is

$$z(t) = -\frac{\beta\Omega_z}{4k} t\cos(\Omega_z t). \tag{2.48}$$

Since the amplitude of oscillation grows linearly with time, the energy increases quadratically and the heating rate is not constant. We define a characteristic resonant heating time t_{res} as the time needed to increase the atomic energy from zero to U_0,

$$t_{\mathrm{res}} = \frac{4}{\beta\Omega_z}. \tag{2.49}$$

Parametric heating rate

For $\Delta\omega = 2\Omega_z$, the driving force of eq. (2.46) is neglected. To estimate the energy gain of the oscillating atom, we write the parametric equation of motion

$$\ddot{z} + \Omega_z^2[1 + \beta\sin(2\Omega_z t)]z = 0 \tag{2.50}$$

such that the modulation appears as an external force,

$$\begin{aligned} m\ddot{z} + m\Omega_z^2 z &= -m\Omega_z^2\beta z\sin(2\Omega_z t) && \text{(2.51a)} \\ &= F_{\mathrm{ext}}. && \text{(2.51b)} \end{aligned}$$

For small β, the oscillatory motion is nearly sinusoidal and its amplitude grows so slowly that it is approximately constant over one oscillation period,

$$z(t) = z_0\cos(\Omega_z t). \tag{2.52}$$

The heating rate is calculated as the power $P(t) = F_{\mathrm{ext}}(t)\dot{z}(t)$ delivered by the external force, averaged over one oscillation period,

$$\dot{E} = \frac{\beta\Omega_z}{2}E. \tag{2.53}$$

Since in this case the energy grows exponentially, we define the characteristic timescale by the e-folding time

$$t_{\mathrm{para}} = \frac{2}{\beta\Omega_z}. \tag{2.54}$$

To estimate the relative amplitude β of the third beam, its expanded radius w_{exp} at the trap position is calculated from the known beam parameters (1.43). Note that the reflections off both surfaces of the glass cell interfere, such that the total reflected power can range from zero to 16% and equals 8% only in average. We therefore have

$$\begin{aligned} \beta &= \frac{w_0}{w_{\mathrm{exp}}}\sqrt{0.08} && \text{(2.55a)} \\ &\approx 0.012. && \text{(2.55b)} \end{aligned}$$

The characteristic heating times

$$\begin{aligned} t_{\mathrm{res}} &= 180\ \mu\mathrm{s} && \text{(2.56a)} \\ t_{\mathrm{para}} &= 90\ \mu\mathrm{s} && \text{(2.56b)} \end{aligned}$$

result in maximum heating rates on the order of

$$\begin{aligned} \dot{E}_{\mathrm{res}} \approx \frac{U_0}{t_{\mathrm{res}}} &\approx 8\ \mathrm{K/s} && \text{(2.57a)} \\ \dot{E}_{\mathrm{para}} \approx \frac{U_0}{t_{\mathrm{para}}} &\approx 16\ \mathrm{K/s}. && \text{(2.57b)} \end{aligned}$$

These heating rates occur only as long as the excitation is exactly resonant with the oscillatory motion. Any frequency deviation will dephase the oscillation and stop the heating process, be it due to the anharmonicity of the potential or due to the reduction of the trap depth as the atom is transported further away from the focus of the dipole trap.

2.4.5 Measurement of the axial oscillation frequency

We used this heating mechanisms to measure the axial oscillation frequency by transporting the atoms for some time with fixed mutual detuning $\Delta\omega$ of the two dipole trap beams, and observing an increase of the oscillation amplitude. For this purpose, we accelerate the atoms by a suitable short frequency ramp to a velocity $v = \Delta\omega/(2k)$ and transport them over 2 mm with constant velocity. After deceleration, the atoms are brought back to the position of the MOT by a similar transport in the opposite direction. As we transport the atom away from the focus of the dipole trap, the trap depth, and thus the oscillation frequency, decreases. We therefore fix the transportation distance to 2 mm to limit the reduction of the oscillation frequency to 20%. Further, this sweep of the oscillation frequency during the excitation smears out the resonance linewidth and thus prevents us from missing the possibly very narrow resonances when sampling the excitation frequency $\Delta\omega$.

The measurement procedure is shown in fig. 2.15. After transferring a known number of atoms into the dipole trap, they are transported using

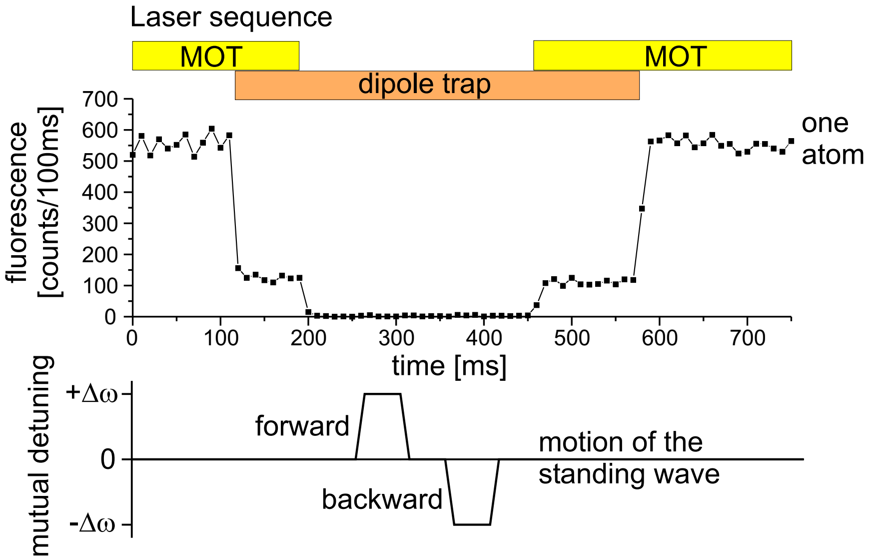

Figure 2.15: Measurement procedure for the axial oscillation frequency. A single atom is loaded from the MOT into the dipole trap. It is then transported forth and back using trapezoidal frequency ramps. After a temporary reduction of the trap depth (not shown), the survival of the atom is detected by recapturing it back into the MOT.

trapezoidal frequency ramps to expose them to the resonant and parametric heating at $\Delta\omega$. Because of the anharmonicity of the trapping potential, this excitation does not necessarily lead to a loss of atoms, because they shift out of resonance before leaving the trap. To decide whether an atom has been resonantly heated or not, we reduce the depth of the dipole trap within 10 ms adiabatically to 10% of its initial value U_0. This threshold has been optimized to keep most of the atoms trapped in the absence of resonant heating, but to lose a substantial fraction of heated atoms. Any remaining atom is recaptured into the MOT and counted via its fluorescence.

The survival probability is obtained from about 100 repetitions with on average one atom per repetition. Fig. 2.16 shows the survival probability versus the detuning $\Delta\omega$. The clearly visible dips at $\Delta\omega/(2\pi) = 330 \pm 5$ kHz and $\Delta\omega/(2\pi) = 660 \pm 15$ kHz correspond to the direct and parametric resonance. Since Ω_z decreases already by 20% over the transportation distance of 2 mm, the measured resonance frequency could be systematically too low by about 10%. In this view it agrees reasonably well with the theoretical expectation of $\Omega_z = 410$ kHz. The remaining discrepancy could be caused by any loss of trapping laser intensity at the focus, e. g. due to wavefront aberrations, or by reduced interference contrast, e. g. due to imperfect overlap of the two counterpropagating beams or imperfectly matched polarizations. For example, a lateral shift of one trapping beam by 20 µm reduces the trap

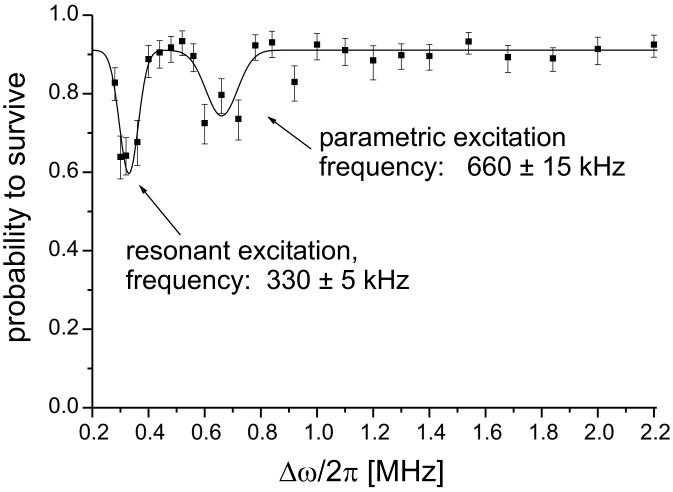

Figure 2.16: Measured survival probability as a function of the detuning $\Delta\omega$ used for transportation. The curve is a fitted sum of two Gaussians.

depth from 1.5 mK to 1.2 mK. When we assume 100% interference contrast, the trap depth at the focus would be estimated to be around 1.0–1.2 mK, depending on the systematic deviation of the measured resonance frequency.

Alternative methods to measure the (axial) oscillation frequency include parametric excitation by modulating the dipole trap depth at $2\Omega_z$ using the AOMs, and detection of motional sidebands using Raman spectroscopy [65].

We can estimate the average heating rate during the resonant excitation from the energy gain of the atoms. During the adiabatic lowering of the trap depth to $0.1\,U_0$ all atoms with $E_0 > 0.35\,U_0$ are lost, see fig. 2.5. This leads to a survival probability of about 90% off resonance. From the cumulative energy distribution (fig. 2.8) we see that the survival probability of 60% observed on resonance corresponds to a loss of atoms with $E_0 > 0.1\,U_0$. These atoms must have gained an energy of $0.25\,U_0$ during the resonant excitation period of 20 ms to reach the escape energy of $0.35\,U_0$. From these values, a time-averaged heating rate of about 16 mK/s is obtained. In the same way a parametric heating rate of about 13 mK/s is found. These heating rates are much smaller than the maximum theoretical heating rates (2.57), which supports the conjecture that the exact resonance condition is fulfilled only for a short time before the oscillation dephases.

2.4.6 Comparison of heating rates

The various heating rates are summarized in table 2.1. The fundamental heating rates, i. e. recoil and dipole force fluctuation heating, are negligible. When transportation is not used, the most severe sources of heating are

Heating effect	Heating rate		Comments
recoil heating	6×10^{-4} mK/s	calc.	
dipole force fluct. (axial)	10^{-8} mK/s	calc.	
laser intensity fluct. (radial)	up to 0.07 mK/s	calc.	depends strongly on Ω_{rad}
laser intensity fluct. (axial)	up to 0.15 mK/s	calc.	depends strongly on Ω_z
laser pointing stability (radial)	up to 5 mK/s	calc.	interpretation of pointing stability measurement unclear
	< 0.05 mK/s	obs.	from lifetime (in harmonic approximation)
optical phase noise (axial)	4 mK/s	calc.	in harmonic approximation
	1 mK/s	calc.	average, from numerical simulation
	0.4 mK/s	obs.	average, from lifetime
resonant excitation (axial) during transportation	8000 mK/s	calc.	only in exact resonance
	10 mK/s	obs.	averaged value
parametric excitation (axial) during transportation	16000 mK/s	calc.	only in exact resonance
	10 mK/s	obs.	averaged value

Table 2.1: Summary of the heating mechanisms in the dipole trap and the corresponding heating rates.

laser intensity noise and pointing instabilities. We hope that this technical noise is significantly reduced when our old arc-lamp pumped Nd:YAG laser is replaced with a newly bought, diode-pumped Yb:YAG laser.

When the optical conveyor belt is used to transport atoms, the strong resonant and parametric heating is usually avoided by choosing the transportation parameters such that the excitation frequency $\Delta\omega$ always stays below the axial oscillation frequency Ω_z. The heating by optical phase noise has not, up to the present stage of the experiment, impaired our measurements, since all our measurement procedures take less than one second. It might, however, become important when we want to cool the atom to the oscillatory ground state, because at $\Omega_z/(2\pi) = 380$ kHz it increases the oscillatory quantum number by 0.5/ms. The phase noise could be reduced by replacing the dual frequency synthesizer with two low phase noise frequency generators.

Additional heating occurs when the optical conveyor belt accelerates and decelerates the atoms because the full acceleration is applied suddenly. This heating effect has been analyzed in detail by S. Kuhr [5], and it can be significant already at medium accelerations. The obvious remedy is to start the acceleration slowly enough to keep the transport adiabatic with respect to the axial oscillation frequency of the atoms. This could be achieved e. g. by using frequency generators with an analogue frequency modulation input.

2.5 Temperature measurement by optical imaging

The high-resolution optical imaging system and the intensified CCD camera (sec. 1.1.5) enable us to determine the temperature of the atoms in the dipole trap from their spatial distribution. Since the photon scattering rate in the dipole trap is very low, the atoms have to be illuminated with near-resonant light for observation. The strong heating due to scattering of photons has to be counteracted by simultaneous near-resonant laser cooling. Hence, using this method, we do not measure the temperature of the atoms before illumination but rather the equilibrium temperature for laser cooling of atoms in the dipole trap. While the method of adiabatic lowering can measure arbitrary temperatures and allows to observe for example external heating effects, the measurement by optical imaging could be especially useful to evaluate and optimize laser cooling in the dipole trap. It could help us to achieve a lower initial temperature of the atoms after the transfer from the MOT into the dipole trap and therefore facilitate further cooling (sec. 4.1.1). Furthermore atomic coherence times would be improved.

2.5.1 Theory

The atoms in our dipole trap are modeled as an ensemble in thermal equilibrium at a temperature T in a three-dimensional harmonic potential. In this approximation, the three degrees of freedom decouple, and the energy of each one-dimensional motion is Boltzmann-distributed with the same temperature T,

$$p_{\mathrm{B}}(E) = \frac{1}{k_{\mathrm{B}}T} e^{-E/(k_{\mathrm{B}}T)}. \tag{2.58}$$

For a fixed energy E, the probability to find an atom at position x in a potential $U(x) = m\Omega^2 x^2/2$ is given by

$$\begin{aligned} p_E(x) &= \frac{1}{\pi\sqrt{x_0^2 - x^2}} && \text{(2.59a)} \\ x_0 &= \sqrt{\frac{2E}{m\Omega^2}} \quad \text{(turning point),} && \text{(2.59b)} \\ |x| &\leq x_0. \end{aligned}$$

The spatial distribution of a thermal atom $p_{\mathrm{th}}(x)$ is the integral of $p_E(x)$ over all energies E weighted with the Boltzmann factor,

$$\begin{aligned} p_{\mathrm{th}}(x) &= \int_0^\infty p_E(x) p_{\mathrm{B}}(E)\,\mathrm{d}E && \text{(2.60a)} \\ &= \sqrt{\frac{m\Omega^2}{2\pi k_{\mathrm{B}}T}}\; e^{-m\Omega^2 x^2/(2k_{\mathrm{B}}T)}. && \text{(2.60b)} \end{aligned}$$

The temperature is thus obtained from the width of the spatial distribution $\sim \exp(-x^2/(2\sigma^2))$ and the oscillation frequency as

$$T = \frac{m\Omega^2\sigma^2}{k_{\mathrm{B}}}. \qquad (2.61)$$

2.5.2 Continuous illumination

While a near-resonant illumination already occurs when MOT and dipole trap are operated simultaneously to transfer atoms between the two traps, first attempts to take images in this configuration were only partly successful. During the exposure time of at least 100 ms required to obtain useful images, the atoms tend to jump between different potential wells of the standing wave such that a single atom appears on several locations or is smeared out completely. Good illumination parameters have been found only after several technical improvements:

The MOT laser beams were carefully centered onto the MOT. For this purpose, each pair of counterpropagating cooling beams was scanned in the transverse plane to maximize the single atom fluorescence rate.

The intensity of counterpropagating cooling beams was made equal to about 10% in order to balance the radiation pressure on the atoms. This was achieved by keeping the cooling laser beam slightly convergent, such that after its retroreflection eventual power losses due to the glass cell and optical components are compensated by a smaller beam diameter.

The polarization of the cooling beams was checked to contain at least 99.5% of their power in the correct circularity to guarantee a pure $\sigma^+ - \sigma^-$ configuration.

The atoms are illuminated without the MOT quadrupole magnetic field present, and residual fields are compensated to 1 µT (10 mG). Intensity and detuning of the cooling laser as well as the depth of the dipole trap are optimized to prevent the atom from hopping between different potential wells or leaving the trap. Typical illumination parameters are: detuning of the cooling laser: $\Delta = -2\pi\, 5$ MHz, intensity of the cooling laser: $2\, I_0$ per beam, dipole trap depth: $U_0/k_{\mathrm{B}} = 0.7$ mK.

In this way, individual atoms have been continuously observed in the dipole trap over one minute, probably limited only by collisions with the background gas [40]. With an exposure time of 1 s, images with good signal-to-noise ratio can be obtained, see fig. 2.17.

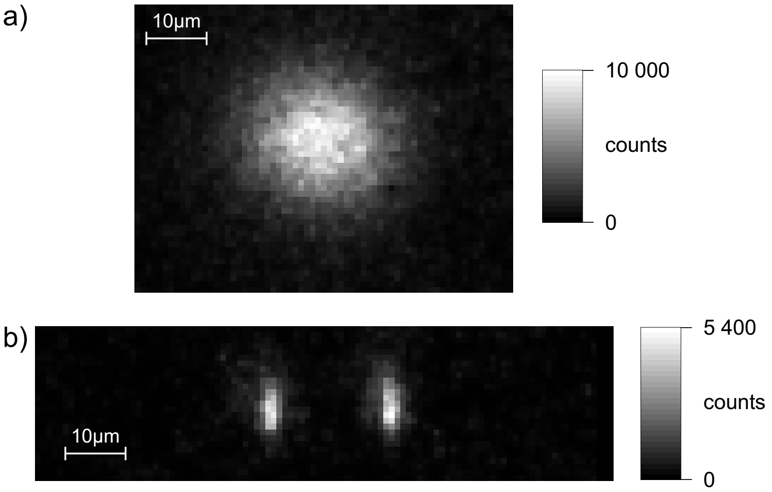

Figure 2.17: (a) CCD image of two atoms in the MOT. (b) CCD image of two atoms in the dipole trap, illuminated by the cooling and repumping beams of the MOT, but without magnetic field. In the horizontal direction, each atom is confined to one potential well ($\lambda/2$) of the dipole potential and thus appears as a vertically elongated spot. One photon detected by the image intensifier corresponds on average to about 350 counts.

2.5.3 Extracting the spatial distribution

To extract the spatial distribution of the atoms from the images, we have to ensure that the visible fluorescence intensity is proportional to the density of the atomic cloud, i. e. that the fluorescence rate of the atom is independent of its position. In principle, the light shift of the transitions in the dipole trap changes the effective detuning of the illuminating laser, and thus the scattering rate of the atom, depending on its position in the trap. Similarly, the Doppler shift influences the scattering rate depending on the local velocity. Yet, the temperature of our atoms is on the order of the Doppler temperature T_{D}. Here, the Doppler shift is on the order of $v_{\mathrm{D}}/\lambda = 0.1$ MHz, which is small compared to the natural linewidth Γ and can be neglected. Sub-Doppler cooling effects, however, could lead to a larger sensitivity of the scattering rate on the atomic velocity than calculated from the Lorentzian lineshape, which is valid only for the two-level case. The systematic error caused by this effect could be quantified only by a full quantum-mechanical treatment of the sub-doppler cooling mechanisms in the dipole trap [66].

The light shift of the ground state blue-detunes the cooling transition and thus adds to the red-detuning of the cooling laser. The effective total detuning is about $-13\,\Gamma$ in the trap center. At the turning point of the atomic motion, the light shift is reduced by about Γ for an atom at about Doppler temperature. In the low-intensity limit, this change in light shift increases the scattering rate by about 20% in the outer regions of the atomic

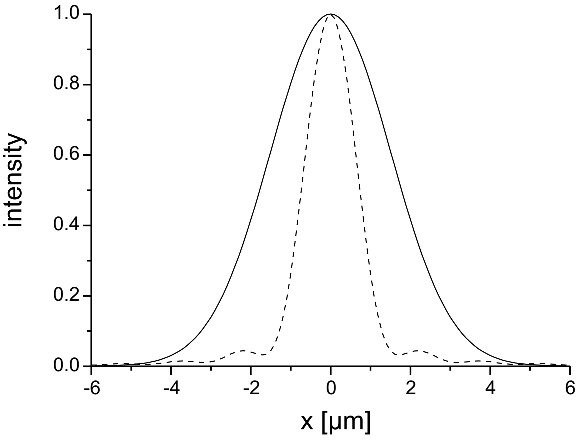

Figure 2.18: Line spread functions in terms of object-plane coordinates. Solid line: Gaussian line spread function with a width of $\sigma_x = 1.51$ µm extracted from the images. Dashed line: Theoretical line spread function of an aberration-free imaging system with a NA of 0.29

cloud, which leads to an increase of its apparent size. The temperature of the cloud might therefore be slightly over-estimated by this method.

Spatial resolution of the image

For the extraction of the spatial distribution, the blur due to the finite resolution of the imaging system has to be taken into account. The action of the imaging process on the spatial distribution can be modeled as a convolution with the point spread function of the optical system. The point spread function is defined as the intensity distribution at the image plane obtained for an ideal point source at the object plane.

The point spread function can be calculated from the numerical aperture (NA) and the aberrations of the optical system. In the absence of aberrations and for a circular, homogeneously illuminated aperture, the point spread function is given by the Airy-disc [67]

$$\begin{aligned} p(r) &= \left(\frac{2J_1(u)}{u}\right)^2 \qquad (2.62) \\ u &= \frac{2\pi r \mathrm{NA}}{\lambda}, \\ r &= \sqrt{x^2+y^2}, \end{aligned}$$

where J_1 is the first order Bessel function. When the object side NA is used in eq. 2.62, $p(r)$ is directly obtained in terms of object plane coordinates $\{x, y\}$ and determines the theoretical resolution.

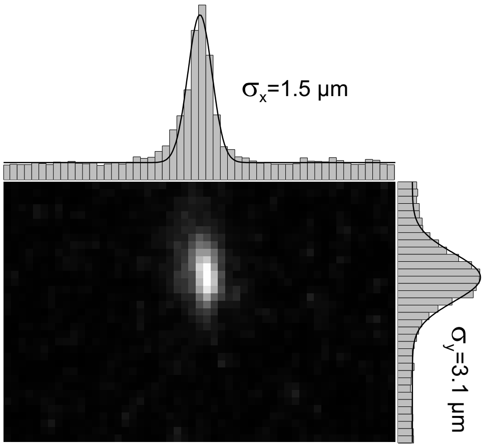

Figure 2.19: Image of one atom in the dipole trap with horizontally and vertically integrated intensity distributions and with Gaussian fits. The horizontal width of the image is determined by the resolution of the imaging system. From the vertical direction information about the radial distribution of the atoms in the dipole trap can be obtained.

The actual resolution can be extracted from the images of single atoms in the dipole trap, since in axial direction the atom is confined to a small fraction of the width of a potential well ($\lambda/2$), which is much below our optical resolution. The horizontal width of the image in fig. 2.19 is therefore determined by the so called line spread function. The line spread function is the intensity distribution at the image plane obtained for an ideal straight line source at the object plane. It is given by the integral of the point spread function along the axis of the line. The theoretical line spread function terms of object plane coordinates is shown in fig. 2.18.

To obtain the intensity distribution along the dipole trap axis, we vertically integrate the intensity in fig. 2.19 after suitably clipping the image to exclude background noise (without losing fluorescence counts). The horizontal intensity distribution is fitted with a Gaussian function

$$I(x) = e^{-\frac{(x-x_0)^2}{2\sigma_x^2}}, \tag{2.63}$$

and from 32 images an average width of $\sigma_x = 1.51 \pm 0.02$ µm is obtained.

Compared to the theoretical line spread function, this function is broader by a factor of 2.6, see fig. 2.18. There are several reasons for this discrepancy:

The image intensifier has a finite resolution determined by its own point spread function. A single photoelectron from the photocathode produces a light spot on the CCD chip with an intensity distribution which is approximately a Gaussian function with $\sigma \approx 1$ pixel ≈ 1 µm at the object plane [68]. The relative importance of the blur due to the image intensifier can be reduced by increasing the optical magnification. In this way, the effective resolution of our imaging system could probably be enhanced significantly.

The optical system easily introduces some aberrations due to a slight displacement or tilt of the components. The diffraction-limited performance of the objective lens tested in appendix B was only achieved after disassembling and reassembling the lens system several times and carefully adjusting its position on an *xyz*-stage for minimum wavefront distortion. This procedure was not performed with the objective used for the CCD camera.

Finally, the radial extent of the atomic cloud is comparable to the depth of focus of about 6 µm, which could prevent focussing the entire cloud.

When we assume that the actual point spread function is rotationally symmetric, we can use this function to deconvolute the vertical intensity distribution. In the case of aberrations such as astigmatism or coma, this assumption may not be valid, but presently we have no means to check this issue experimentally. When the second, vertical dipole trap (see sec. 4.2.3) will be installed, however, the atoms can be confined to a small fraction of $\lambda/2$ in the *two* dimensions of the object plane. This effective point source could then be used to obtain the full, two-dimensional point spread function.

The vertical (radial) intensity distribution of the images also fits well to a Gaussian function with an average width of $\sigma_y = 3.32 \pm 0.04$ µm. The deconvolution with the one-dimensional point spread function is quite simple, since the convolution of one Gaussian function with another Gaussian function results again in a Gaussian function, and the widths σ_i add quadratically,

$$\int_{-\infty}^{\infty} e^{-\frac{(x-x')^2}{2\sigma_1^2}} e^{-\frac{x'^2}{2\sigma_2^2}} \,\mathrm{d}x' = e^{-\frac{x^2}{2(\sigma_1^2+\sigma_2^2)}}. \tag{2.64}$$

The radial distribution of the atoms is thus a Gaussian with a width of

$$\begin{aligned} \sigma_{\mathrm{rad}} &= \sqrt{\sigma_y^2 - \sigma_x^2} && (2.65) \\ &= 2.96 \pm 0.05\ \mu\mathrm{m}. && (2.66) \end{aligned}$$

Radial oscillation frequency

The above images were taken with different dipole trap parameters than those of equation (1.43), since the focus of the trapping beams has been reduced to about 19 µm. To find the precise value of the radial oscillation frequency, an excitation spectrum of the radial motion was recorded by modulating the trap depth and observing an increase of the temperature of the atoms.

The procedure is similar to the one used in sec. 2.4.5. After loading the atoms into the dipole trap, we sinusoidally modulate the power of the trapping beams with a frequency ω_{exc} using the AOMs. A modulation depth of ±10% of the trap depth over 350 ms ensures a significant parametric

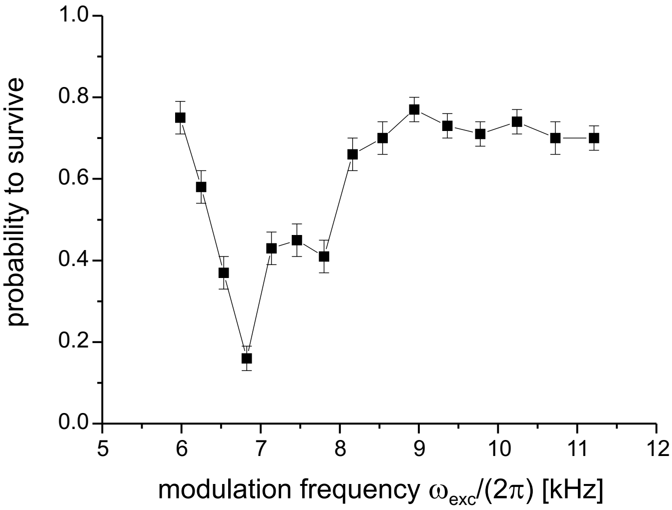

Figure 2.20: Determination of the radial oscillation frequency. Shown is the measured survival probability after parametric excitation at ω_{exc} and adiabatic lowering.

excitation. This heating is detected as an increased loss of atoms after adiabatically lowering the trap depth to 5%.

The spectrum is shown in fig. 2.20. A large fraction of atoms is heated out of the trap around $\omega_{\mathrm{exc}} = 2\pi\, 7.2$ kHz. The asymmetric line shape consisting of two individual resonances was reproduced in three more measurements, and can be explained by an ellipticity of the radial potential of the dipole trap. Since we found that the frequencies of the two resonances slowly decreases and their separation increases with time after an alignment of the dipole trap, we believe that drifts of the positions of the two counter-propagating laser beams lead to a mutual lateral displacement. An initial ellipticity could also be caused by elliptic or astigmatic laser beams.

Since the orientation of this possible ellipticity relative to the direction of observation is not known, I use a mean resonant excitation frequency of $\omega_{\mathrm{exc}} = 2\pi\,(7.2 \pm 0.4)$ kHz, leading to $\Omega_{\mathrm{rad}} = 2\pi\,(3.6 \pm 0.2)$ kHz. In order to reduce the uncertainty and temporal variation of this value, one could improve the mechanical stability of the optical setup, or use an active beam stabilization technique.

2.5.4 Results

From the width of the radial distribution and the radial oscillation frequency, a temperature of 71 ± 8 µK is obtained using equation (2.61). The quoted statistical error is mainly due to the uncertainty of the oscillation frequency. The magnitude of the systematic errors is unknown at the moment, but could be experimentally or theoretically quantified in further investigations, as indicated in this section.

The temperature itself agrees well with the result from the method of adiabatic lowering of section 2.3. Its value slightly below the Doppler temperature of 125 µK indicates weak sub-Doppler cooling effects during the continuous illumination in the dipole trap. In the future, the temperature measurement by optical imaging can hopefully be employed in the optimization of polarization-gradient cooling in the dipole trap, see section 4.1.

Chapter 3

High finesse cavity setup

A controlled coherent interaction between neutral atoms can be realized by simultaneously coupling them to one mode of the electromagnetic field. When the distance between the atoms is larger than the wavelength, the direct dipole-dipole interaction leads only to a very weak coupling. Therefore, the electromagnetic field must be confined and resonantly enhanced in a cavity. An excited atom deposits its energy as a photon in the cavity mode and reabsorbs the photon at a coupling rate g, similar to the exchange of energy between two coupled pendula. In the same picture, damping occurs due to losses by leakage and absorption of energy from the cavity field (rate κ), as well as due to spontaneous emission of the atom into other modes of the electromagnetic field (rate Γ). In the so called "strong coupling" regime, the coupling rate dominates the loss rates, $g^2 \gg \kappa\Gamma$.

By placing two atoms into the cavity mode, the cavity field emitted by the first atom can change the state of the second atom depending on the state of the first atom. Only in the strong coupling regime this process works reliably enough to use this conditional process for quantum gates. Using microwave transitions in Rydberg atoms, the strong coupling regime has been reached with superconducting cavities [69, 70], and fundamental quantum gates have been demonstrated [10]. In the optical region, the strong coupling regime has been reached [12, 13], but the controlled delivery of two atoms into the very small mode cavity volumes has yet to be attained.

We want to use our dipole trap to transport atoms into an optical cavity, since the preparation of a desired number of atoms as well as their transportation by the optical conveyor belt have already been demonstrated. A simple quantum gate could be operated by loading two atoms from the MOT into the dipole trap, preparing them in suitable quantum states (see sec. 4.2) and transporting them into the cavity. After the quantum gate is performed using their simultaneous coupling to the cavity mode, the atoms are transported back into the observation region and their final quantum states are read out.

To reach the regime of strong coupling for a given atomic transition, the coupling rate g is maximized while the loss rate κ is kept to a minimum. Since g can be viewed as the single-photon Rabi frequency, it is proportional to the electric field strength which a single photon in the cavity mode creates at the position of the atom. Only by reducing the mode volume V, the electromagnetic energy density and thus g can be increased. For this purpose, small optical resonators with very short lengths of $10 - 100$ µm are commonly used. The cavity loss rate κ is kept small by using highly reflective mirrors. The mathematical relations between g, κ and all the other cavity parameters can be found, for example, in [71].

3.1 Mechanical design

Our cavity consists of two small mirrors mounted onto an aluminum holder, see fig. 3.1. The dipole trap laser beams passing between the mirrors require a certain minimum mirror distance. In order to avoid heating of the cavity mirrors, this spacing should be significantly larger than the waist of the dipole trap laser beam. If too much laser power hits the mirrors, they thermally expand as the dipole trap is switched on, causing the highly sensitive cavity stabilization to unlock. The cavity will be placed as closely as possible to the MOT to limit the transportation distance to about 5 mm. The cylindric-conical form of the mirrors was chosen to allow the MOT laser beams to pass close to the cavity mode.

3.1.1 Mirrors

The mirrors consist of BK7 glass substrates, which have been superpolished and coated with a special, ultrahigh reflectivity coating (Research Electro Optics, Boulder). The reflectivity R is specified to greater than 99.997% at 852 nm, leading to a finesse of $F = \pi\sqrt{R}/(1 - R) > 10^5$. The radius of curvature of 1 cm and a cavity length l of 92 µm sustain a cavity TEM_{00} mode with a waist radius of $w_0 = 13.55$ µm, and a radius of $w = 13.58$ µm at the mirror surface. Diffraction losses are kept below 10^{-6} as long as the Gaussian mode is located more than $2.63\,w = 36$ µm away from the edge of the mirror. In practice, the mirrors are often chipped and scratched close to the edge, which is why we chose a diameter of the mirror surface of 1 mm. Due to the curvature of the surface, the mirror distance at the edges of the two mirrors is 25 µm smaller than the cavity length measured between the mirror centers.

When assembling a cavity, the mirrors are visually inspected under a microscope and cleaned by various methods. The reflectivity of the mirrors is characterized by measuring the optical ring-down time in a test cavity. Two selected mirrors are then glued onto the shear piezoelectric actuators on the aluminum holder by means of an alignment groove. Details of these

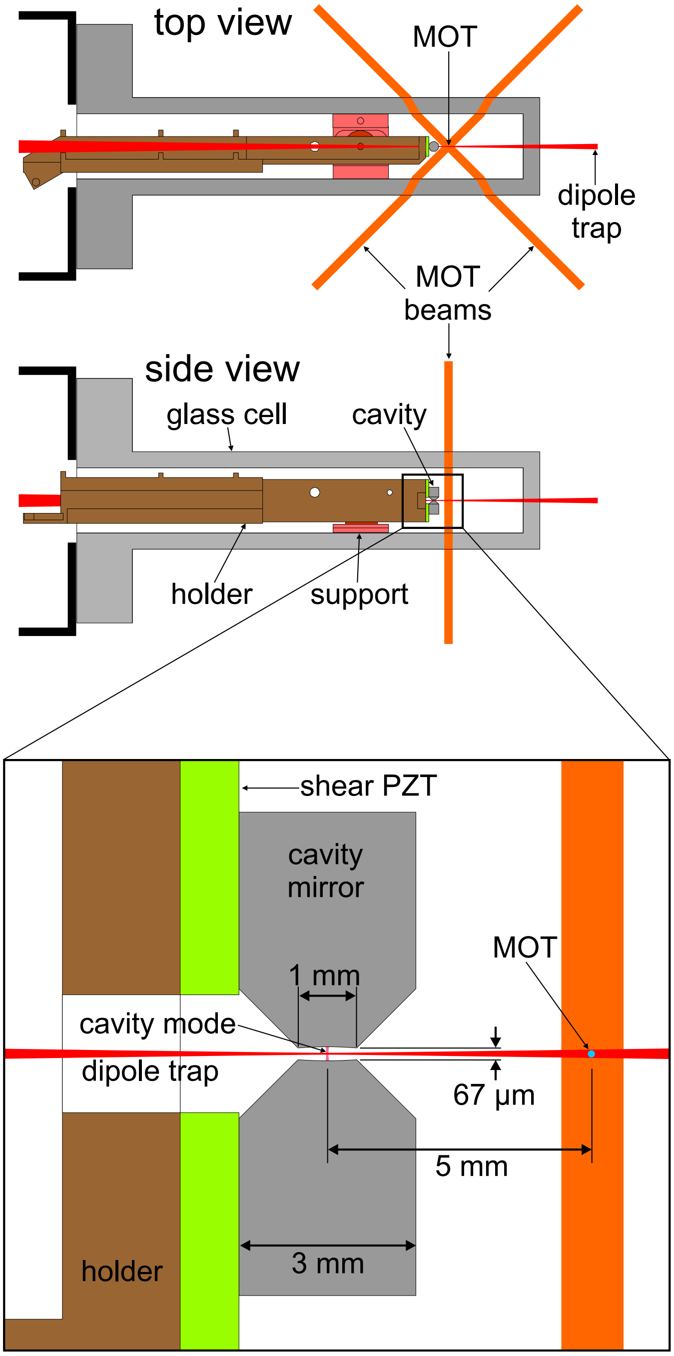

Figure 3.1: Schematic view of the cavity inside the vacuum cell.

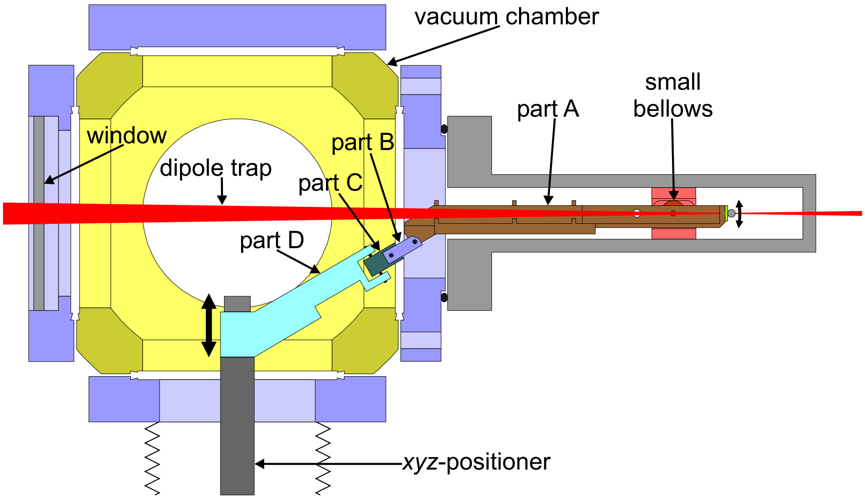

Figure 3.2: Design of the adjustable cavity holder. Part A is made of an UHV-compatible aluminum alloy (AlZnMgCu0.5), the components of the cardan joint B, C and D are made of stainless steel.

procedures are described in [14, 72]. The present cavity has the following parameters:

length: $l = 92\ \mu\text{m}$,
finesse: $F = 118000$,
free spectral range $\text{FSR} = 1.6\ \text{THz}$,
linewidth $\Delta\nu_{\text{FWHM}} = 14\ \text{MHz}$.

3.1.2 Holder

Since the position of the dipole trapping beams is fixed by the MOT and apertures outside of the vacuum chamber, the cavity mode and thus the whole cavity has to be aligned onto the dipole trap. For this purpose, the holder is made adjustable with a three-axis motional vacuum feedthrough, which consists of a linear manipulator (Thermionics Northwest, model FLMM133) held in an xy-stage (model XY-B450/T275-1.39). It connects via a cardan joint to the cavity holder, which rests inside the glass cell on a short bellows, see fig. 3.2. The bellows serves as a pivot to reduce the motion of the cavity and thus to increase the precision of the position adjustment in the sensitive directions perpendicular to the dipole trap. Coarse control of the position along the trap axis is possible by sliding the bellows on its support plate. Additionally, the bellows acts as a UHV-compatible spring for vibration isolation of the cavity. When the cardan joint is slightly lubricated with UHV grease (Fomblin), the adjustment is smooth and reaches the required precision of a few µm.

The cavity holder is designed to provide mechanical rigidity and high

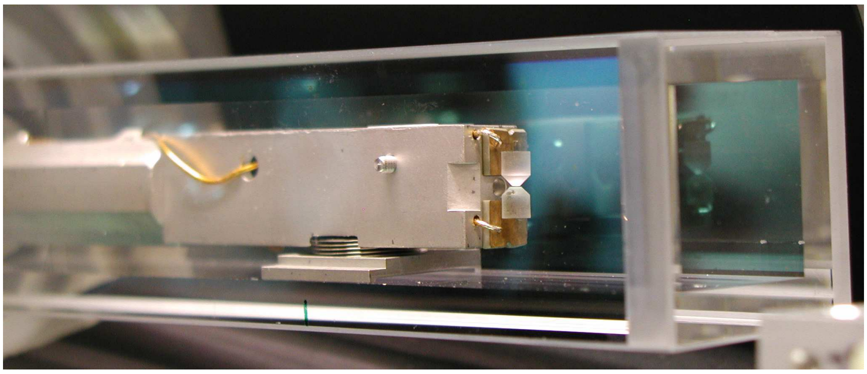

Figure 3.3: Photograph of the assembled cavity and holder in the glass cell. This picture was taken with a spare glass cell in an auxiliary vacuum chamber, which is a copy of our main experimental chamber.

self-resonance frequencies, while at the same time leaving maximum space for MOT and dipole laser beams. Additionally, it guides the wires from the piezoelectric actuators through the narrow glass cell to an electrical feed-through. Fig. 3.3 shows an assembled cavity in the glass cell.

3.2 Cavity stabilization setup

The planned experiments on atom-cavity interactions require the resonance frequency of the cavity to be stabilized on, or near to, an atomic transition frequency. Due to the high finesse of $F \approx 10^5$, this task is quite demanding: Since a shift of one free spectral range in frequency corresponds to a change in the length l of the resonator of $\lambda/2$, a frequency stability of one tenth of the resonance width requires a stabilization of l to ± 200 fm.

For this purpose, the cavity is designed for highest passive stability by mounting small, light weight mirrors on a stiff support, by applying means for vibration isolation and by utilizing the acoustic isolation provided by the ultra-high vacuum. Reaching the required short- and long-term stability, however, requires an additional active stabilization by an electronic servo loop ("lock"). The resonance frequency of the cavity is compared against a stable laser source, and the piezoelectric actuators are used to compensate fluctuations in the length l in order to keep the cavity resonant with the laser light.

3.2.1 Lock scheme

The incident power of the lock laser is enhanced in the cavity by a factor in the order of the finesse. Thus even the smallest usable lock laser power of 10-100 nW results in an intra-cavity circulating power which completely

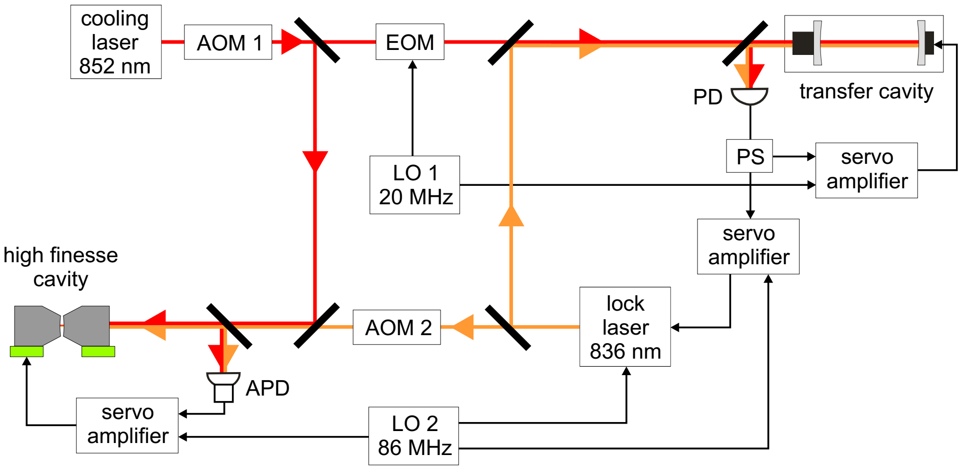

Figure 3.4: Scheme used for frequency stabilization of the high-finesse cavity. LO: local oscillator, EOM: electro-optic phase modulator, PD: photodiode, PS: RF power splitter, APD: avalanche photodiode, AOM: acousto-optic modulator. The actual double-pass configuration of the AOMs is not shown.

saturates a resonant atomic transition. Therefore we operate a lock laser at 836 nm, which is detuned far enough to keep the spontaneous scattering rate of an atom in the cavity at about 10/s, comparable to the scattering rate from the dipole trap laser. Yet, the coating of the cavity mirrors still provides the same high finesse necessary for stabilization at this wavelength.

The far detuned lock laser, however, must itself be stabilized relative to the atomic transition. The residual fluctuations and drifts of the frequency difference should be small compared to the linewidth of the cavity of typically a few MHz. Since there is no easily accessible absolute (atomic) frequency standard at the wavelength of the lock laser, we use an auxiliary cavity of moderate finesse to transfer the frequency stability of our cooling laser at 852 nm to 836 nm. As shown in fig. 3.4, the transfer cavity is locked to the cooling laser, and the lock laser is simultaneously stabilized onto a different longitudinal mode of the transfer cavity. For the detection of an atom in the cavity, a resonant probe laser at 852 nm is needed. This beam is derived from the cooling laser. AOM 2 allows us to fine-tune the resonance of the high-finesse cavity over the probe laser, whereas AOM 1 tunes the probe laser frequency and the high-finesse cavity simultaneously over the atomic resonance. This scheme for cavity stabilization is similar to the one described by H. J. Kimble et al. in [73].

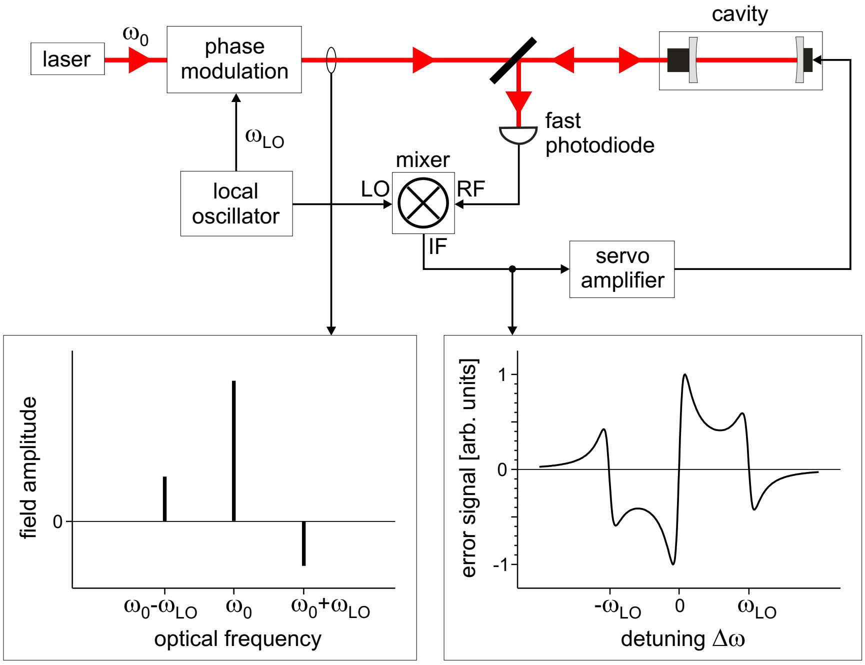

Figure 3.5: Pound-Drever-Hall method of generating an error signal of the frequency deviation of a laser beam from a cavity resonance.

3.2.2 Pound-Drever-Hall locking method

The electronic servo circuits of fig. 3.4 derive their error signals by the Pound-Drever-Hall method [74]. The light reflected from the cavity input is analyzed for its phase, which varies dispersively when the laser frequency crosses the cavity resonance. The optical phase of the main (carrier) frequency is compared to the pase of two sidebands, which are produced by phase modulation of the incident laser beam with a local oscillator, see fig. 3.5. As long as the sidebands stay off resonance, they serve as a stable phase reference for the carrier, since the phase *difference* is insensitive to fluctuations of the optical path length between laser, cavity and photodiode.

The error signal is obtained by interfering carrier and sidebands on a fast photodiode and extracting the frequency component at the local oscillator frequency with a mixer. A servo amplifier then feeds back the error signal either to the cavity or to the laser, depending on which part should be stabilized to the other.

Implementation

For the stabilization of the transfer cavity to the cooling laser, the laser beam is phase modulated with an EOM (Linos Photonics, model LM0202PHAS). For this purpose, the signal from a 20 MHz local oscillator (see app. C.2.1) is amplified to 1 W and is fed into a resonance circuit consisting of the EOM as capacitor and a small coil as inductor. The beam reflected off the transfer cavity is detected with a fast photodiode (Newport, model 818-BB-21A). A mixer circuit (see app. C.2.2) extracts the error signal, which is amplified and fed back to the piezoelectric actuator of the transfer cavity.

The lock laser is a diode laser similar to our other diode lasers (see sec. 1.1.4). It is phase modulated by a modulation of the laser diode current. The current modulation actually produces a mixture of phase and amplitude modulation of the laser beam, which shows up as a slight difference in the powers of the two sidebands. The parasitic amplitude modulation results in an offset of the error signal after it is demodulated by the mixer. This offset voltage is compensated by an adjustable offset voltage at the proportional-integral servo amplifier. Stabilization of the lock laser onto the transfer cavity proceeds by feeding the amplified error signal back to the grating and the current of the diode laser.

The stabilization of the high-finesse cavity onto the lock laser should use the least possible amount of laser power. Therefore, the reflection off the cavity is detected with an avalanche photodiode and amplified with a resonant amplifier circuit, see app. C.2.3. Since our very short high finesse cavity can have rather large resonance linewidths of a few tens of megahertz, a high modulation frequency of 86 MHz was chosen to keep the sidebands off-resonance and to obtain a large capture range of the lock. The error signal is integrated with a proportional-integral servo amplifier and further amplified by a fast high-voltage amplifier (FLC Electronics, model A800) for driving the piezo-electric actuators. A passive notch filter compensates a strong mechanical resonance of the cavity assembly at 40 kHz [14].

3.2.3 Transfer cavity

When the high-finesse cavity is resonant with the atomic transition, the lock laser frequency coincides with one of its other longitudinal modes, which are spaced in frequency by the free spectral range (FSR) of about 1.5 THz. After the lock laser is coarsely tuned to one of these resonances, it is locked to the nearest resonance of the transfer cavity. The remaining frequency gap is bridged with AOM 2 of fig. 3.4. Since the continuous tuning range of this AOM is about 50 MHz, the free spectral range of the transfer cavity has to be on the order of 100 MHz such that its modes lie sufficiently dense. The length of this cavity must therefore be on the order of 1 m.

Our transfer cavity consists of two standard laser mirrors with a radius of curvature of 2 m at a distance of 1.23 m. The exact length was chosen such that the frequencies of low order transverse modes does not coincide with the TEM_{00} mode. The mirrors are mounted on a quartz tube of low thermal expansion and insulated from vibrations by insulating foam and a brass tube. The finesse of the cavity is about 250, the linewidth about

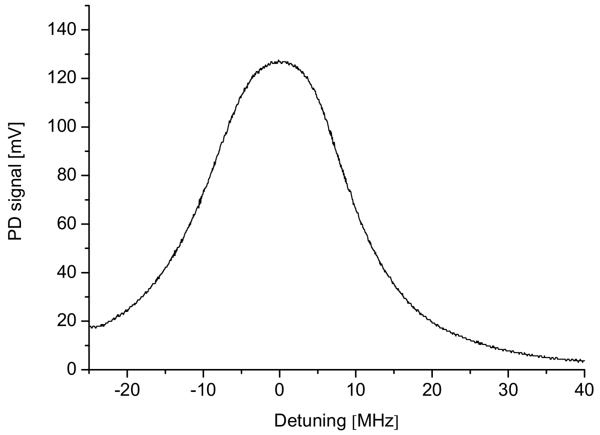

Figure 3.6: Transmission of the probe laser at 852 nm (photodiode voltage) through the high-finesse cavity, which is scanned using AOM 2 of fig. 3.4. The visible deviation from a Lorentzian lineshape is probably due to the averaging of 64 tracks in combination with residual frequency jitter.

480 kHz [72].

3.2.4 Present performance and future optimizations

The whole stabilization setup is able to lock the high-finesse cavity to the atomic resonance over a timescale of one hour, using 200 nW of lock laser power. In fig. 3.6 the cavity is scanned while in lock by ramping the frequency of AOM 2 of fig. 3.4. The lock is stable against minor disturbances like ambient noise and slight vibration of the optical table. Residual relative frequency fluctuations have been estimated from the rms-amplitudes of the error signals when the system is locked. While the fluctuations of the transfer cavity relative to the cooling laser and the lock laser relative to the transfer cavity are both below 50 kHz, the residual frequency fluctuation of the high-finesse cavity is about 2 MHz or 13% of the linewidth.

The present performance of the cavity might be sufficient to detect single atoms within the mode volume by observing a change in probe laser transmission. Numerical simulation of a scheme to entangle two atoms via the cavity [8] indicate that at least a finesse on the order of 10^6 is required [75]. The main task is of course to obtain suitable mirrors, but also some aspects of the stabilization have to be addressed due to the increased finesse.

The residual length fluctuations of the high-finesse cavity have to be reduced inversely proportional to the finesse. An increase in gain of the feedback loop would require a higher unity gain frequency, which is however limited by a number of mechanical resonances at $60-100$ kHz. At the same time, the tolerable lock laser power is reduced due to the higher resonant enhancement within the cavity. With an accordingly low signal-to-noise ratio of the error signal, an increased loop gain could even be detrimental. A good approach would be to improve the passive stability by avoiding vibrations as well as by reducing the electronic interference which presently couples somewhere into our feedback loop.

Preliminary tests have further shown that the dipole trap laser passing between the mirrors unlocks the high-finesse cavity servo. Probably, a tiny fraction of the laser beam hits the mirrors and induces a thermal change of the cavity resonance of about 10^4 linewidths. Possible solutions are to ramp the dipole trap power slowly enough that the servo loop can track the drift, or to add a suitable "feed-forward" signal to the servo voltage to precompensate the expected frequency shift.

Chapter 4

Outlook

4.1 Cooling trapped atoms

Further cooling of the atoms in our dipole trap would be beneficial for future experiments in may aspects. Cooling counteracts heating effects and thus enables prolonged storage times, more complicated transportation sequences and higher transportation efficiencies. Shallower dipole traps can be used, with reduced scattering rates and light shifts. Cooling also improves the radial localization of the atoms, which is important when they are addressed via magnetic field gradients, and when they are inserted into a cavity (sec. 4.3).

4.1.1 Raman cooling

Cooling far below the Doppler temperature is possible by the use of Raman transitions between the hyperfine ground states of cesium. For this purpose, we have built up a laser system which provides the required Raman beams [76]. Raman spectra easily resolve the motional sidebands due to the axial oscillation of the atoms in our dipole trap [65, 77]. Hence, Raman sideband cooling of the axial motion to the oscillatory ground state should be possible [78, 79].

We have not been able to resolve the sidebands caused by the slow radial oscillation. Raman cooling is still possible in this case [80], but does not reach the ground state.

4.1.2 Other cooling methods

A variant of the Raman cooling method is the degenerate Raman sideband cooling. It does not need special Raman beams, but uses a magnetic field and the dipole trap laser itself to provide the Raman transitions. It has been applied for ground state cooling in optical lattices [81, 82, 83]. A different cooling method, which uses a pair of blue-detuned Raman beams, works by electromagnetically induced transparency [84]. It has been demonstrated to cool ions to the vibrational ground state of a Paul trap [85].

Polarization gradient cooling in near-resonant optical molasses reaches substantial sub-Doppler temperatures down to 1 µK [86, 87], but the state-dependent light shifts in our dipole trap could lead to greatly reduced cooling efficiencies [66]. A difference between the light shifts of the hyperfine ground states could be used to obtain cooling by a Sisyphus-like cycle using microwave transitions [88]. This differential light shift is very small in our linearly-polarized dipole trap, but it is much larger in a circularly polarized trap.

Finally there are proposals to use the coupling to a high-finesse cavity to cool atoms below the Doppler limit [89, 90]. A first experimental demonstration used single Rubidium atoms in a strongly coupled optical high-finesse cavity [91].

4.2 Quantum register

The observation of chains of optically resolved atoms in the dipole trap [40] suggests that they could be used as a quantum register for the implementation of quantum logic gates. Elementary quantum gates have been demonstrated with strings of ions in Paul traps [2, 3].

4.2.1 Atoms as qubits

The hyperfine ground states of a cesium atom can be used to store one bit of quantum information. A logic zero, $|\,0\,\rangle$, could for example be coded as $F = 4$ and a logic one, $|\,1\,\rangle$, as $F = 3$. Arbitrary superposition states $\alpha|\,0\,\rangle + \beta|\,1\,\rangle$ are then conveniently produced by microwave pulses acting on the 9.2 GHz hyperfine transition, as was demonstrated in our experiment [7]. Coherence times in the order of 10 ms were observed, limited by the temperature of the atoms in the dipole trap via the differential light shift. Using spin echo techniques to cancel this inhomogeneous dephasing effect, coherence times of up to 300 ms have been obtained.

4.2.2 Addressing individual atoms

Individual atoms which are trapped in potential wells a few micrometer apart can be addressed with microwave pulses by applying a magnetic field gradient along the dipole trap axis. Using a hyperfine transition which is Zeeman-shifted by the magnetic field, each atom has a different resonance frequency and can be selected in frequency space. In the near future we will explore the possibility of preparing arbitrary register states of the form

$$(\alpha_1|\,0\,\rangle_1 + \beta_1|\,1\,\rangle_1)(\alpha_2|\,0\,\rangle_2 + \beta_2|\,1\,\rangle_2)\ldots, \tag{4.1}$$

i. e. states that can be prepared without interaction between the atoms.

The register can be read out by projection onto the basis states $\{|\,0\,\rangle, |\,1\,\rangle\}$ and detecting the state of each atom. For this purpose, a strong push-out laser resonant with the $F = 4 \rightarrow F' = 5$ -transition removes all atoms in $F = 4$ (state $|\,0\,\rangle$) from the trap [7]. The remaining atoms are then observed with the CCD camera and indicate the digits in state $|\,1\,\rangle$.

4.2.3 Rearranging atoms with a second conveyor belt

As soon as more than two or three atoms are used, their random placement into the dipole trap should be rearranged into a regularly spaced chain to avoid unduely small or large separations. One idea is to “pick up” one atom, to move the remaining atoms along the trap axis using the transportation capability of our dipole trap, and to put back the separate atom at a suitable position. The microscopic tweezers could be realized by an auxiliary standing wave dipole trap intersecting the main trap at a right angle and transporting atoms in the vertical direction. At the crossing region, the strong axial dipole force of one trap overcomes the radial force of the other. In this way, one atom could be displaced vertically, while other atoms are moved horizontally through the crossing region.

Technically, the laser beam for the auxiliary trap could be shined in at a small angle to the vertical MOT beam. Below the vacuum cell, it could be simply retroreflected to obtain the standing wave structure, which could be turned into an conveyor belt by translating the retroreflecting mirror. As a laser source, the newly bought Yb:YAG laser could be used advantageously, since its output at 1030 nm will produce interference fringes with the Nd:YAG beam at 1064 nm only at a frequency of about 10^{13} Hz which won’t disturb trapped atoms.

4.2.4 Quantum shift register

Recently, we have transported single atoms in coherent superposition states in our optical conveyor belt over millimeter distances while preserving most of the coherence [7]. The decoherence mechanisms are well described by analytical models and are mostly of technical origin such as trap fluctuations. For a true “quantum shift register”, which transports *arbitrary* quantum states, the transportation of entangled states remains to be demonstrated.

4.3 High-finesse cavity

To generate entangled quantum register states or to perform quantum logic operations, a controlled coherent interaction is required. Our goal is to use an optical high finesse cavity as a means for coupling two atoms via the cavity mode. For this purpose, two neighboring atoms of a previously prepared quantum register state are transported into the cavity mode. After one or several quantum operations the register is transported back to be read out by the CCD-camera.

Once a cavity with improved finesse has been inserted into our apparatus, the first task is to detect atoms inside the cavity. A single atom trapped within the mode volume can drastically change the transmission of a probe laser through the cavity [92]. The transport of atoms with the dipole trap into the mode volume can thus be observed [93].

Since the radial motion of the atom in the dipole trap covers several nodes and anti-nodes of the cavity field, the coupling of the atom to the cavity field fluctuates between its maximum value and zero. For advanced experiments, a constant, high coupling has to be ensured. One possible solution would be a reduction of the radial temperature to improve the radial localization to below $\lambda/2$. At the same time, drifts of the relative position of cavity and dipole trap would have to be kept below $\lambda/4$. A more realistic suggestion uses the dipole force exerted by the cavity lock laser to confine the atoms to the anti-nodes of the 852 nm cavity field. This mechanism works at the center between the cavity mirrors if the lock laser is blue-detuned by an odd multiple of the free spectral range, or red-detuned by an even multiple.

Two suitably prepared atoms can be entangled by a simultaneous coupling to the cavity mode [8], or even by transporting them through the cavity [94]. As soon as the entanglement can be detected, the demonstration of a simple two-qubit quantum gate should be possible.

Appendix A

Cesium data

Important physical data of the cesium atom are presented in table A.1, and a level scheme of the first excited states including the hyperfine splitting is shown in fig. A.1.

Mass	m	$2.21 \cdot 10^{-25}$ kg
Vapor pressure (20°C)		10^{-6} mbar (10^{-4} Pa)
Natural lifetime $6\mathrm{P}_{3/2}$ (D2-transition)	τ_{D2}	30.5 ns
Decay rate (D2-transition)	Γ_{D2}	$2\pi \cdot 5.22$ MHz
Natural lifetime $6\mathrm{P}_{1/2}$ (D1-transition)	τ_{D1}	34.9 ns
Decay rate (D1-transition)	Γ_{D1}	$2\pi \cdot 4.56$ MHz
Saturation intensity (D2-transition) $\mid F=4, m_F=4\,\rangle \rightarrow \mid F'=5, m_{F'}=5\,\rangle$	I_0	11 W/m^2
Doppler temperature (D2-transition)	T_{D}	125 µK
Recoil energy (D2-transition)	$E_{\mathrm{r}}/k_{\mathrm{B}}$	99 nK

Table A.1: Some physical properties of the ^{133}Cs atom, from [27].

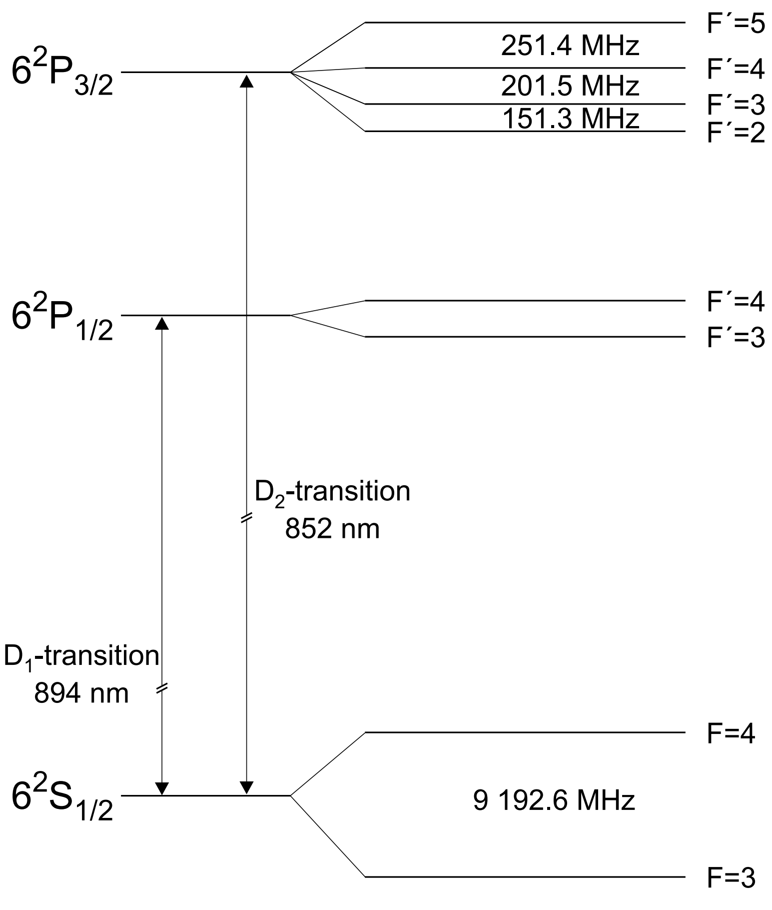

Figure A.1: Level scheme of ^{133}Cs.

Appendix B

Imaging system

During my thesis I developed a new imaging system, which allowed us to observe single atoms in the MOT as well as in the dipole trap with good signal to noise ratio. Its main part is a diffraction limited, long working distance lens system for the efficient collection of fluorescence [36]. The fluorescence count rate was improved by a factor of five, compared to the previously used optical system [95] which was limited by aberrations. The diffraction limited performance of the present system permits efficient discrimination of straylight without loss of fluorescence, as well as high resolution imaging.

B.1 Design

Our basic experimental requirement is the efficient collection of fluorescence light from single atoms in the MOT. The experimental geometry is shown in fig. B.1. The objective lens must reside outside the vacuum, because a lens inside the vacuum would be difficult to mount and align, and it would

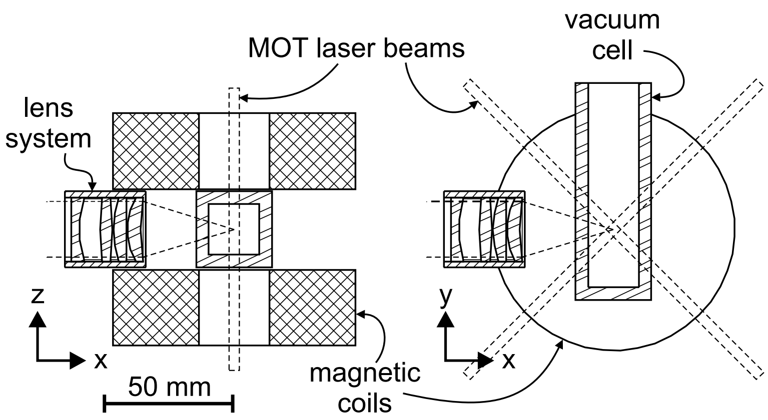

Figure B.1: Experimental Geometry: The lens system is placed close to the glass cell between the magnetic coils of the MOT.

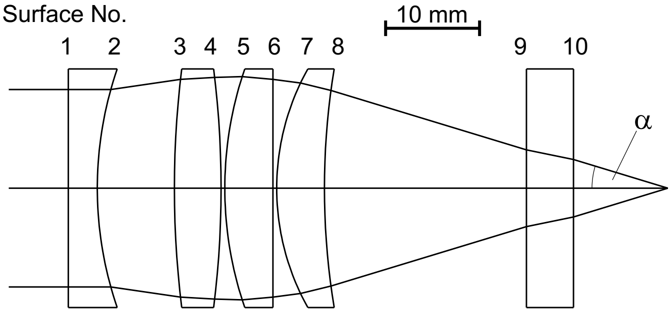

Figure B.2: Layout of the lens system. Surfaces 1 to 8 represent the objective itself, surfaces 9 and 10 belong to the silica wall of the glass cell.

interfere with the planned high finesse cavity setup inside the glass cell. The movable detection axis (sec. 1.3.3) would not have been possible neither.

B.1.1 Requirements

An important parameter of imaging systems is the numerical aperture (NA), which is defined as the sine of the calf cone angle α in fig. B.2. The summarized requirements for our objective lens are:

1. Collimation of the radiation of a point source at a wavelength of 852 nm with a large numerical aperture (NA). Once the light is collimated it can easily be imaged with low NA optics.

2. A minimum working distance of 36 mm. This is determined by our laser setup, because laser beams reflected off the glass cell must not enter the objective.

3. Near diffraction limited spot size, to enable high resolution imaging and spatial filtering of the fluorescence light. Retaining diffraction limited performance gets exceedingly difficult with increasing NA, because the n-th order aberrations ($n \geq 3$) grow like $(\mathrm{NA})^n$.

4. A field of view covering the MOT position uncertainty of about 1 mm.

5. Imaging through a plane silica window of 5 mm thickness, which introduces spherical aberrations for a NA>0.2.

6. Limitation of the outer diameter of the assembled lens system to 30 mm by the magnetic coils of the MOT, see fig. B.1.

Commercially available solutions for this application are either long working distance microscope objectives, which are relatively expensive, molded aspheric lenses, which usually have a short working distance, or achromats, which have larger spot sizes. None of these is meant to image through a thick window.

B.1.2 Design procedure

Single spherical lenses exhibit a reduction of their resolution above NA ≈ 0.1 due to their predominant spherical aberration. The main idea of a multi-lens system is therefore to compensate the aberrations of one surface with the aberrations of other ones. In our case, positive spherical aberration from convex surfaces is the primary fault to eliminate. It needs to be balanced by negative spherical aberrations of concave surfaces. To keep the design reasonably simple and cheap, we restricted ourselves to spherical surfaces and BK7 glass only.

I designed the objective using the program Oslo LT (Sinclair Optics, Oslo LT Version 5 Rev. 5.40, free download from http://www.sinopt.com/). It evaluates a lens system by tracing a bundle of rays through the lenses, calculating the refraction at each surface. For reasons of numerical stability, the simulated rays propagate backwards through the objective towards the MOT. There, the program computes the aberrations and the wavefront error, which is a measure for the deviation of the actual wavefront from the ideal sphere around the focal point. An automatic optimization routine, which varies the radii of curvature of the lens surfaces and the the distances between the lenses, can be used to minimize the aberrations until a local optimum is reached. The NA is kept constant during the optimization by fixing the entrance beam diameter and the effective focal length, which itself can be fixed by setting the radius of curvature of one surface to such a value that the prescribed focal length is attained.

Different starting configurations were used in search for a global optimum. The program was set up to minimize the squared sum of the spherical aberrations up to 7th order and third order coma and astigmatism. Acceptable performance could not be achieved with three lenses, with four lenses, however, good designs were possible. The radii of curvature of the lens surfaces were subsequently fixed to catalog values of our vendor (Lens-Optics GmbH), each time re-optimizing the remaining variables. In this way, most of the error introduced by the discretization is compensated. The resulting design is shown in Table B.1 and fig. B.2. It consists of three standard catalog lenses and one (non-standard) meniscus lens, but with catalog radii of curvature. It has got an effective focal length of 36 mm, a working distance of 36.5 mm, and a NA of 0.29. Moreover, it exactly compensates the aberrations introduced by the 5 mm silica window.

B.1.3 Theoretical performance

The fraction of fluorescence that can be collected is given by the ratio of the solid angle Ω covered by the objective (as viewed from the point source) to

Table B.1: Specifications of the lens system.

Surface No.	Radius of curvature [mm]	Distance to next surface [mm]	Material
1	∞	3.08	BK7
2	39.08	8.20	air
3	103.29	4.97	BK7
4	-103.29	0.40	air
5	39.08	5.12	BK7
6	∞	0.40	air
7	26.00	5.07	BK7
8	78.16	21.55	air
9	∞	5.00	silica
10	∞	10.00	vacuum

the total solid angle of 4π,

$$\frac{\Omega}{4\pi} = \frac{1}{2}\left(1 - \sqrt{1 - (\mathrm{NA})^2}\right), \tag{B.1}$$

which amounts to 2.1% in our case.

The design has a calculated wavefront aberration of $\lambda/1000$ rms on axis, resulting in a diffraction limited spot size of 1.8 µm (airy disc radius). Provided that the curvature of the image surface is taken into account, the wavefront error at a distance of 0.5 mm off axis is $\lambda/13$ rms. 1 mm off axis the spot size radius increases to 3 µm rms. The depth of focus can be estimated approximating the cone of light entering the lens system by a Gaussian beam with a divergence $\theta = w_0/z_0$ equal to the NA and calculating the confocal parameter $2z_0$:

$$\begin{aligned} 2z_0 &= \frac{2\lambda}{\pi\theta^2} && \text{(B.2)} \\ &= 6.4\ \mu\text{m}. && \text{(B.3)} \end{aligned}$$

The performance of the objective is not limited to the exact situation of our experimental setup. Changing the distance between surfaces 2 and 3 in fig. B.2 from 8.2 mm to 6.6 mm (and refocusing) allows the system to work even without the 5 mm silica window, with negligible performance degradation. Adaption to any window thickness up to 10 mm is possible. Although the design is optimized for 852 nm, it retains its diffraction limited performance from 1064 nm to 400 nm if the chromatic focus shift is taken into account.

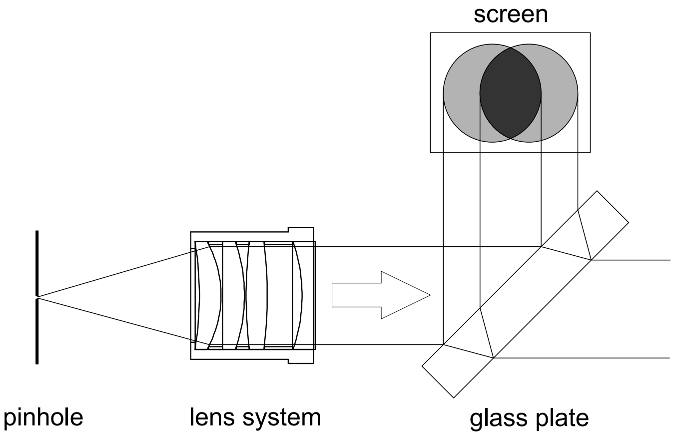

Figure B.3: Measuring wavefront deformations with a shear plate interferometer. A pinhole of 1 µm diameter acts as a point source. Its transmission is collimated by the lens system under test. A part of the beam is split off and is brought to interference with a displaced copy of itself on a screen.

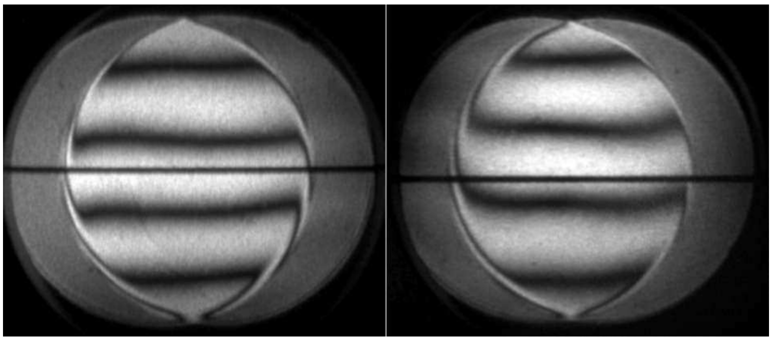

Figure B.4: Shear plate interferograms of the collimated beam beam produced by the objective lens. The shear is applied in two orthogonal directions, straight equidistant interference fringes correspond to a plane wavefront.

B.2 Assembly and experimental tests

All lenses have a diameter of 1", a surface quality (over 90 % of the clear aperture) of $\lambda/4$, a scratch-dig characteristic of 20-10, a centration to better than 5 minutes of arc and an anti-reflection coating for 650-1000 nm. They are stacked into an aluminum tube of 1" inner and 30 mm outer diameter and held in place by a threaded retainer ring. The distances between the lenses are determined by thin aluminum spacer rings. The mechanical parts have been manufactured to a tolerance of 0.1 mm. All aluminum surfaces are painted black to suppress straylight. The total cost of the objective including lenses and mechanical parts is about € 500 only.

An experimental test of the wave front aberration was performed by

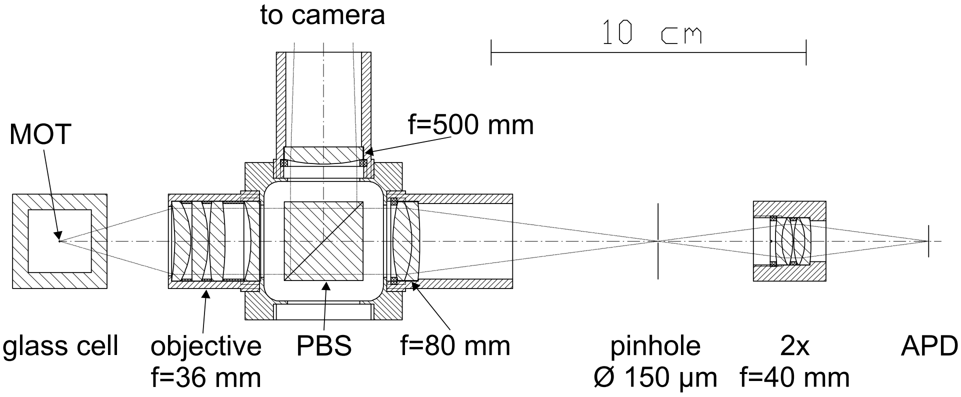

Figure B.5: Layout of the optical elements for APD and camera detection.

focusing an 852 nm laser beam onto a 1 µm diameter pinhole (Coherent, model 43-5172) serving as a high NA point source. The transmitted light was collimated by the objective under test and analyzed by means of a shear plate interferometer (Melles Griot, Model 09 SPM 001). It contains a thick glass plate with with two plane ($\lambda/10$) surfaces at 45° in the optical path, see fig. B.3. The reflections off the the front and the back surface interfere on a screen. They only partially overlap because of the relative shift ("shear") due to the thickness of the glass plate. The plate is also slightly wedged, such that a plane wavefront produces regular interference fringes. Any curvature of the incident wavefront results in a relative tilt of the overlapping wavefronts on the screen, which causes tilted or bent interference fringes. From the bending of the resulting interference fringes (fig. B.4) we estimate a peak-valley wavefront distortion of less than $\lambda/4$ over 90% of the clear aperture.

In our MOT setup the optical axis of the objective was carefully aligned onto the trap center using a Helium-Neon laser beam. The collimated fluorescence light from the MOT is focused by an $f = 80$ mm doublet lens (Melles Griot, 06LAI009, wavefront distortion specified $< \lambda/5$) onto a pinhole of 150 μm diameter for spatial filtering, see fig. B.5. Since the optical magnification from the MOT to the pinhole equals 2.2, an area of 67 µm diameter is thus selected at the MOT position. Using two more lenses (Melles Griot, 06LAI005, $f = 40$ mm), the pinhole is imaged 1:1 onto the APD.

For imaging onto the ICCD-camera, a higher magnification of about 14 is realized by focusing the collimated beam with a $f = 500$ mm plano-convex lens onto the image intensifier. At this focal length, a singlet lens suffices to reach diffraction-limited performance.

Appendix C

Electronics

C.1 Magnetic coil control

For our experiments, the magnetic quadrupole field must be switched between “high field” (normal MOT operation), “low field” (MOT loading) and “off”, see sec. 1.3.1. The switching time should be no more than a few milliseconds.

Although our power supply (F. u. G. GmbH, NTN 2800–65, 0–65 V, 0–40 A) permits the control of the output voltage by an analog programming input, it is not well suited for fast switching. First, it contains a thyristor preregulation stage, therefore it takes several hundred milliseconds to charge internal capacitors before the output voltage can rise. Second, when the current is set to zero by the external programming voltage, there is still a 50 Hz AC current leaking out of the supply, which produces magnetic fields in the order of 1 µT in the coils.

I have therefore designed the external control circuit shown in fig. C.1, which is placed between the power supply and the MOT coils. Two power MOSFETs (Q1, Q2), in series with the coils (L1, L2), are used as switches. When Q1 is switched on, the coil current is equal to the current limit setting of the power supply (typically 15.4 A), which then operates in constant current mode. When only Q2 is switched on, the coil current is equal to the voltage limit setting of the power supply, divided by R9, to typically 1.4 A. With both Q1 and Q2 switched off, the power supply voltage stays maximal, keeping all internal capacitors charged. The residual current through the coils in this state is negligible, since Q1 and Q2 have got leakage currents in the order of 10 nA. When the high coil current is switched off, the energy stored in the coils (about 2 Joules) is transferred to C14 within 4 ms and then safely dissipated in R11.

The MOSFETs Q1 and Q2 are controlled by a computer via TTL signals. The TTL inputs are fully isolated by optocouplers to protect the computer as well as the circuit. Additionally, keeping the power supply floating tolerates

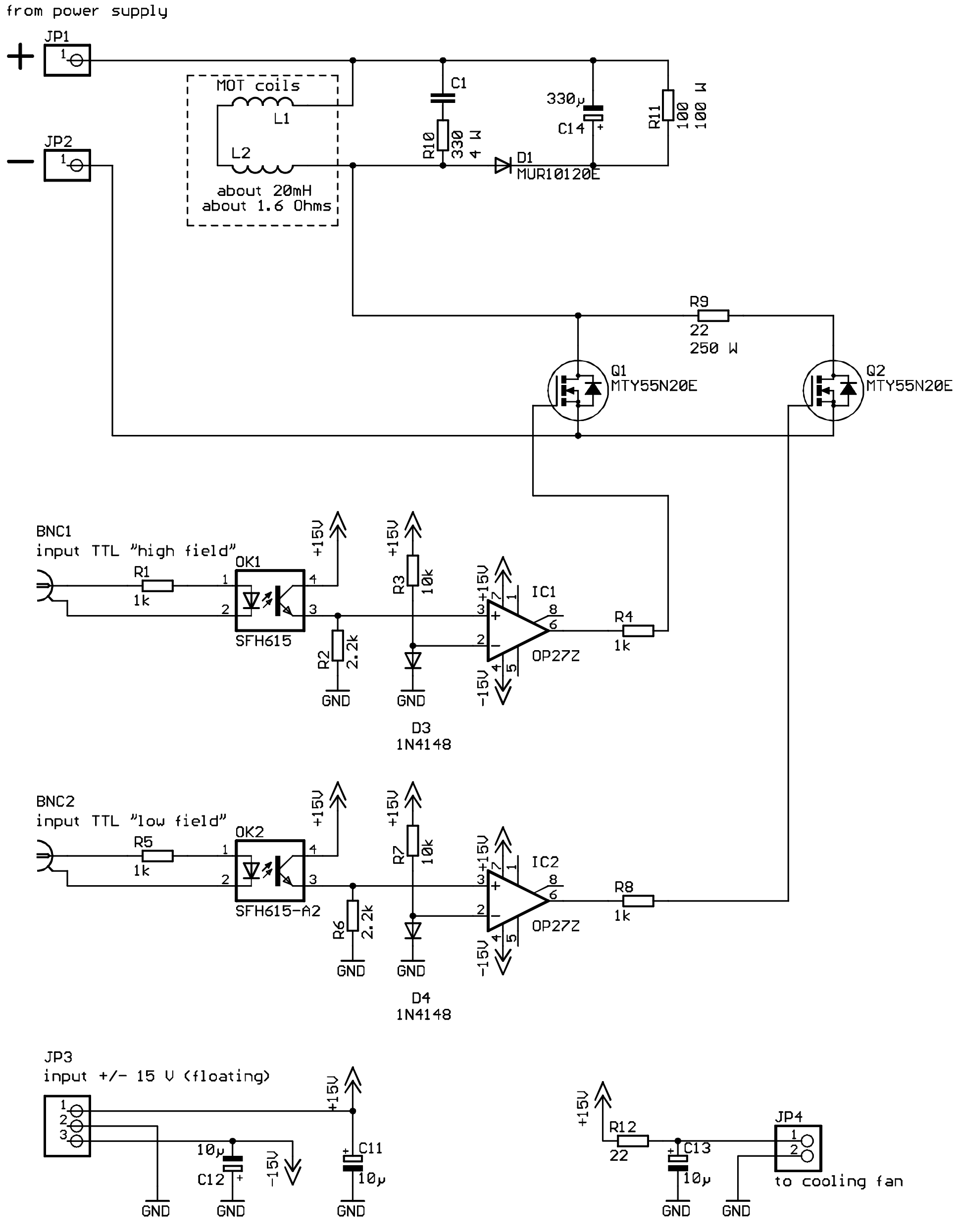

Figure C.1: Schematic of the magnetic coil control circuit.

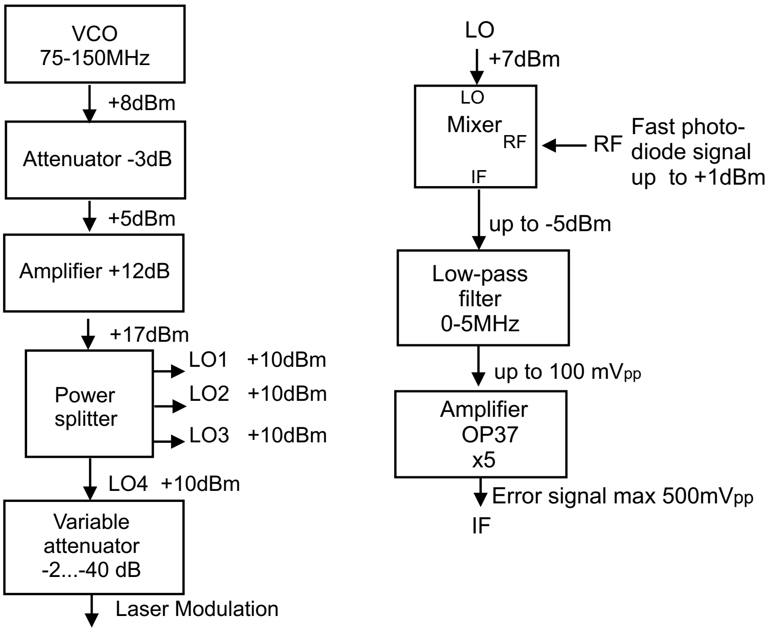

Figure C.2: Block diagrams of the VCO and mixer circuits used in the Pound-Drever-Hall stabilization of the high-finesse cavity.

one short circuit to ground anywhere within the water-cooled coils. A fan cools the MOSFETs and in particular R9, which dissipates 50 W during the low current state.

C.2 Components for cavity stabilization

The transfer cavity, the lock laser and the high-finesse cavity are frequency stabilized by the Pound-Drever-Hall method as described in section3.2. Therefore I designed two small, cheap circuits: The VCO box produces the modulation and local oscillator (LO) signals at the required power levels, and the mixer circuit includes a filter and an amplifier, see fig. C.2.

C.2.1 VCO and laser modulation

The VCO circuit of fig. C.3 contains a commercial VCO (Voltage-Controlled Oscillator, Mini-Circuits, model POS-150). A combination of a 3 dB attenuator and an RF amplifier (Mini-Circuits, model MAV-11) provides sufficient reverse isolation to prevent frequency pulling by reflected RF power. The amplified signal of +17 dBm is split by a 4-fold power splitter (Mini-Circuits, model PSC-4-1) to generate three fixed-level LO outputs (+10 dBm) for driving mixers. The fourth signal passes a voltage-controlled attenuator (Mini-Circuits, model TFAS-1) and is used for phase-modulation of the lock laser.

The modulation frequency is chosen to avoid radio-frequency interference and to optimize the Pound-Drever-Hall signal. The amplitude of the phase-modulation sidebands on the laser beam is set via the amplitude adjust of the modulation output.

C.2.2 Mixer

In the mixer circuit (fig. C.4), the LO and the photodiode (RF) signal are combined in a double-balanced mixer (Mini-Circuits, model SRA-1). The 3 dB attenuator brings the output of the VCO circuit down to the specified +7 dBm of the mixer and damps reflected and spurious signals. It can be omitted if an equivalent cable loss is present. The IF output of the mixer is followed by a diplexer-type low-pass filter [96], which presents an impedance of 50 Ω to the mixer for all frequencies. Signals below the cut-off frequency of 5 MHz (for the high-finesse cavity: 100 kHz) are pre-amplified by an operational amplifier (e. g. OP37). The amplification of the error signal within the mixer circuit reduces the relative influence of electromagnetic hum and noise which usually adds to the signal on its way to the proportional-integral servo amplifier.

C.2.3 Resonant avalanche photodiode detector

The resonant avalanche photodiode (APD) circuit of fig. C.5 is designed for low-noise detection of a high-frequency intensity modulation on a weak laser beam. The APD (PerkinElmer Optoelectronics, model C30902E) converts the light into a photocurrent while providing an internal avalanche gain of typically 10–100. The negative bias voltage of the APD of up to −250 V is controlled by a protection circuit (T2, T3) which limits the photocurrent to about 70 µA. Hence the APD will survive optical powers up to the mW range even at high gain.

The photocurrent feeds a parallel resonance circuit consisting of L1 and the capacity of the APD, T1 and stray capacitance. The resonance is tuned to the modulation frequency of our Pound-Drever-Hall stabilization of 86 MHz. The resonance circuit can be thought of as an impedance match of the purely capacitive APD to the capacitive input of T1, where L1 cancels the total capacity at the resonance frequency. The dual-gate MOSFET T1 (Infineon, BF998) has been chosen for the first amplification stage due to its low noise figure of 0.6 dB (at 200 MHz) and its high gain (> 20 dB). At its drain, the output impedance is approximately matched to 50 Ω by L2, which works as a resonance transformer together with C2. It was found, however, that the two resonance circuits around T1 easily self-oscillate by coupling back from L2 to L1. Therefore, we plan to replace L2 will by a small, broadband, ferrite-core transformer. The signal is further amplified

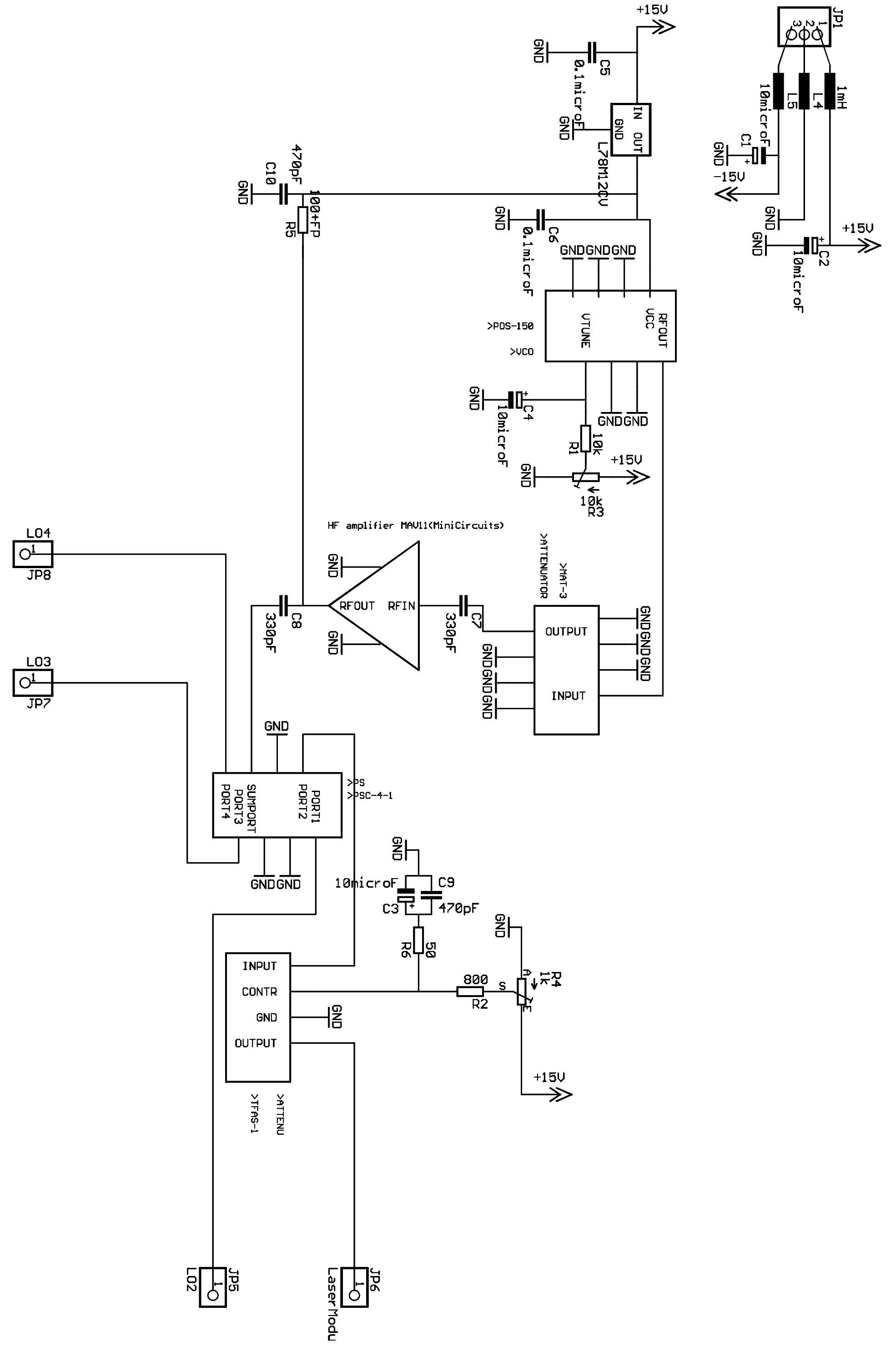

Figure C.3: Schematic of the VCO circuit.

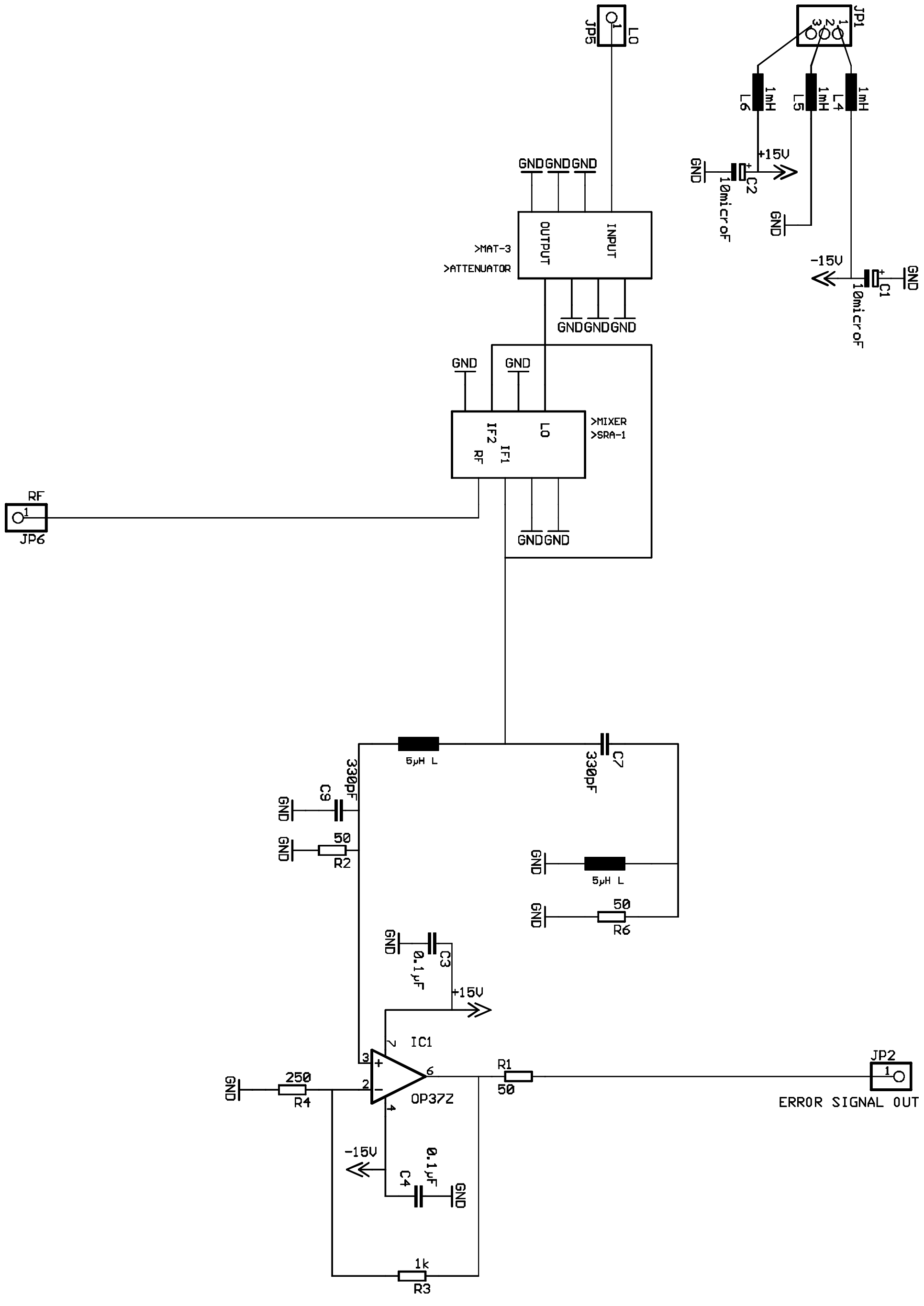

Figure C.4: Schematic of the mixer circuit.

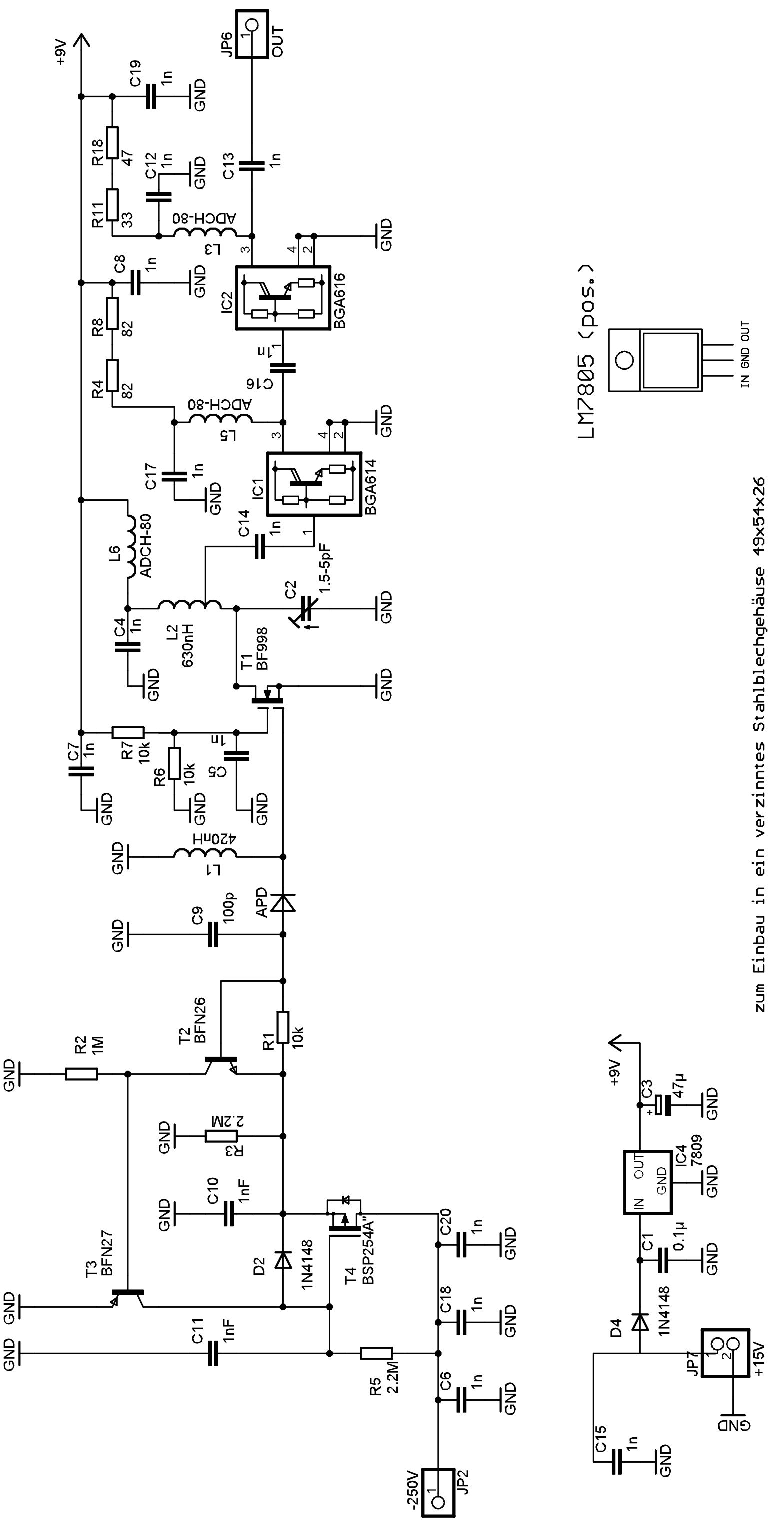

Figure C.5: Schematic of the resonant avalanche photodiode detector.

by two low-noise, 50 Ω, 20 dB MMIC gain blocks (IC1 and IC2). A similar circuit is described by H. Baldauf [97] and used for heterodyne detection of resonance fluorescence [98].

The high total gain was selected to make the output noise of the APD circuit visible at the output of the mixer circuit. Thus the overall noise of the mixer and the APD is dominated by the first amplification stage ensuring a maximum total signal-to-noise ratio.

Bibliography

[1] P. Shor, *Algorithms for Quantum Computation*, Proceedings of the 35th Annual Symposium on Foundations of Computer Science, 124 (1994)

[2] F. Schmidt-Kaler, H. Häffner, M. Riebe, S. Gulde, G. P. T. Lancaster, T. Deuschle, C. Becher, C. F. Roos, J. Eschner, and R. Blatt, *Realization of the Cirac-Zoller controlled-NOT quantum gate*, Nature **422**, 408 (2003)

[3] D. Leibfried, B. DeMarco, V. Meyer, D. Lucas, M. Barrett, J. Britton, W. M. Itano, B. Jelenković, C. Langer, T. Rosenband, and D. J. Wineland, *Experimental demonstration of a robust, high-fidelity geometric two ion-qubit phase gate*, Nature **422**, 412 (2003)

[4] D. Haubrich, H. Schadwinkel, F. Strauch, B. Ueberholz, R. Wynands, and D. Meschede, *Observation of individual neutral atoms in magnetic and magnetooptical traps*, Europhys. Lett. **34**, 663 (1996)

[5] S. Kuhr, *A controlled quantum system of individual neutral atoms*, Ph.D. thesis, Universität Bonn (2003)

[6] S. Kuhr, W. Alt, D. Schrader, M. Müller, V. Gomer, and D. Meschede, *Deterministic delivery of a single atom*, Science **293**, 278 (2001), [published online June 14, 2001; 10.1126/science.1062725]

[7] S. Kuhr, W. Alt, D. Schrader, I. Dotsenko, Y. Miroshnychenko, W. Rosenfeld, M. Khudaverdyan, V. Gomer, A. Rauschenbeutel, and D. Meschede, *Coherence Properties and Quantum State Transportation in an Optical Conveyor Belt*, Phys. Rev. Lett. **91**, 213002 (2003)

[8] L. You, X. X. Yi, and X. H. Su, *Quantum logic between atoms inside a high-Q optical cavity*, Phys. Rev. A **67**, 032308 (2003)

[9] T. Pellizzari, S. A. Gardiner, J. I. Cirac, and P. Zoller, *Decoherence, Continous Observation and Quantum Computing: A Cavity QED Model*, Phys. Rev. Lett. **75**, 3788 (1995)

[10] A. Rauschenbeutel, G. Nogues, S. Osnaghi, P. Bertet, M. Brune, J. M. Raimond, and S. Haroche, *Coherent Operation of a Tunable Quantum Phase Gate in Cavity QED*, Phys. Rev. Lett. **83**, 5166 (1999)

[11] M. Weidinger, B. T. H. Varcoe, R. Heerlein, and H. Walther, *Trapping States in the Micromaser*, Phys. Rev. Lett. **82**, 3795 (1999)

[12] C. J. Hood, T. W. Lynn, A. C. Doherty, A. S. Parkins, and H. J. Kimble, *The Atom-Cavity Microscope: Single Atoms Bound in Orbit by Single Photons*, Science **287**, 1447 (2000)

[13] P. W. H. Pinkse, T. Fischer, P. Maunz, and G. Rempe, *Trapping an atom with single photons*, Nature **404**, 365 (2000)

[14] W. Rosenfeld, *A high finesse optical resonator for cavity QED experiments*, Diplomarbeit, Universität Bonn (2003)

[15] T. W. Hänsch and A. L. Schawlow, *Cooling of gases by laser radiation*, Opt. Commun. **13**, 68 (1975)

[16] S. Chu, L. Hollberg, J. E. Bjorkholm, A. Cable, and A. Ashkin, *Three-dimensional Viscous Confinement and Cooling of Atoms by Resonance Radiation Pressure*, Phys. Rev. Lett. **55**, 48 (1985)

[17] E. L. Raab, M. Prentiss, A. Cable, S. Chu, and D. E. Pritchard, *Trapping of Neutral Sodium Atoms with Radiation Pressure*, Phys. Rev. Lett. **59**, 2631 (1987)

[18] D. J. Wineland and W. M. Itano, *Laser cooling of atoms*, Phys. Rev. A **20**, 1521 (1979)

[19] R. J. Cook, *Quantum-Mechanical Fluctuations of the Resonance-Radiation Force*, Phys. Rev. Lett. **44**, 976 (1980)

[20] J. Dalibard and C. Cohen-Tannoudji, *Laser cooling below the Doppler limit by polarization gradients: simple theoretical models*, J. Opt. Soc. Am. B **6**, 2023 (1989)

[21] S. D. Gensemer, V. Sanchez-Villicana, K. Y. N. Tan, T. T. Grove, and P. L. Gould, *Trap-Loss collisions of* ^{85}*Rb and* ^{87}*Rb: Dependence on trap parameters*, Phys. Rev. A **56**, 4055 (1997)

[22] B. Ueberholz, S. Kuhr, D. Frese, V. Gomer, and D. Meschede, *Cold collisions in a high-gradient magneto-optical trap*, J. Phys. B: At. Mol. Opt. Phys. **35**, 4899 (2002)

[23] D. Haubrich, A. Höpe, and D. Meschede, *A simple model for optical capture of atoms in strong magnetic quadrupole fields*, Opt. Commun. **102**, 225 (1993)

[24] J. Weiner, V. S. Bagnato, S. Zilio, and P. S. Julienne, *Experiments and theory in cold and ultracold collisions*, Rev. Mod. Phys. **71**, 1 (1999)

[25] B. Ueberholz, S. Kuhr, D. Frese, V. Gomer, and D. Meschede, *Counting cold collisions*, J. Phys. B: At. Mol. Opt. Phys. **33**, L135 (2000)

[26] D. Frese, B. Ueberholz, S. Kuhr, W. Alt, D. Schrader, V. Gomer, and D. Meschede, *Single Atoms in an Optical Dipole Trap: Towards a Deterministic Source of Cold Atoms*, Phys. Rev. Lett. **85**, 3777 (2000)

[27] D. A. Steck, *Cesium D Line Data* (23 January 1998, Revision 1.5, 21 November 2002), `http://steck.us/alkalidata/`

[28] C. E. Wieman and L. Hollberg, *Using diode lasers for atomic physics*, Rev. Sci. Instr. **62**, 1 (1991)

[29] L. Ricci, M. Weidemüller, T. Esslinger, A. Hemmerich, C. Zimmermann, V. Vuletic, W. König, and T. W. Hänsch, *A compact grating-stabilized diode laser system for atomic physics*, Opt. Commun. **117**, 541 (1995)

[30] C. Wieman and T. W. Hänsch, *Doppler-Free Laser Polarization Spectroscopy*, Phys. Rev. Lett. **36**, 1170 (1976)

[31] C. P. Pearman, C. S. Adams, S. G. Cox, P. F. Griffin, D. A. Smith, and I. G. Hughes, *Polarization spectroscopy of a closed atomic transition: applications to laser frequency locking*, J. Phys. B **35**, 5141 (2002)

[32] T. W. Hänsch, M. D. Levenson, and A. L. Schawlow, *Complete Hyperfine Structure of a Molecular Iodine Line*, Phys. Rev. Lett. **26**, 946 (1971)

[33] B. Dahmani, L. Hollberg, and R. Drullinger, *Frequency stabilization of semiconductor lasers by resonant optical feedback*, Opt. Lett. **12**, 876 (1987)

[34] Z. Hu and H. J. Kimble, *Observation of a single atom in a magnetooptical trap*, Opt. Lett. **19**, 1888 (1994)

[35] F. Ruschewitz, D. Bettermann, J. L. Peng, and W. Ertmer, *Statistical investigations on single trapped neutral atoms*, Europhys. Lett. **34**, 651 (1996)

[36] W. Alt, *An objective lens for efficient fluorescence detection of single atoms*, Optik **113**, 142 (2002)

[37] V. Gomer, F. Strauch, B. Ueberholz, S. Knappe, and D. Meschede, *Single-atom dynamics revealed by photon correlations*, Phys. Rev. A **58**, 1657 (1998)

[38] S. A. Hopkins and A. V. Durrant, *Parameters for polarization gradients in three-dimensional electromagnetic standing waves*, Phys. Rev. A **56**, 4012 (1997)

[39] C. G. Townsend, N. H. Edwards, C. J. Cooper, K. P. Zetie, and C. J. Foot, *Phase-space density in the magneto-optical trap*, Phys. Rev. A **52**, 1423 (1995)

[40] Y. Miroshnychenko, D. Schrader, S. Kuhr, W. Alt, I. Dotsenko, M. Khudaverdyan, A. Rauschenbeutel, and D. Meschede, *Continued imaging of the transport of a single neutral atom*, Optics Express **11**, 3498 (2003)

[41] V. S. Letokhov, *Doppler line narrowing in a standing light wave*, Pis. Zh. Eksp. Teor. Fiz. **7**, 348 (1968), engl. translation JTEP Lett. **7**, 272 (1968)

[42] A. Ashkin, *Acceleration and Trapping of Particles by Radiation Pressure*, Phys. Rev. Lett. **24**, 156 (1970)

[43] A. Ashkin, *Laser in Life Sciences*, Berichte der Bunsen-Gesellschaft für Physikalische Chemie **93**, 255 (1988)

[44] S. Chu, J. E. Bjorkholm, A. Ashkin, and A. Cable, *Experimental Observation of Optically Trapped Atoms*, Phys. Rev. Lett. **57**, 314 (1986)

[45] R. Grimm, M. Weidemüller, and Y. B. Ovchinnikov, *Optical dipole traps for neutral atoms*, Adv. At. Mol. Opt. Phys. **42**, 95 (2000)

[46] J. D. Jackson, *Classical Electrodynamics*, Wiley, New York, 2nd edition (1962)

[47] M. Fabry and J. R. Cussenot, *Détermination théorique et expérimentale des forces d'oscillateur des transitions de l'atome de césium*, Can. J. Phys. **54**, 836 (1976)

[48] W. Alt, D. Schrader, S. Kuhr, M. Müller, V. Gomer, and D. Meschede, *Single atoms in a standing-wave dipole trap*, Phys. Rev. A **67**, 033403 (2003)

[49] J. Dalibard and C. Cohen-Tannoudji, *Dressed-atom approach to atomic motion in laser light: the dipole force revisited*, J. Opt. Soc. Am. B **2**, 1707 (1985)

[50] C. Cohen-Tannoudji, J. Dupont-Roc, and G. Grynberg, *Atom-Photon Interactions*, Wiley, New York (1992)

[51] D. Schrader, *AC Stark shift* (2001), unpublished

[52] D. Schrader, *Ein Förderband für einzelne Atome*, Diplomarbeit, Universität Bonn (2000)

[53] D. Schrader, S. Kuhr, W. Alt, M. Müller, V. Gomer, and D. Meschede, *An optical conveyor belt for single neutral atoms*, Appl. Phys. B **73**, 819 (2001)

[54] P. Kohns, P. Buch, W. Sübtitz, C. Csambal, and W. Ertmer, *On-Line Measurement of Sub-Doppler Temperatures in a Rb Magneto-optical Trap-by-Trap Centre Oscillations*, Europhys. Lett. **22**, 517 (1993)

[55] A. Höpe, D. Haubrich, G. Müller, W. G. Kaenders, and D. Meschede, *Neutral Cesium Atoms in Strong Magnetic-Quadrupole Fields at Sub-Doppler Temperatures*, Europhys. Lett. **22**, 669 (1993)

[56] M. Mudrich, S. Kraft, K. Singer, R. Grimm, A. Mosk, and M. Weidemüller, *Sympathetic Cooling with Two Atomic Species in an Optical Trap*, Phys. Rev. Lett. **88**, 253001 (2002)

[57] G. Reymond, N. Schlosser, and P. Grangier, *Single Atom Manipulation in a Microscopic Dipole Trap*, in H. R. Sadeghpour, E. J. Heller, and D. E. Pritchard, eds., *Proceedings of the XVIII International Conference on Atomic Physics*, World Scientific (2002)

[58] L. D. Landau and E. M. Lifschitz, *Mechanics*, Pergamon, New York (1976)

[59] W. H. Press, S. A. Teukolsky, W. T. Vetterling, and B. P. Flannery, *Numerical Recipes in C*, Cambridge University Press, New York, 2nd edition (1992)

[60] R. Barlow, *Statistics*, Wiley, New York (1989)

[61] V. Bagnato, D. E. Pritchard, and D. Kleppner, *Bose-Einstein condensation in an external potential*, Phys. Rev. A **35**, 4354 (1987)

[62] V. Gomer, personal communication

[63] T. A. Savard, K. M. O'Hara, and J. E. Thomas, *Laser-noise-induced heating in far-off resonance optical traps*, Phys. Rev. A **56**, R1095 (1997)

[64] M. E. Gehm, K. M. O'Hara, T. A. Savard, and J. E. Thomas, *Dynamics of noise-induced heating in atom traps*, Phys. Rev. A **58**, 3914 (1998)

[65] I. Dotsenko, W. Alt, S. Kuhr, D. Schrader, M. Müller, Y. Miroshnychenko, V. Gomer, A. Rauschenbeutel, and D. Meschede, *Application of electro-optically generated light fields for Raman spectroscopy of trapped cesium atoms*, Appl. Phys. B **78**, 711 (2004)

[66] Marc Cheneau, *Laser cooling of single atoms in a standing-wave dipole trap*, Internship report (2003)

[67] D. Meschede, *Optik, Licht und Laser*, Teubner, Stuttgart (1999)

[68] M. Khudaverdyan, *Addressing of individual atoms in an optical dipole trap*, Diplomarbeit, Universität Bonn (2003)

[69] G. Rempe, H. Walther, and N. Klein, *Observation of Quantum Collapse and Revival in a One-Atom Maser*, Phys. Rev. Lett. **58**, 353 (1987)

[70] M. Brune, F. Schmidt-Kaler, A. Maali, J. Dreyer, E. Hagley, J. M. Raimond, and S. Haroche, *Quantum Rabi Oscillation: A Direct Test of Field Quantization in a Cavity*, Phys. Rev. Lett. **76**, 1800 (1996)

[71] P. R. Berman, ed., *Cavity Quantum Electrodynamics*, Advances in atomic, molecular, and optical physics, Academic Press, San Diego (1994)

[72] Y. Miroshnychenko, *Design and test of a high finesse resonator for single atom experiments*, Diplomarbeit, Universität Bonn (2002)

[73] H. Mabuchi, J. Ye, and H. J. Kimble, *Full observation of single-atom dynamics in cavity QED*, Appl. Phys. B **68**, 1095 (1999)

[74] R. Drever and J. Hall, *Laser phase and frequency stabilization using an optical resonator*, Appl. Phys. B **31**, 97 (1983)

[75] D. Schrader, personal communication (2003)

[76] M. Müller, *Ramankühlung einzelner Atome*, Diplomarbeit, Universität Bonn (2000)

[77] I. Dotsenko, *Raman spectroscopy of single atoms*, Diplomarbeit, Universität Bonn (2002)

[78] H. J. Lee, C. S. Adams, M. Kasevich, and S. Chu, *Raman Cooling of Atoms in an Optical Dipole Trap*, Phys. Rev. Lett. **76**, 2658 (1996)

[79] H. Perrin, A. Kuhn, I. Bouchoule, and C. Salomon, *Sideband cooling of neutral atoms in a far-detuned optical lattice*, Europhys. Lett. **42**, 395 (1998)

[80] A. Kuhn, H. Perrin, W. Hänsel, and C. Salomon, *Three Dimensional Raman Cooling using Velocity Selective Rapid Adiabatic Passage*, in K. Burnett, ed., *OSA Tops on Ultracold Atoms and BEC*, volume 7, 58, European Conference on Lasers and Electro-Optics/European Quantum Electronics Conference CLEO/EUROPE-EQEC, Optical Society of America, Washington DC, Hamburg, Germany (1996)

[81] S. E. Hamann, D. L. Haycock, G. Klose, P. H. Pax, I. H. Deutsch, and P. S. Jessen, *Resolved-Sideband Raman Cooling to the Ground State of an Optical Lattice*, Phys. Rev. Lett. **80**, 4149 (1998)

[82] A. J. Kerman, V. Vuletić, C. Chin, and S. Chu, *Beyond Optical Molasses: 3D Raman Sideband Cooling of Atomic Cesium to High Phase-Space Density*, Phys. Rev. Lett. **84**, 439 (2000)

[83] A. J. Kerman, *Raman sideband cooling and cold atomic collisions in optical lattices*, Ph.D. thesis, Stanford University (2002)

[84] G. Morigi, J. Eschner, and C. H. Keitel, *Ground State Laser Cooling Using Electromagnetically Induced Transparency*, Phys. Rev. Lett. **85**, 4458 (2000)

[85] C. F. Roos, D. Leibfried, A. Mundt, F. Schmidt-Kaler, J. Eschner, , and R. Blatt, *Experimental Demonstration of Ground State Laser Cooling with Electromagnetically Induced Transparency*, Phys. Rev. Lett. **85**, 5547 (2000)

[86] A. Kastberg, W. D. Phillips, S. L. Rolston, R. J. C. Spreeuw, and P. S. Jessen, *Adiabatic Cooling of Cesium to 700 nK in an Optical Lattice*, Phys. Rev. Lett. **74**, 1542 (1995)

[87] D. Boiron, A. Michaud, P. Lemonde, Y. Castin, C. Salomon, S. Weyers, K. Szymaniec, L. Cognet, and A. Clairon, *Laser cooling of cesium atoms in gray optical molasses down to 1.1 μK*, Phys. Rev. A **53**, R3734 (1996)

[88] K. W. Miller, S. Dürr, and C. E. Wieman, *RF-induced Sisyphus cooling in an optical dipole trap*, Phys. Rev. A **66**, 023406 (2002)

[89] P. Horak, G. Hechenblaikner, K. M. Gheri, H. Stecher, and H. Ritsch, *Cavity-Induced Atom Cooling in the Strong Coupling Regime*, Phys. Rev. Lett. **79**, 4974 (1997)

[90] V. Vuletić and S. Chu, *Laser Cooling of Atoms, Ions, or Molecules by Coherent Scattering*, Phys. Rev. Lett. **84**, 3787 (2000)

[91] P. Maunz, T. Puppe, I. Schuster, N. Syassen, P. W. H. Pinkse, and G. Rempe, *Cavity cooling of a single atom*, Nature **428**, 50 (2004)

[92] J. McKeever, J. R. Buck, A. D. Boozer, A. Kuzmich, H.-C. Nägerl, D. M. Stamper-Kurn, and H. J. Kimble, *State-Insensitive Cooling and Trapping of Single Atoms in an Optical Cavity*, Phys. Rev. Lett. **90**, 133602 (2002)

[93] J. A. Sauer, K. M. Fortier, M. S. Chang, C. D. Hamley, and M. S. Chapman, *Cavity QED with optically transported atoms*, Phys. Rev. A **69**, 051804 (2004)

[94] C. Marr, A. Beige, and G. Rempe, *Entangled-state preparation via dissipation-assisted adiabatic passages*, Phys. Rev. A **68**, 033817 (2003)

[95] F. Strauch, *Positionsempfindliche Korrelationsmessungen an einzelnen Atomen*, Ph.D. thesis, Universität Bonn (1997)

[96] C. Hutchinson, ed., *The ARRL Handbook for Radio Amateurs 2001*, American Radio Relay League, 78. edition (2000)

[97] H. Baldauf, *Untersuchung der Resonanzfluoreszenz eines gespeicherten Ions*, Diplomarbeit, Max-Planck-Institut für Quantenoptik, Garching (1994)

[98] J. T. Höffges, H. W. Baldauf, T. Eichler, S. R. Helmfried, and H. Walther, *Heterodyne measurement of the fluorescent radiation of a single trapped ion*, Opt. Commun. **133**, 170 (1997)

Danksagung

Mein erster Dank gilt Professor Meschede, der es mir ermöglicht hat an einem sehr interessanten Experiment zu arbeiten. Den Hunger des stetig wachsenden Experimentes nach Sachmitteln und Personal hat er in bemerkenswerter Weise aus ständig neuen Geldquellen gestillt. Professor Eberhard Klempt danke ich für die Überhahme des Zweitgutachtens.

Den größten Anteil am Erfolg des Experimentes und damit am Gelingen meiner Doktorarbeit haben sicherlich Dr. Stefan Kuhr und Dominik Schrader, mit denen ich während meiner gesamten Zeit in Bonn zusammengearbeitet habe. Stefan danke ich dafür, daß er mit Ehrgeiz, Vorausplanung und Optimismus das Experiment unermüdlich vorangetrieben hat. Seiner Vorliebe für Bier habe ich zahlreiche gemeinsame Kneipenbesuche zu verdanken. Dominik hat schon als Diplomand jede noch so lange Meßnacht mit Begeisterung mitgemacht (im Gegensatz zu mir . . .). Mit seiner theoretischen Begabung hat er viel zum Verständnis und zur Planung unseres Experimentes beigetragen. Auch für seine Bevorzugung guter Restaurants gegenüber der Mensa bin ich dankbar.

Für ihre unersetzlichen Beiträge danke ich allen (weiteren) Diplomanden unseres Experimentes, Martin Müller, Yevhen Miroshnychenko, Igor Dotsenko, Wenjamin Rosenfeld, Mkrtych Khudaverdyan und Leonid Förster. Mit ihnen habe ich nicht nur gelernt, wie man Leute anlernt und anleitet, sondern auch erfahren, daß es Freude macht. Yevhen und Igor, die als Doktoranden an unserem Experiment weitermachen, waren in dieser Zeit an vielen Messungen beteiligt. Daniel Frese hat zu Beginn seiner Doktorarbeit noch einige Messungen an unserem Experiment durchgeführt, und Wade Smith hat ein halbes Jahr lang als Gastdoktorand seine technischen und persönlichen Erfahrungen von einer anderen Arbeitsgruppe eingebracht. Marc Cheneau hat als Ferienpraktikand bemerkenswerte theoretische Arbeit geleistet.

Unserem Postdoc Dr. Victor Gomer danke ich für seine engagierte Betreuung während der ersten Zeit meiner Arbeit. Er hatte immer Zeit für Fragen und Diskussionen. Dabei hat er mir sowohl mittels einfacher Abschätzungen tiefe Einblicke in die physikalische Theorie gegeben, als auch ganz praktische Erfahrungen in Vakuumtechnik vermittelt. Darüberhinaus hat er viele Verwaltungsaufgaben übernommen und uns Doktoranden dadurch den Rücken frei gehalten für die Arbeit im Labor.

Dr. Arno Rauschenbeutel hat dann dankenswerter Weise die Postdoc-Pflichten übernommen. In unzähligen Diskussionen habe ich viel von seinem immensen Wissen über Quantenoptik und Physik im Allgemeinen gelernt. Selbst über die Betriebsprobleme der Deutschen Bahn wußte er stets interessante Details zu berichten.

Die Mitarbeiter mehrerer feinmechanischen Werkstätten haben unsere

Groß-, Eil- und Massenaufträge stets in bester Qualität gefertigt und damit unseren experimentellen Aufbau erst ermöglicht. Die Mitarbeiter der Elektronikwerkstatt haben unzählige Geräte gebaut und repariert. Unser Hausmeister, Herr Ernst, hat uns bei vielfältigen technischen und anderen Problemen geholfen.

Den Mitarbeitern des Sekretariates und der Verwaltung, Dagmar Eichler-Becker, Annelise Miglo, Illona Jaschke, Dr. Robert Haberstroh, Dr. Dietmar Haubrich und Fien Latumahina danke ich für die Erledigung aller verwaltungstechnischer und organisatorischer Aufgaben in freundlicher Atmosphäre.

Viele wertvolle Freunde, Förderer und Diskussionspartner müssen aus Platzgründen ungenannt bleiben, auch bei ihnen bedanke ich mich.

Mein größter Dank gilt meinen Eltern, meiner Großmutter und meiner Schwester, die mich immer unterstützt und besonders in schlechten Zeiten wieder aufgerichtet haben.

Allen genannten und ungenannten Personen wünsche ich alles Gute.